BULGARIAN ACADEMY OF SCIENCES

INSTITUTE FOR NUCLEAR RESEARCH AND NUCLEAR ENERGY

TOMOGRAPHY OF THE ELECTRON BEAM TRANSVERSE PHASE SPACE AT PITZ

Galina Asova

Thesis submitted in conformity with the requirements for the degree
Doctor of Philosophy

Sofia, 2012

БЪЛГАРСКА АКАДЕМИЯ НА НАУКИТЕ

ИНСТИТУТ ЗА ЯДРЕНИ ИЗСЛЕДВАНИЯ И ЯДРЕНА ЕНЕРГЕТИКА

ГАЛИНА ЛАЗАРОВА АСОВА

ТОМОГРАФИЯ НА НАПРЕЧНОТО ФАЗОВО ПРОСТРАНСТВО НА ЕЛЕКТРОНЕН СНОП В PITZ

Научна специалност: 4.1 Физически науки
(Ускорители на електрони)

ДИСЕРТАЦИЯ
за присъждане на образователна и научна степен
"ДОКТОР"

София, 2012

TOMOGRAPHY OF THE ELECTRON BEAM TRANSVERSE PHASE SPACE AT PITZ

Galina Asova

За един истински мечтател, за Татко...

Abstract

The operation of a Free Elector Laser, FEL, requires high energy, high peak current electron beams with small transverse emittance. In the contemporary FELs, the electron beam is passed through a periodic magnetic structure - an undulator - which modifies the straight beam trajectory into a sinusoidal one, where FEL light is generated at each bend. According to the energy, the transverse emittance and the peak current of the beam and the parameters of the undulator, FEL radiation with wavelength in the range of nano- to micrometers can be generated.

Studies and development of FELs are done all over the world. The Free electron LASer in Hamburg, FLASH, and the international European X-ray FEL, XFEL [1], in Hamburg, Germany, are two leading projects of the Deutsches Elektronen SYnchrotron, DESY. Part of the research program on FELs in DESY is realized in Zeuthen within the project Photo-Injector Test Facility at DESY in Zeuthen, PITZ. PITZ is an international collaboration including Germany, Russia, Italy, France, Bulgaria, Thailand, United Kingdom. The Institute of Nuclear Research and Nuclear Energy, INRNE, at the Bulgarian Academy of Sciences participates from bulgarian side.

PITZ studies and optimizes the photo-injectors for FLASH and the XFEL. The research program emphasizes on detailed measurements of the transverse phase-space density distribution [2]. Until 2010 the single slit scan technique has been used to measure the beam transverse distributions. At the end of 2010 a module for tomographic diagnostics has been installed which extends the possibilities of PITZ to measure simultaneously the two transverse planes of a single micropulse with improved signal-to-noise ratio. The difficult conditions of low emittance for high bunch charge and low energy make the operation of the module challenging.

This thesis presents the design considerations for the tomography module, a number of reconstruction algorithms and their applicability to limited data sets, the influence of the above mentioned challenges and approaches to solve them. The first measurements obtained with the device are shown. Using numerical particle tracking it is shown that the tomographic reconstruction is consistent with the simulated data. Cross-check of some of the measured data with results obtained at different locations along the beamline, using single slit scans, prove that the measured phase-space distributions and the corresponding emittance values are consistent. Shot-to-shot fluctuations are revealed which would not be possible with the standard slit scans. Despite certain difficulties related to asymmetry of the electron beam transverse profiles and the strong influence of space-charge forces, it is shown the module fulfills its purpose and improves the resolution of the measurements of the transverse phase spaces.

Абстракт

Генериране на лъчение от Лазерите на Свободни Електрони (ЛСЕ, *Free Electron Laser*) изисква силнотокови и високоенергетични електронни снопове с малък напречен емитанс. В съвременните ЛСЕ електронният сноп от ускорителя, преминал през периодична магнитна структура - ондулатор - е с модулирана синусоидална траекторията, на чиито пикове се формира лазерното лъчение. В зависимост от енергията, напречния емитанс и пиковия ток на електронния сноп, както и от характеристиките на ондулатора, ЛСЕ генерират лъчение от нано- до микрометри спектрален диапазон.

През последните десетиления широкомащабни изследвания в тази област в Европа, САЩ, Япония и Русия доведоха до създаването на мощни ЛСЕ. В Европа изследванията са съсредоточени в Германия, Швейцария, Швеция, Италия и Русия. В създадения през 60-те години на миналия век немски изследователски център Deutsches Elektronen SYnchrotron (DESY) се реализира дългосрочна програма за разработка на ЛСЕ [1] - PETRA, Free electron LASer in Hamburg (FLASH) и международният European X-ray FEL (XFEL). Част от програмата се реализира и в Цойтен, Берлин, в бившия Институт по Физика на високи енергии на Академията на Науките на ГДР, сега вече DESY Zeuthen.

През 2002 год. там бе формирана колаборацията Photo-Injector Test Facility at DESY in Zeuthen (PITZ) включваща научни колективи от Германия, България, Франция, Русия, Англия, Италия и Тайланд. От България участва колектив от физици, математици и инженери от Института за Ядрени Изследвания и Ядрена Енергетика (ИЯИЯЕ) при Българска Академия на Науките.

Колаборацията работи върху оптимизирането на фотоинжектор за ЛСЕ за FLASH и XFEL, а изследванията са съсредоточени в измерване на напречното фазово пространство [2]. Поради ниската шумова и импулсна разделителна способност на използвания метод на маските, през периода 2006-2011 год. бе проектиран модул за Томография на Фазовото Пространство (ТФП) на електронния сноп. Този метод силно повишава разделителната способност на измерванията, тъй като дава възможност за измерване на отделни електронни бънчове, в две напречни полуравнини едновременно и с подобрено отношение на сигнал/шум. Трябва да се отбележи, че измерванията с ТФП се усложняват от ниските енергии от 25 MeV при заряд от 1 nC и малкия емитанс под 1 mm·mrad на фотоинжектора.

Дисертацията описва дизайна на модула за ТФП, разработени алгоритми за томографско реконструиране, приложението им при малък брой проекции използвани като входни данни и резултатите от първите измервания с него. Ограниченията на метода са проверени чрез реконструкции на фазовото пространство с проекции от числени симулации за целия диапазон енергия/емитанс на PITZ. За сравнение резултатите от ТФП измерванията са потвърдени с тези от метода на маските от две Emittance Measurement SYstems (EMSY), разположени преди и след модула в PITZ. Резултатите от томографските измервания показват нестабилност в динамиката на отделни импулси, която не може да бъде регистрирана с метода на маските поради осредняване на фазовото пространство на множество импулси. Показано е, че независимо от силното влияние на пространствения заряд и несиметричния и нееднороден напречен профил на електронния сноп, ТФП модулът изпълнява предназначението си и многократно подобрява разделителната способност на фазовото пространство на фотоинжектора.

Contents

Chapter 1

Introduction

The electromagnetic radiation emitted by ultra-relativistic electrons travelling through magnetic fields - synchrotron radiation - is characteristic with its wide energy spectrum, high intensity and coherence. Generated by bunched beams, the radiation has short pulsed nature down to the scales of nanometers, thus being applicable in areas necessitating high spatial and temporal resolution. Since its discovery in the second half of the 20th century, the synchrotron radiation has become a widely used source to study processes down to subatomic levels - biology, chemistry, material science, etc.

Whereas the first generation light sources have been delivering synchrotron light on parasitic basis jointly with high-energy physics experiments, nowadays there are dedicated facilities referred to as synchrotron light sources of fourth generation or Free Electron Lasers (FELs). In the contemporary FELs, the electron beam is passed through a periodic magnetic structure, an undulator, which modifies the straight beam trajectory into a sinusoidal one where the beam radiates at each bend. The figure of merit of the emitted radiation is its spectral brightness or brilliance. The brilliance is defined as the number of photons in $10^{-3}\omega$ frequency bandwidth centered around the angular frequency $\omega = energy/\hbar$, emitted by the source per second into a solid angle of 1 $mm^2 mrad^2$ surface [1]. The peak brilliance of the contemporary FELs based on Self Amplified Spontaneous Emission (SASE FELs) exceeds the one produced by the 'third generation light sources' by orders of magnitude - Fig. 1.1.

The definition of brilliance emphasizes not only on the photon flux but also on the high phase-space density of the radiating source. This high phase-space density, referred to as emittance, assumes that the particles, constituting the beam, occupy a small volume in the space defined by their spatial and momentum components. In other words, they are tightly packed in space and have very similar direction of flight. The transverse emittances for the horizontal and the vertical planes can be defined as if one looks towards the beam in its frame of reference and takes into account only the transverse components of the momentum and space. As the beam is frozen in its frame of reference and one looks from the side and accounts the longitudinal position of the particles within the bunch and their longitudinal momentum vector components, this area is referred to as longitudinal emittance. To be able
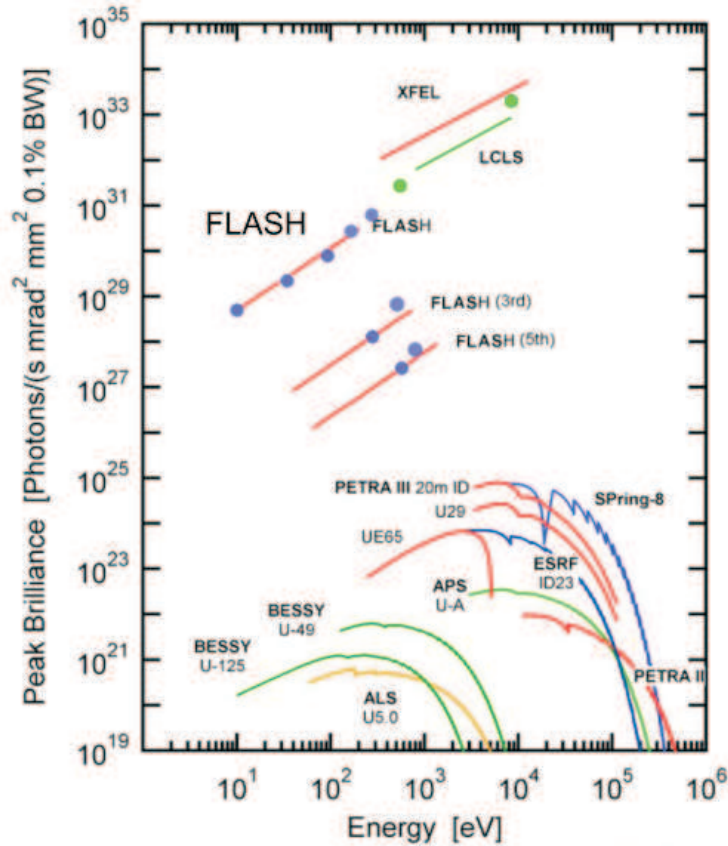
Figure 1.1: Peak brilliance of SASE FELs in comparison to the third generation light sources. The blue dots indicate the operating regime of the FLASH FEL at DESY, Hamburg. Image courtesy [1, 3].

to decouple the beam emittance from its energy, the emittance is multiplied by the product of the relativistic Lorentz factors $\gamma = \frac{E}{E_0}$ and $\beta = \frac{v}{c}$ for E, E_0, v and c being correspondingly the total energy, the rest mass energy, the particles velocity and the speed of light in vacuum. This quantity is defined as normalized emittance.

As it will be described in the following, the FELs operating in SASE regime require round beams with small normalized transverse emittance at the entrance of the undulator magnets and high peak current in the order of a few kA. Machines which can constantly deliver parameters in such ranges are proven to have single-pass geometry like the one shown in Fig. 1.2. Moreover, the injector part usually constitutes of a laser-driven photocathode electron source capable of producing beams with brightness two orders of magnitude higher than in standard thermionic guns [4]. To minimize shot-to-shot fluctuations of the beam quality, dedicated diagnostic sections are installed along the beamline and operated quasi-parasitically to the user runs, whereas the injector part is desirable to be optimized in a stand alone facility. Such is the case with the currently operating Free-electron LASer in Hamburg (FLASH) and the future European X-ray FEL (XFEL), both at DESY. The Photo-Injector Test facility at DESY, Zeuthen site (PITZ), is used as a test stand for research and optimization of the injector setup for those two machines.

In the following part of this introduction some basic principles of an FEL are described as requirements for the beam quality are given at the end. Chapter 2 introduces PITZ as a photo-injector test facility. Basics of the photo-injector phase space and beam optics, needed in order to be able to perform tomography studies, are given in Chapter 3. The next Chapter 4 encompasses the theory behind tomography and several reconstruction algorithms are discussed. How tomography can be applied in the field of beam dynamics is also a topic of this section whereas the specific application in PITZ is discussed in Chapter 5. The final part of this work is dedicated to experimental results and their validity.

Free Electron Lasers

This section introduces some basics of FELs. Derivation of the used formulae and further details can be found in [5–7].

An FEL consists of an RF photo-cathode or a special thermionic gun where the particles are extracted from the source and initially accelerated, followed by a number of further accelerating modules. This section is referred to as an injector. Bunch compressors might be installed between the accelerating modules in order to longitudinally compress the bunch and consequently increase its peak current. Undulator magnets and transfer lines, guiding the radiation to photon experiments, are situated near the end of the setup. Behind the undulator, electrons and photons are separated by a bending magnet, guiding the electrons towards a beam dump. Diagnostics components are typically located in the sections where control of the beam quality parameters is needed, e.g. around bunch compressors or in the sections where the final energy has already been achieved. A simplified schematics layout of a single-pass machine is shown in Fig. 1.2.
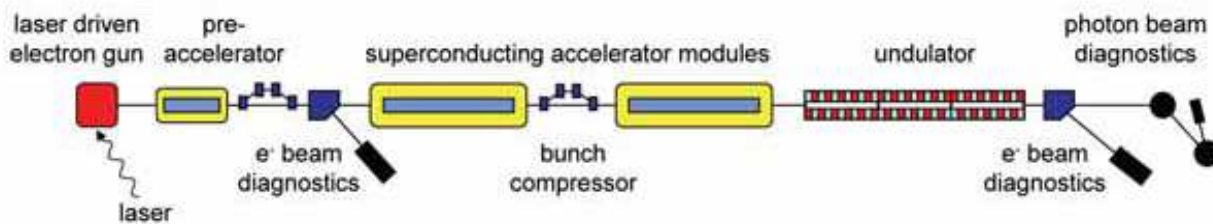
Figure 1.2: Simplified single-pass FEL layout. Major components are the photo-cathode RF gun, accelerating modules, bunch compressors, undulators, transfer lines guiding the FEL radiation to dedicated experiments and a beam dump. Image courtesy to [1].

The undulator magnet generates a magnetic field through which the electron beam propagates. On the sinusoidal trajectory, defined by the undulator, the electrons emit synchrotron radiation in a narrow cone in the forward direction. Some of the particles lose energy and are slipping back with respect to the electromagnetic wave, travelling a longer path along the undulator, while others gain energy. This process depends on the relative phase between

the electromagnetic wave and the electron oscillations. Energy from the electron beam is transferred to the photon beam if the wavelength of the photon beam λ satisfies [6]

$$\lambda = \frac{\lambda_u}{2\gamma^2}\left(1 + \frac{K^2}{2}\right),$$

(1.1)

where λ_u is the undulator period, i.e. the distance between two identical in polarity magnets - Fig. 1.3. K is the dimensionless undulator parameter [6]
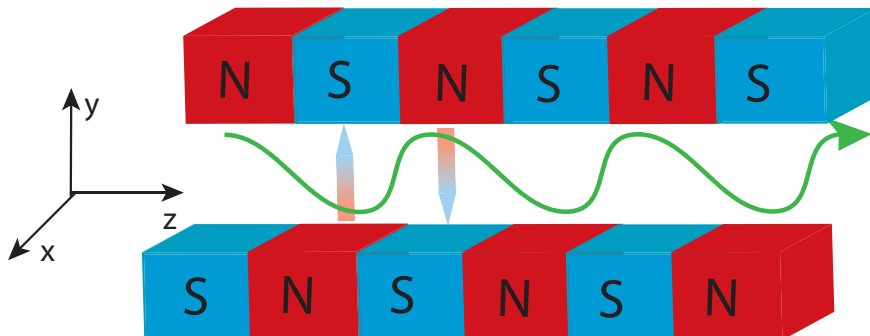
Figure 1.3: Planar undulator top view with oscillating orbit of the propagating beam shown in green. The arrangement of permanent magnets with alternating polarity generates a magnetic field in the vertical direction, varying sinusoidally along the z-axis. The longitudinal distance between two magnets with identical polarity is the undulator period λ_u.

$$K = \frac{qB_u\lambda_u}{2\pi m_e c},$$

(1.2)

as B_u is the peak magnetic field, q - the elementary charge, m_e - the electron rest mass and c - the speed of light in vacuum. Radiation with this λ is amplified. The energy variations induce longitudinal density modulations inside the travelling bunch of the order of the radiation wavelength λ, known as microbunching. Those modulations exponentially amplify the power of the emitted light where, eventually, all the particles lose energy and saturation occurs. In general in saturation the amplification ceases and the power drops.

Eq. (1.1) shows that the radiation wavelength, which will be amplified, is a tunable parameter. Nevertheless the design is optimized in order to reach the shortest possible wavelengths down to the sub-nm regime - changing the wavelength is feasible by varying the input beam energy or the undulator parameter. Energy variations are limited by design constraints. The K-parameter can be altered by changing the gap height between the two horizontal planes of the undulator and thereby the peak magnetic field.

The power of the emitted radiation in SASE regime $P(z)$ initially increases exponentially with the distance along the undulator z [8]

$$P(z) \propto P_{in}e^{\frac{2z}{L_g}}.$$

(1.3)

The length needed for $P(z)$ to increase by a factor of e is defined as the gain length [6]

$$L_g \propto \sqrt[3]{\frac{\sigma_r^2}{I_{peak}}},$$

(1.4)

where σ_r is the transverse beam size. To obtain short gain length, the peak current I_{peak} should be high and the transverse beam size has to be kept small or otherwise saturation cannot be reached within the finite length of the undulator. As an example consider Fig. 1.4 where simulated data has been superimposed to measurements from the FLASH facility [9].
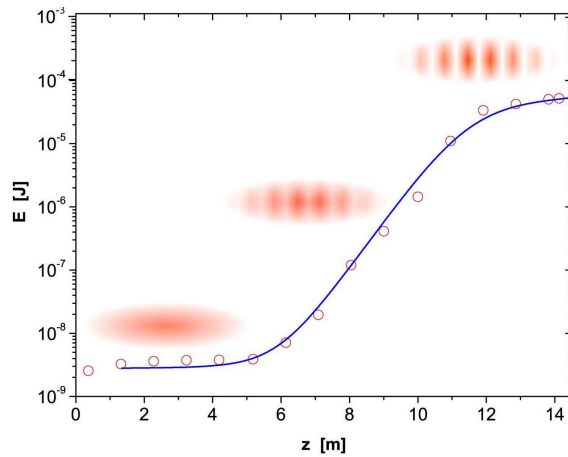
Figure 1.4: Exponential growth of SASE radiation power as a function of the distance along the undulator until saturation. The red circles represent data from FLASH with beam energy of 245 MeV. The solid blue curve is obtained with simulations. Image courtesy to [9].

The minimim reachable radiation wavelength, within constant approximation, is defined by [5],

$$\lambda_{min} \propto \Delta E \sqrt{\frac{1 + \frac{K^2}{2}}{\gamma B_n K^2}},$$

(1.5)

as here ΔE is the input beam energy spread and its brightness is defined as [5]

$$B_n = \frac{2I_{peak}}{\varepsilon_n^2}$$

(1.6)

with ε_n being the normalized emittance of the electron beam [5]. Therefore, short-wavelength FELs require minimized energy spread as only particles in a narrow energy band would contribute to the FEL process. This can be seen also in Eq. (1.1): the relation $\lambda \propto \frac{1}{\gamma^2}$ shows that the bandwith of the emitted light depends on the momentum spread of the source. If there are particles with different momenta there will be a range of wavelengths amplified. In order to reduce this effect the beam momentum spread has to be minimized.

At the same time the brightness has to be as high as possible, thus there is a constraint on small normalized transverse emittance and high peak current. The high charge density

and the small emittance from the last equation are to a great extent opposing to each other since high density would give rise to strong electric forces within the beam and consequently distort the beam quality defined by the emittance. The beam emittance and the photon wavelength are related in the so called coherence condition [6]

$$\varepsilon_n < \frac{\gamma \lambda}{4\pi}, \tag{1.7}$$

according to which short wavelengths are achievable only if the normalized transverse emittance is small.

Some of the design parameters for the European XFEL as it is planning to operate at a wavelength of 0.1 nm are listed in Table 1.1. While the peak current can be increased by a

Table 1.1: Original main parameters of the XFEL [1].

Electron beam energy	17.5	GeV
Bunch charge	1	nC
Bunch peak current	5	kA
Bunch length	20	μm
Relative energy spread $\frac{\Delta E}{E}$	1.2×10^{-4}	-
Slice energy spread at the undulator	1	MeV
Slice emittance at the undulator[a]	1.4	mm·mrad

[a]transverse emittance of a longitudinal part of the bunch

factor of 100 in the aforementioned bunch compressors along the beamline, the emittance can only degrade starting from the source. Therefore the emittance requirements at the injector section are even more stringent. With some safety margin for the emittance degradation from the source to the undulator, the originally specified requirement for the projected beam emittance in the XFEL injector region is 0.9 mm·mrad [10]. With the LCLS result that the slice emittance from the electron source does not degrade significantly until the beam reaches the undulator [11] and with the demonstration that low emittance beams can be generated at PITZ [2], the beam parameters for the XFEL were revised in 2010. Even though the 17.5 GeV linac will be build, now one considers that also an operation with a beam emittance of 1 mm·mrad at a total beam energy of 14 GeV will be possible without deteriorating the properties of the emitted FEL radiation.

Conclusions

Some basic FEL features and requirements were introduced in this chapter. It was shown that the transverse emittance of the electron beam is of great importance in order to reach high brightness and short wavelengths and it needs to be optimized from the source. For that purpose FLASH and the XFEL are using PITZ as a test bench where the sources - the

electron guns - are characterized. This thesis describes the functional implementation of a module for phase-space tomographic diagnostic at PITZ, including:

1. physics design of the module for the PITZ parameter space of beam momentum of 15–40 MeV/c, nominal bunch charge of 1 nC and emittance in the transverse planes smaller than 1 mm·mrad at the injector exit;

2. choice of an algorithm for tomographic reconstruction, suitable for limited set of projections used as input data;

3. commissioning of the module and proof of principle measurements with it.

These objectives determine the following tasks to be worked out:

1. choice of an optimal set of matching and FODO quadrupoles according to the layout of PITZ beamline;

2. a future installation of an RF deflecting cavity for longitudinal phase-space measurements has to be considered in the geometry of the tomography module and its preceding matching section;

3. possible space-charge effects, characteristic for the above listed beam momentum, bunch charge and emittance, should be considered;

4. development of software procedures for automatic analysis of numerical simulations needed for the physics design of the module;

5. development of software procedures for automatic data taking and analysis of experimental data;

6. definition of criteria for an incorrect measurement;

7. measurement and calibration of the quadrupole magnets in the module;

8. development of a measurement procedure.

These tasks were realised in the period between years 2006 and 2009. The tomography module was installed by November 2010 and its functionality was experimentally proven with bunch charges 100 pC – 1 nC and momentum of 25 MeV/c.

Chapter 2

Photo-Injector Test Facility at DESY in Zeuthen

The Photo-Injector Test Facility at DESY in Zeuthen (PITZ) is build to develop, operate and characterize electron sources meeting the requirements for Free Electron Lasers (FELs) operated in the Self Amplified Spontaneous Emission regime (SASE-FELs) as FLASH and the European XFEL [12]. These requirements include a projected transverse emittance below 1 mm·mrad, an rms bunch length below a few mm and a nominal bunch charge of 1 nC [10]. As an inital stage of the PITZ project, the first fully characterized RF gun cavity has been installed at the Vacuum Ultra Violet - Free Electron Laser (VUV-FEL) at DESY in Hamburg in 2003. In 2009 another gun cavity, currently installed at FLASH, has been characterized with maximum gradient at the cathode plane of 60 MV/m.

This chapter gives an overview of the physical setup of the photo-injector test facility. First, the basic module is described, namely the gun section, followed by the beam diagnostics available at PITZ. An additional diagnostics component installed in 2010 - a module for phase-space tomographic diagnostics, is the main subject of this work. Design considerations of the tomography setup and its expected performance are discussed in Chapter 5.

A simplified overview of the current setup is shown in Fig. 2.1. As it can be seen there, the accelerating part of PITZ consists of a laser-driven RF gun and a booster cavity. To be able to achieve minimal transverse emittance from the photo-injector, the accelerating gradient in the gun cavity has been increased from approximately 43 MV/m in the first gun to 60 MV/m now. A magnetic field produced by a main solenoid is used to focus the electron beam and a bucking coil compensates the magnetic field at the cathode and thus minimises the residual angular momentum of the electrons. The beam is accelerated further to energies up to a maximum of about 30 MeV by a normal-conducting Cut-Disc Structure type booster cavity. Diagnostic components are installed in both sections - the low-energy one downstream the gun cavity, and in the high-energy section downstream the booster cavity. The diagnostic includes three emittance measurement systems, a low-energy and two high-energy dispersive arms, observation screens for transverse spot size measurements and
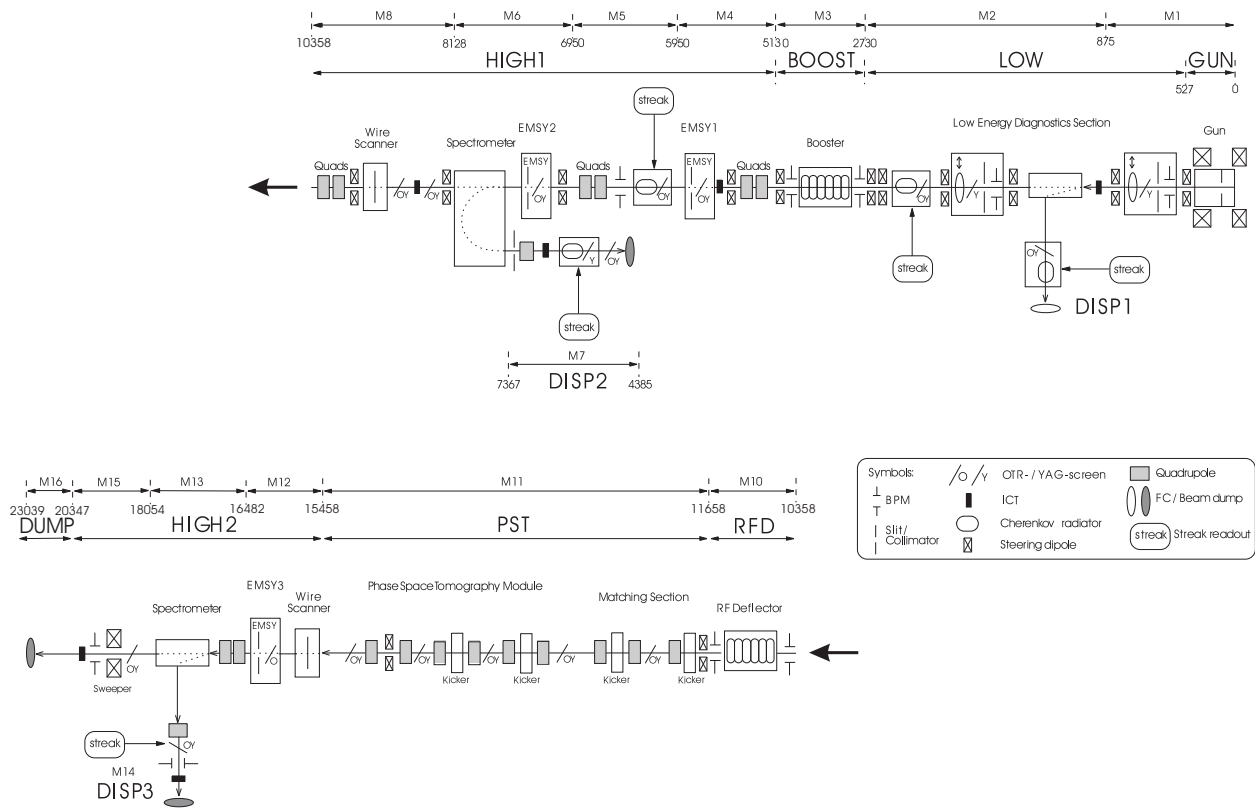
Figure 2.1: Schematic PITZ layout. The electron beam propagates from right to left. The kicker magnets and the RF deflecting cavity are still not installed.

charge measurement devices. A module for transverse phase-space tomographic diagnostics is situated in the second part of the beamline. More detailed descriptions of the modules follow below. Table 2.1 shows some nominal parameters and the range of the possible PITZ parameter space.

Table 2.1: Main PITZ parameters range.

Parameter	Nominal value	Max value	Units
Accelerating gradient at the cathode	60	$\leq$60	MV/m
Beam momentum after initial acceleration	6.8	$\leq$6.8	MeV/c
Final beam energy with CDS booster	25	$\leq$30	MeV/c
Bunch charge	1	$\leq$3 [a]	nC
Bunch peak current	50	-	A
Bunch length	20	$\leq$24	ps

[a]as measured with laser settings in winter 2009

10

2.1 Laser system

One major feature of the photoemission on which PITZ is based is that the emitted particle beam inherits the characteristics of the laser beam - in this way short bunches with high charge can be produced. The current PITZ laser, developed by the Max Born Institute, Berlin [13], is designed to fulfill requirements imposed by beam dynamics simulations showing that minimum transverse emittance can be achieved with a flat-top temporal laser profile having about 20 ps FWHM pulse duration and 2 ps rise and fall times [10, 14].

The laser system consists of a Yb:YAG laser, a pulse train oscillator and an amplifier system, a transport beamline and diagnostics. The laser is able to generate pulse trains with a repetition rate of 10 Hz with up to 800 micropulses. The spacing within a pulse train is 1 μs. The final laser wavelength is $\lambda = 257$ nm. The system is directly synchronized to the 1.3 GHz resonance frequency of the gun cavity by a master oscillator.

The temporal properties of the pulse are measured by an optical sampling technique on the laser table called OSS here. The resolution of the system is 1 ps. Additionally a streak camera Hamamatsu C5680 can be used but its resolution is limited to about 2-4 ps.

The laser energy at the photocathode can be adjusted from 0 nJ up to a few hundred nJ by adjusting the transmission level.

The laser beam with tansverse Gaussian distribution is transported to the tunnel over an optical path of approximately 25 m - see Fig. 2.2, and a central uniform part of it is cut out by a beam shaping aperture (BSA) before illuminating the Cs_2Te photocathode. The
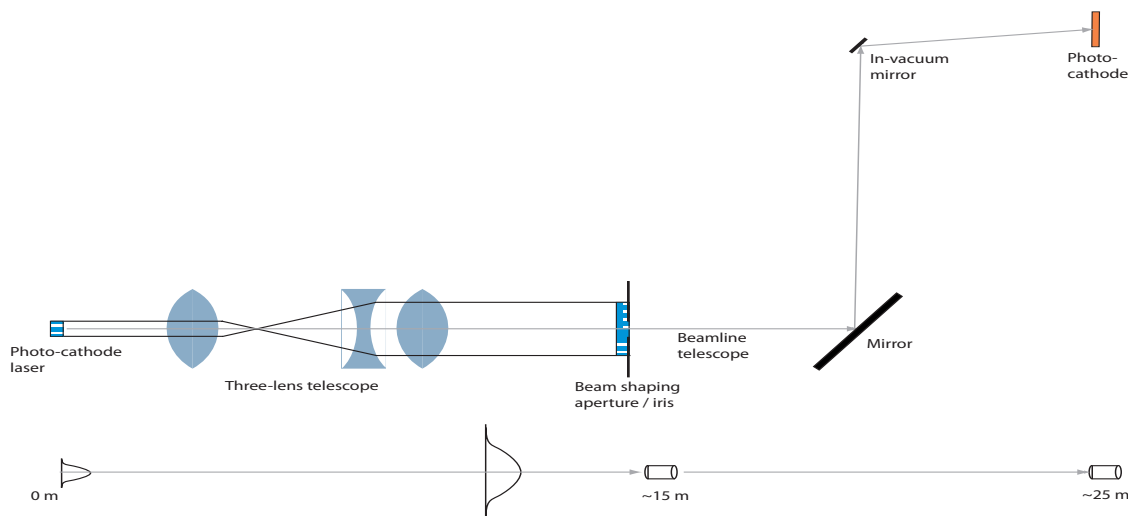
Figure 2.2: Layout of the laser beam line.

transverse size of the laser beam at the photocathode is controlled with the diameter of the BSA. The imaging from the laser table to the plane of the BSA consists of a telescope of three lenses with magnification of 6.5. A mirror located behind the BSA deflects the laser beam towards an in-vacuum mirror which guides the laser light to the photocathode. A second imaging system with unit magnification consisting of four lenses located behind the

BSA, not shown in Fig. 2.2, images the laser onto the photocathode.

In order to monitor the transverse properties of the spot, the already shaped laser beam can be deflected and imaged on a number of so called virtual cathodes (VCs) working in different ranges of the pulse energy. The VCs are located on a dedicated diagnostics table between the aforementioned mirrors as the optical path from a splitter to a VC is identical with the one to the real photocathode. Two of the VCs which are directly illuminated by the laser light are UV sensitive CCD chips. A typical spatial distribution of the laser beam can be seen in Fig. 2.3(a). Fig. 2.3(b) shows a temporal laser profile measured with the optical sampling technique.
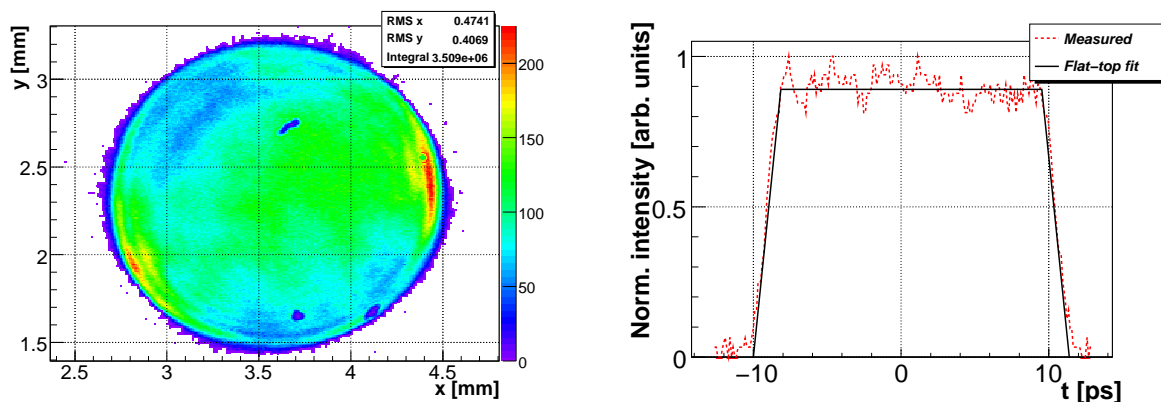
(a) Transverse profile of the laser spot on one of the virtual cathodes.

(b) Temporal laser profile having 19.7 ps FWHM with 1.9 and 1.8 ps rise and fall times correspondingly. The profile is measured by the OSS.

Figure 2.3: Transverse (left) and temporal (right) laser profiles.

A photomultiplier and laser pulse energy meter are used to monitor the laser energy [15]. The position jitter can be monitored using a quadrant diode [16].

2.2 Gun section

The PITZ gun section consists of a $1^1/_2$ cell π-mode RF gun cavity, resonating at a frequency of 1.3 GHz, main and bucking solenoids. An overview of the setup is shown in Fig. 2.4. On the back wall of the half cell of the gun cavity a photocathode is positioned.

2.2.1 Photocathode

Major requirements towards the cathodes used in operation are the capability of long bunch train generation and high charge extraction, i.e. short response time and high quantum efficiency (QE), combined with uniformity and long lifetime of the photoemissive layer. Semiconductors like Cs_2Te have the required high QE and fast response time as at the same time, due to high sensitivity to remnant gases, they require ultra high vacuum conditions [17, 18].
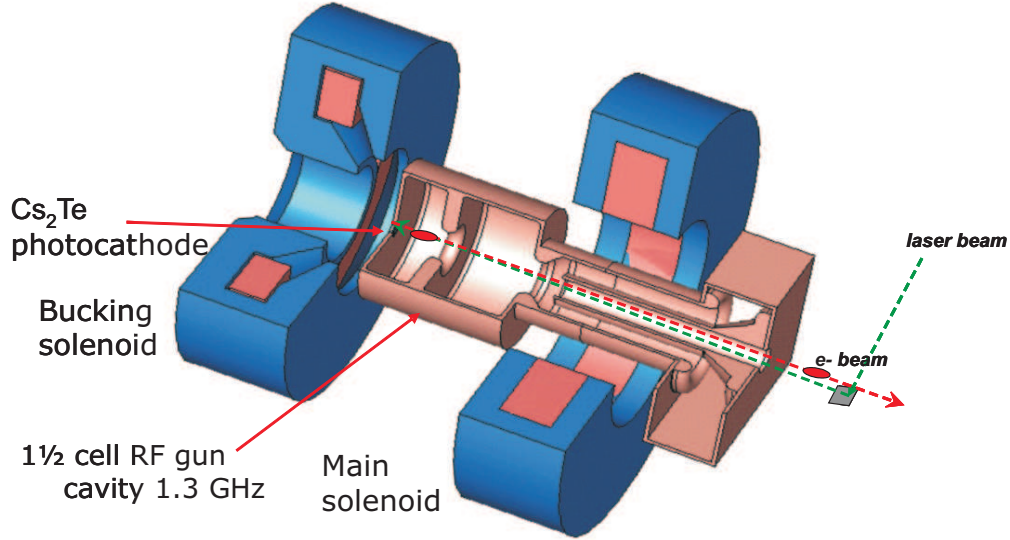
Figure 2.4: Layout of the gun, main and bucking solenoids correspondingly on the right and the left hand side.

PITZ uses Cs_2Te photocathodes which are produced by LASA, INFN-Milano [19]. The photoemissive layer of a few tens nm thickness and a diameter of 5 mm is deposited on a polished Molybdenum substrate. First Te and afterwards Cs is deposited on the Te until the quantum efficiency, monitored during this process, reaches a maximum [20].

In the run period of summer-autumn 2008, the QE was measured to be of the order of 5% for each newly inserted photocathode.

2.2.2 RF gun cavity

UV laser light illuminates the Cs_2Te photocathode located on the back wall of the half cell and thus produces photoelectrons which are accelerated up to a maximum energy of about 6.8 MeV. The launching phase of the laser, the laser emission time with respect to the RF wave, is chosen so that it delivers maximum energy gain. The highest possible electric field on the cathode, E_0, delivers maximum acceleration according to the relation

$$E_0[MV/m] \propto \sqrt{P_f[MW]}, \tag{2.1}$$

where P_f stands for the peak forward power in the cavity. High E_0 reduces the emittance blow-up due to self-fields of the electrons [21]. The constant of proportionality depends on the shunt impedance which determines the maximum power dissipated on the cavity walls [22]. For a particular gun cavity, used in PITZ, the constant of proportionality has been estimated to be 23.336, and the required peak forward power is calculated to be about 6.6 MW for an accelerating gradient of 60 MV/m [21]. Powered by a 10 MW klystron, a sine-like modulated microwave is fed into the gun via waveguides and an on-axis RF coupler.

Part of the waveguide is filled with pressurized SF_6 to suppress sparks.

Due to thermal expansion, the volume of the cavity changes during operation and thus the resonant frequency drifts from the above mentioned 1.3 GHz. A devoted water cooling system is used to compensate for the heating and to obtain a fine tuning of the gun.

Gun prototype $\sharp 4.1$, whose geometry and gradient are shown in Fig. 2.5, is used for the simulations and measurements shown here. It has been conditioned to operate with
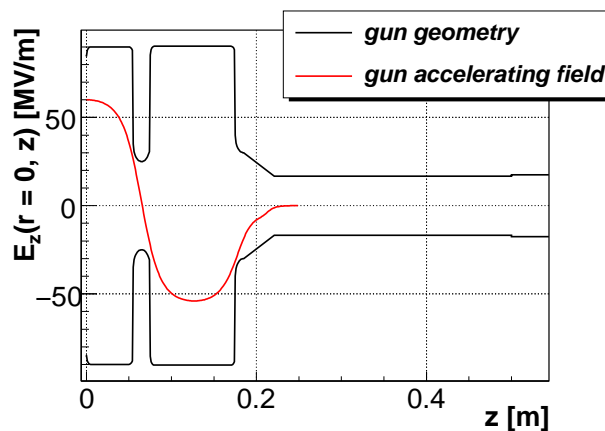
Figure 2.5: Gun geometry and gradient as used in simulations.

maximum accelerating gradient of 60 MV/m or 6.25 MW peak power, 10 Hz repetition rate and 700 μs RF pulse duration in 2010 [23]. Thus, the maximum mean power stored in the cavity is about 44 kW. The water cooling system of the gun cavity consists of 14 channels with separately adjustable flow. In addition, prior to operation, a dry-ice cleaning technique has been applied [23]. 18 temperature sensors, located on the gun walls and at the iris, are delivering control information.

2.2.3 Solenoids

After being emitted, the photoelectron beam is focused by the main solenoid positioned just after the gun body as shown in Fig. 2.4. The purpose of this magnet is to focus and to control the evolution of the beam envelope since at low energies the beam is strongly divergent due to self-forces of the particles.

The position of this solenoid is chosen so that its peak field is at 0.276 m from the cathode - blue curve in Fig. 2.6. The peak field is 0.29 T at a current of 500 A. The relation between the current and the magnetic field is [24]

$$B_{z,main}[T] = 5.893E\text{-}4[T/A].\ I_{main}[A] - 1.169E\text{-}5[T].$$

The tail of the main solenoid field extends to the cathode position and therefore a second solenoid - bucking, is used to compensate it. Otherwise there will be some magnetic emittance contribution due to uncompensated transverse momentum component. The polarity of the
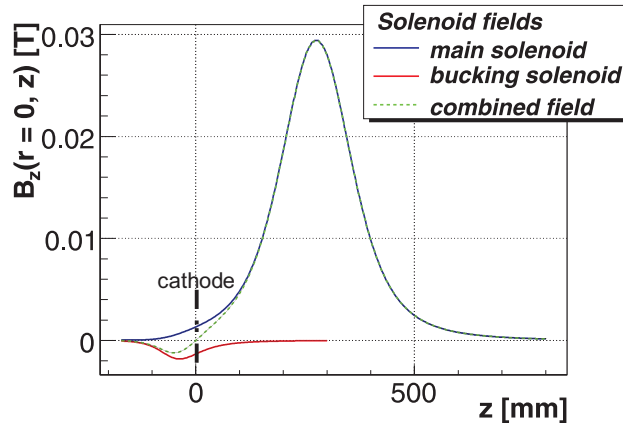
Figure 2.6: Longitudinal components of the main (blue dashed), bucking (red) and the resulting sum (green dashed) solenoidal magnetic fields. The cathode position (z = 0 m) is highlighted by a black dashed line.

bucking solenoid is opposite to the one of the main solenoid and the compensating factor obeys the equation

$$\mathrm{B_{z,buck}[T]} = -1.403\,\mathrm{B_{z,main}[T]} - 6.562\mathrm{E}\text{-}2. \tag{2.2}$$

The longitudinal components of the fields of the main and the bucking solenoids and the resulting superposition are shown in Fig. 2.6.

2.3   Booster cavity

Further acceleration of the electron bunch is necessary in order to conserve the emittance. A booster cavity can be placed at a certain distance downstream the gun where the beam is at laminar waist, i.e. the transverse beam size is minimized. The entrance of the cavity coincides with the $z-$position of this waist [10,25]. The energy gain in the booster cavity, $\frac{d\gamma}{dz}$, is chosen so that, for defined RF phase and solenoid current, the beam envelope is matched to the so called "invariant envelope" or

$$\frac{d\gamma}{dz} = \frac{2}{\sigma}\sqrt{\frac{I_{peak}}{3I_0\gamma}}, \tag{2.3}$$

where σ is the rms size of the incoming beam, I_0 - the Alfven current (1.7 kA for electrons). More detailed explanation of the invariant envelope theory can be found in [10, 25].

   PITZ uses a 14-cell Cut-Disc Structure (CDS) cavity [12,26] with which beam momentum of about 40 MeV/c can be reached at maximum design accelerating gradient of 14 MV/m. About 25 MeV/c is the momentum for nominal operating conditions. Installation of this booster is essential for the performance of the here discussed tomography section since otherwise the beam divergence does not allow successful matching of both transverse planes to the layout of the magnetic lattice. This issue is discussed in Chapter 5.4.2.

2.4   Beam diagnostics

As one of the PITZ major goals is defined as characterization of the electron sources for FEL machines, the beamline is equipped with various diagnostics devices for measuring beam parameters like orbit, momentum and momentum spread, bunch length and charge, longitudinal phase-space distribution, transverse shape and projected emittance, etc. Some devices, like emittance measurement stations, are located only in the high-energy section - behind the booster cavity, while others are also in the low-energy section between the gun and the booster cavities.

Bunch charge

Permanent monitoring of the bunch charge is performed with the help of Integrating Current Transformers (ICT) in both low- and high-energy sections. ICTs allow non-destructive charge measurement but they are not sensitive enough for charges much below 100 pC. The uncertainty of the device is about 30 pC. In addition, copper Faraday Cups (FC) are used. Their uncertainty is estimated to be about 2 pC [2].

Electron beam transverse distribution

An observed beam spot or projections of it are the primary source of information about the beam transport along the linac and its transverse and longitudinal properties. Even though observation screens are interceptive devices and are not favoured in user facilities, in PITZ, being a test facility, they are heavily used.

There are two types of screens along the beamline [27] - Yttrium-Aluminum-Garnet (YAG) and Optical Transition Radiation (OTR). Ce doped YAG powder on a Si substrate is used as scintillating material with its thickness varying between 5 and 20 μm. The OTR screens are foils with aluminum coating. The YAG screens are mounted with normal incidence towards the beam, followed by 45° mirrors deflecting the light out of the vacuum pipe. The OTRs, being mirrors, are inclined at 45° towards the beam axis. As it will be discussed later, the screen stations along the tomography module are equipped with both types of screens.

In all screen stations the light is deflected towards a CCD camera readout by a system of mirrors. A number of screen stations are equipped with magnifying lenses with focal lengths between 100 and 250 mm, providing magnification between 0.25 and 0.1 with respect to the screen dimensions, as only one lens can be inserted at a time. The resolution is improved by reducing geometrical aberrations with the help of diaphragms mounted on each lens. Additional pneumatically movable mirrors are used to change the optical path towards a calibration grid, attached on a separate holder outside the beamline. The estimated optical resolution is 30 lp mm^{-1} [27].

Currently two types of monochrome CCD cameras are used [28] - analog (8 bit resolution)

and digital (12 bit resolution), both externally triggered by the main trigger module. The analog cameras are JAI M10SX and M10RS [29], with chip dimensions of 768×574 square pixels of 8.3 μm size. The digital cameras - Prosilica GE 1350 and GC 1350 [30], provide resolution of 1360×1024 but in PITZ neighbouring pixels are combined to dimensions of 680×512 in order to increase the signal to noise ratio due to a decreased read noise. A TINE protocol [31] is integrated on the control system software communication level. Custom videokernel libraries, supported for 32- and 64-bit CPU architecture, are provided for client applications. Specific camera properties like integration time, gain, etc. can be remotely adjusted via control servers [28].

Another type of devices used for beam profile measurements are the wire scanners. Currently there are two wire scanner prototypes for FLASH used in PITZ. Physically it is a fork with two independent scanning tungsten wires of 30 μm diameter having 10 mm distance between them [32]. A scintillation counter is used to detect radiation, emitted as a wire crosses the beam and scatters the primary electrons. Tests have shown that beams with a charge down to a few pC can be measured. The speed of the movement of the wires - 5 μm/s to 1 m/s, combined with big transverse dimensions of the beam, cannot provide single bunch measurement, but nevertheless, wire scanners can be used when the heat load can destroy screen stations.

Beam position

Alongside with the screen and wire scanner stations described above, Beam Position Monitors (BPMs) are used to monitor the beam orbit along the beamline. BPMs are non-interceptive devices where the passing beam induces current on a number of antennae pick-ups. A beam displacement from the center of the vacuum pipe, assuming the antennae of the BPM are correctly aligned and calibrated with respect to the axis of the pipe, will induce a different amount of current on the opposite antennae and thus, the center of mass of the beam will be revealed as displaced. The BPMs in PITZ are of button type, able to measure a transverse offset with a precision of 30 μm [2].

Longitudinal beam properties

Characterization of the longitudinal phase space includes measurements of the beam momentum, momentum spread, bunch length and the longitudinal phase-space distribution itself. There are three sections along the beamline for those purposes - low-energy dispersive arm (LEDA) downstream the gun, and two high-energy dispersive arms - HEDA1 and HEDA2, downstream the booster cavity.

The mean momentum and momentum spread are measured with spectrometer dipole magnets in the three sections. The dipole magnet deflects the electron beam through a fixed radius of curvature defined by its geometry and the position of the screen where the distribution is observed. When two different parts of the bunch have different energies the

corresponding particles have different paths through the magnetic field. Thus, projected onto an observation screen behind the magnet, the momentum distribution is tranformed into a spatial distribution in the plane of dispersion.

The dipole for LEDA is a 60° bending magnet installed at about 1 m downstream the gun. HEDA1, located at about 7 m from the cathode, incorporates a 180° dipole magnet with bending radius of 300 mm. HEDA2, positioned at the end of the beamline, is currently under installation.

Bunch length and longitudinal phase-space distribution measurements can be performed in LEDA, HEDA1 and HEDA2 as all of them are equipped, or planned to be, with streak readout systems and reference screens in the straight sections. The temporal bunch shape is tranformed into a corresponding light distribution with the help of Cherenkov radiation in a Silica aerogel or using OTR screens, depending on the beam energy. More details on those systems can be found in [33–35].

HEDA2, in combination with a future RF deflecting cavity, will also be used for longitudinal phase-space studies including high resolution slice momentum spread measurements. The RF deflecting cavity will have the purpose to deflect the electron bunch vertically and, thus, introduce a correlation between the longitudinal and the vertical coordinates. Further details on the setup and the measurement idea can be found in [36, 37].

Transverse emittance

Characterization of the electron source requires measurements of the transverse and longitudinal properties of the beam during its evolution. There are three dedicated Emittance Measurement SYstems (EMSY) [38–41] located at different distances downstream the booster cavity. The EMSYs are designed for usage at energies of the electron beam between 5 and 30 MeV. Each EMSY has a horizontal and a vertical actuator with mounted slits of 10 and 50 μm openings, both orthogonal to the beam axis, a YAG and/or an OTR observation screen. One or more emittance dominated beamlets, created by the slits, are observed on a screen located after a drift further downstream. The drift length between the slit and the observation screen is different for each EMSY. It is chosen so that space-charge forces do not degrade the beamlets and good signal-to-noise ratio in a combination with good resolution are obtainable [39]. In PITZ different drifts are used for thermal emittance measurements and for standard ones with 1 nC bunch charge.

Each of the actuators carrying the slits is movable by a linear stage with a precision of 5 μm. The angular acceptance of a slit can be maximized by a rotational stage and a goniometric cradle for the two transverse planes with a precision of 2 mrad.

The three stations have been commissioned in 2005 and the first measurement with all of them have been performed in the autumn of 2006. Further details on the design, the measurement procedure and results can be found in Ref. [38–42].

Transverse slice emittance measurements can be performed also with HEDA1 and HEDA2.

The measurement principle constitutes of introducing a linear correlation between the longitudinal position of the particles within the bunch and their momentum by proper phasing of the booster cavity. Afterwards the momentum distribution is transferred into a spatial one by a dipole magnet. Finally, the transverse emittance in the plane perpendicular to the bending plane is measured for momentum ranges corresponding to different temporal slices. Details on the design of the setups can be found in [36, 43–45].

Additionally, the PITZ beamline is equipped with a tomography module for transverse emittance measurements using multiscreen method and tomographic reconstruction. Details on its design considerations and expected performance are subject of this work and will be discussed in Chapter 5 and Chapter 6.

Conclusions

The Photo-Injector Test Facility at DESY in Zeuthen was introduced in this chapter. The following points were discussed:

1. PITZ parameter space;

2. major components of the machine - the laser system, the gun and the booster cavities, the solenoid magnets;

3. devices for beam diagnostics; references describing in details those modules were given.

Chapter 3

Transverse beam dynamics in a linear accelerator

To describe the motion of an ensemble of N particles, travelling approximately in the same direction and inclination with respect to an ideal reference particle which propagates along the accelerator axis with a certain design momentum, it is convenient to introduce a right-handed cartesian coordinate system as shown in Fig. 3.1. Each particle within this ensemble
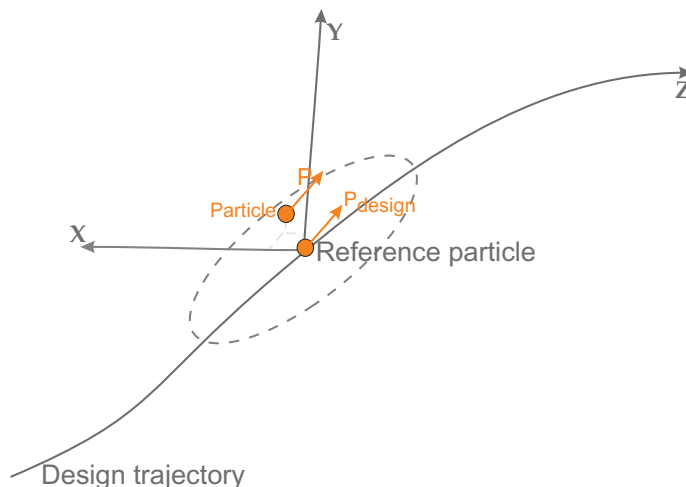
Figure 3.1: Design trajectory and coordinate system.

can be described by its three spatial coordinates $\vec{r} = \{x, y, z\}$ and its three canonical momentum components $\vec{p} = \{p_x, p_y, p_z\}$. By the definition of the paraxial approximation, namely $\frac{p_{x,y}}{p_z} \ll 1$, if those N particles are concentrated in a relatively small volume in the 6-dimensional phase space defined by $\{\vec{r}, \vec{p}\}$ they are considered to be a particle beam. The beam state can be represented by a phase-space density function $\rho\left(\vec{r}, \vec{p}\right)$. If the transverse to longitudinal coupling can be neglected, the phase space can be decomposed to a four-dimensional transverse - (x, p_x, y, p_y), and a two-dimensional longitudinal - (z, p_z) phase space. Finally, the dimensionality of the transverse phase space can be reduced to two two-dimensional motions, orthogonal to the longitudinal one [46]. In beam physics, the angle,

21

defined by any transverse and the longitudinal component of the momentum, is of more practical interest. The angle θ_x is defined as

$$\tan\theta_x = \frac{dx}{dz} = \frac{p_x}{p_z} = \frac{\gamma m_0 \dot{x}}{\gamma m_0 \dot{z}} = x'. \tag{3.1}$$

Thus, (x, x') define the so called transverse trace space for the horizontal plane. (y, y') is defined in the same manner.

For analytical reasons the beam dynamics theory uses the statistical distribution of the beam, i.e. its second moments. If the beam distribution is characterized by the density function $\rho(x, x')$, its second moments are defined using [25]:

$$\langle x^2 \rangle = \frac{\int x^2 \rho(x, x')\, dx dx'}{\int \rho(x, x')\, dx dx'} - \left(\frac{\int x \rho(x, x')\, dx dx'}{\int \rho(x, x')\, dx dx'} \right)^2,$$

in the same way $\langle x'^2 \rangle$ and $\tag{3.2}$

$$\langle xx' \rangle = \frac{\int xx' \rho(x, x')\, dx dx'}{\int \rho(x, x')\, dx dx'} - \frac{\int x \rho(x, x')\, dx dx' \int x' \rho(x, x')\, dx dx'}{\times \left(\int \rho(x, x')\, dx dx' \right)^2}.$$

Thus, the beam rms size is $\sigma_x = \sqrt{\langle x^2 \rangle}$ [mm], the angular spread, called divergence is $\sigma_{x'} = \sqrt{\langle x'^2 \rangle}$ [mrad] and the covariance, also called coupling term, $\sigma_{xx'} = \sqrt{\langle xx' \rangle}$ [mm· mrad]. In general, the particles in a two-dimensional phase space can be enclosed in a phase-space
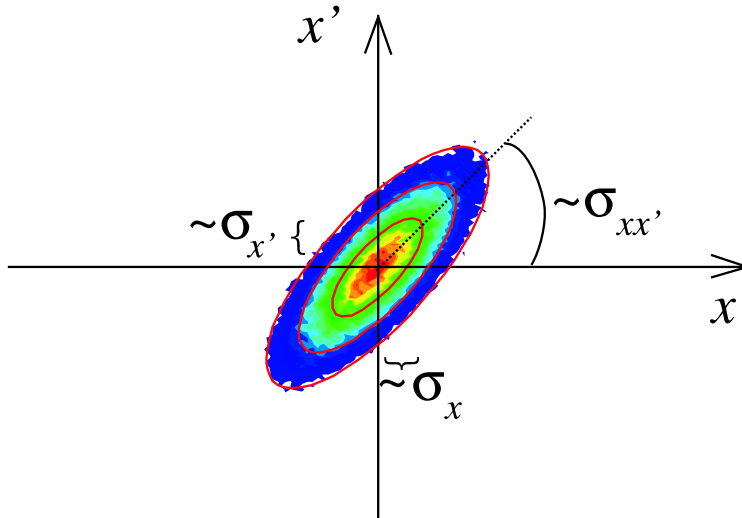

Figure 3.2: Transverse phase space in (x, x') plane, x is the transverse coordinate, representing the beam size, and x' - the angular divergence. The angle of inclination of the ellipse is given by the covariance $\sigma_{xx'}$.

ellipse [47], and from Fig. 3.2 it can be seen that $\sigma_{xx'}$ defines the slope of this ellipse.

3.1 Beam transport in linear approximation

In linear approximation one can assume that there is no coupling between the degrees of freedom and only linear forces are present. The motion of a particle can be described considering only first order linear equations. In this case a simplified linear transport based on transformation matrices can be applied. This so called matrix formalism [47] is valid for highly relativistic particles but nevertheless it is a simple and useful approximation depending only on the focusing properties of the transport system. Furthermore, the tomography reconstruction, described later, relies on the validity of such an approximation defining the transformations between each two observation points.

Let

$$M = \begin{pmatrix} M_{11} & M_{12} \\ M_{21} & M_{22} \end{pmatrix} \tag{3.3}$$

be the transport matrix from point z_0 to z_1 along the beamline - Fig. 3.3, so that $det(M)$ is unity and

$$|Tr(M)| = |M_{11} + M_{22}| < 2. \tag{3.4}$$

The requirement on the determinant states that an object undergoing a transformation
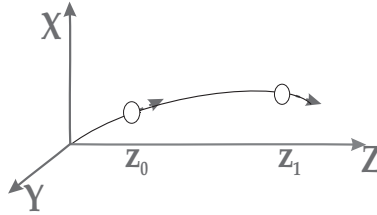
Figure 3.3: A particle can be transported between two longitudinal positions z_0 and z_1 knowing the transport matrix of the elements constituting the beamline. Here the horizontal and the vertical axes are rotated with respect to Fig. 3.1 in order to emphasize on the horizontal that will be used later in the formulae.

defined by such a matrix preserves its area. The requirement on the trace of the matrix states that the motion of the particles under M is stable, i.e. the trajectories defined by M enclose on themselves in one revolution along the reference path.

A particle can analytically be transported between the two longitudinal positions using

$$\left. \begin{pmatrix} x \\ x' \end{pmatrix} \right|_{z_1} = \begin{pmatrix} M_{11} & M_{12} \\ M_{21} & M_{22} \end{pmatrix} \left. \begin{pmatrix} x \\ x' \end{pmatrix} \right|_{z_0} = M \left. \begin{pmatrix} x \\ x' \end{pmatrix} \right|_{z_0}. \tag{3.5}$$

Given a set of beamline elements having transport matrices $M_0, \cdots, M_n$, it is then easy to find a final trajectory vector $X_f = \left. \begin{pmatrix} x \\ x' \end{pmatrix} \right|_f$ from an initial one X_i as

$$X_f = M_n \cdots M_1 \cdot M_0 \cdot X_i. \tag{3.6}$$

Transport matrices are defined for different beamline elements. For instance, the matrix of a quadrupole magnet with strength k, see Eq. 3.9, and $k > 0$ focusing for a positively charged particle, and effective length l_q is [47, 48]

$$QF = \begin{pmatrix} \cos\left(l_q\sqrt{k}\right) & \frac{\sin\left(l_q\sqrt{k}\right)}{\sqrt{k}} \\ -\sqrt{k}\sin\left(l_q\sqrt{k}\right) & \cos\left(l_q\sqrt{k}\right) \end{pmatrix} \tag{3.7}$$

and that of a defocusing one

$$QD = \begin{pmatrix} \cosh\left(l_q\sqrt{|k|}\right) & \frac{\sinh\left(l_q\sqrt{|k|}\right)}{\sqrt{|k|}} \\ \sqrt{|k|}\sinh\left(l_q\sqrt{|k|}\right) & \cosh\left(l_q\sqrt{|k|}\right) \end{pmatrix}, \tag{3.8}$$

where the focusing strength k of a quadrupole is defined by its gradient

$$k\,[m^{-2}] = \frac{q \cdot g}{p} = \frac{q}{p}\frac{dB_y}{dx}\frac{[\text{T/m}]}{[\text{GeV/c}]} \tag{3.9}$$

for q, p being the corresponding particle's charge and momentum, g is the quadrupole gradient, B - the magnetic field. The notation changes for a negatively charged particle.

If $k = 0$, the matrix is equivalent to the one of a drift space, namely

$$M = \begin{pmatrix} 1 & l_q \\ 0 & 1 \end{pmatrix}. \tag{3.10}$$

If the length of the quadrupole with strength $k_x(z) > 0$ is infinitesimally small - dz, the angular deflection given to an electron after some displacement z is

$$dx' = -xk_x(z)dz. \tag{3.11}$$

Differentiation leads to the basic equation for particle trajectory in linear approximation - the general Hill's equation for an on-momentum particle [47–49]:

$$\frac{d^2x}{dz^2} + k_x(z)x = 0. \tag{3.12}$$

An on-momentum particle is the one which has no momentum deviation with respect to an ideal reference particle. The system of motion equations for the two transverse planes becomes

$$\left| \begin{aligned} \frac{d^2x}{dz^2} + k_x(z)x &= 0 \\ \frac{d^2y}{dz^2} + k_y(z)y &= 0 \end{aligned} \right. \tag{3.13}$$

3.1. Beam transport in linear approximation

as one considers that $sgn(k_y(z)) = -sgn(k_x(z))$, see Appendix A. When $k_{x,y}(z)$ varies along the accelerator in an alternating-gradient manner Eq. (3.13) describes the oscillatory betatron motion resulting from linear focusing with restoring forces. Thus, longitudinally, along the z-coordinate, the particles oscillate in a sinusoidal manner within some range of maximum displacement. The period of the oscillations depends fully on the magnetic lattice of the machine, i.e. on the restoring forces defined by $k_{x,y}(z)$.

Neglecting momentum deviation, the solution of the general Hill's equation, as a second order differential equation, is uniquely defined by the initial values and can be written as [48]

$$\left| \begin{aligned} x(z) &= M_{11}x(z_0) + M_{12}x'(z_0) \\ x'(z) &= M_{21}x(z_0) + M_{22}x'(z_0) \end{aligned} \right. \tag{3.14}$$

or in matrix form

$$\left. \begin{pmatrix} x \\ x' \end{pmatrix} \right|_z = \begin{pmatrix} M_{11} & M_{12} \\ M_{21} & M_{22} \end{pmatrix} \left. \begin{pmatrix} x \\ x' \end{pmatrix} \right|_{z_0} \tag{3.15}$$

which is the analogue to Eq. (3.5). In what follows the transverse plane is treated in general since the horizontal and the vertical planes are interchangeable. Subscripts are avoided.

The above matrices and equations are valid for a particle having design momentum p_0. If this is not the case, the momentum deviation should be taken into account. Let a particle have momentum different from the design value as

$$p = p_0(1 + \delta) \tag{3.16}$$

and some deflection in the horizontal plane is introduced by bending magnets. The radius of curvature is denoted with r. Then the equations of motion have the form [47]

$$\left| \begin{aligned} &\frac{d^2x}{dz^2} + k_x(z)x = \frac{\delta}{r(z)} \\ &\frac{d^2y}{dz^2} + k_y(z)y = 0 \end{aligned} \right. \tag{3.17}$$

From the right part of the first equation it can be seen that momentum is transferred to x. Eq. 3.5 is also modified as follows:

$$\left. \begin{pmatrix} x \\ x' \\ \delta \end{pmatrix} \right|_{z_1} = \begin{pmatrix} M_{11} & M_{12} & D \\ M_{21} & M_{22} & D' \\ 0 & 0 & 1 \end{pmatrix} \left. \begin{pmatrix} x \\ x' \\ \delta \end{pmatrix} \right|_{z_0}. \tag{3.18}$$

The dispersion function $D(z)$ defines the trajectory of such a particle and $D'(z)$ - the slope. They can be derived using the transport matrix of a dipole magnet.

3.2 The Twiss functions

A general solution of Hill's equation Eq. (3.12) can be written as [48, 49]

$$x(z) = A\sqrt{\beta(z)} \cos(\phi(z) + \phi(z_0)), \tag{3.19}$$

describing the trajectory of a particle - an oscillation which amplitude $\sqrt{\beta(z)}$ and phase $\phi(z)$ depend on the initial conditions and longitudinal position. A is an invariant constant and $\beta(z)$ - the *beta* function, defines the maximum displacement which is termed as beam envelope. Such a transverse motion is known as betatron oscillation. The angle φ at which a particle oscillates as it propagates from z_0 to z is the so called phase advance and analytically it can be expressed as [48, 49]

$$\varphi(z) = \phi(z) - \phi(z_0) = \int_{z_0}^{z} \frac{dz}{\beta(z)}. \tag{3.20}$$

For magnetic lattices with strong focusing the phase advance varies fast as the amplitude of the oscillations is small.

Courant and Snyder define two more functions used to describe the betatron oscillations so that [48]

$$\alpha(z) = -\frac{\beta'(z)}{2},$$

$$\gamma(z) = \frac{1 + \alpha^2(z)}{\beta(z)}. \tag{3.21}$$

where α is the maximum angular excursion of a particle and γ defines the span in divergence. Those $\beta(z)$, $\alpha(z)$ and $\gamma(z)$ are referred to as Courant-Snyder or Twiss parameters. Using them the transport matrix 3.3 becomes [48]

$$M(z_1, z_0) = \begin{pmatrix} \sqrt{\dfrac{\beta_1}{\beta_0}} \left(\cos\varphi + \alpha_0 \sin\varphi\right) & \sqrt{\beta_0 \beta_1} \sin\varphi \\ \dfrac{\alpha_0 - \alpha_1}{\sqrt{\beta_0 \beta_1}} \cos\varphi - \dfrac{1 + \alpha_0 \alpha_1}{\sqrt{\beta_0 \beta_1}} \sin\varphi & \sqrt{\dfrac{\beta_0}{\beta_1}} \left(\cos\varphi - \alpha_1 \sin\varphi\right) \end{pmatrix} \tag{3.22}$$

- a transformation convenient to be applied when the initial and final Twiss parameters are known and one is interested in the real beam transport.

3.2.1 Twiss functions in a periodic FODO structure

As a quadrupole lens is always focusing for one of the transverse planes while at the same time it is defocusing for the other - Appendix A, an arrangement of such magnets with alternating polarity and certain space between them can be used to obtain periodic particles' trajectories. The space in between can be a field-free space, as usual in linear machines, or a

bending dipole magnet surrounded by drifts. Such a symmetric structure is called a FODO cell. The acronym FODO stays for a Focusing-space-Defocusing-space arrangement of the beamline elements. The field gradients of the quadrupoles are carefully chosen with respect to the beam parameters and the length of the space between the magnets. The upper part of Fig. 3.4 shows a structure of a half-length horizontally focusing magnet, a defocusing and again a half-length focusing one as the length of the drift space between each two is equal for a FODO cell. The plot below is the periodic solution of the envelope obtained after choosing the proper gradients. As it can be seen there, the middle of a quadrupole is a symmetry point
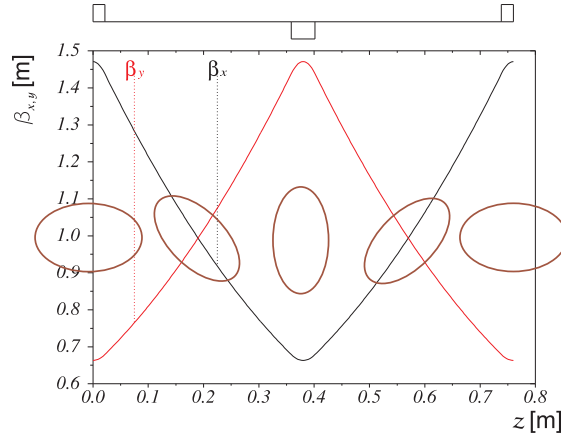

Figure 3.4: Periodic trajectory of the beam envelope and phase-space transformations along a FODO cell. The uppermost part shows the cell arrangement. The horizontal z-axis is labeled with respect to the entrance of the cell. Superimposed are the transformed phase-space ellipses - in the middle of a quadrupole the beam is at waist and half-cell length after a magnet the orientation is changed by 90°, i.e. if the beam has been converging it becomes diverging.

where, depending on the polarity of the magnet, the beam envelope can be at a waist, that is the spot size is minimized. In the half-cell length between two adjacent quadrupole lenses the beam ellipse rotates by 90°. If L is the length of such a cell then, to achieve the above mentioned periodicity at least twice, it is needed that the focusing strength $k(z) = k(z+L)$.

3.3   Beam emittance

In the two-dimensional phase space the average particle ensemble can be represented by a phase-space ellipse - Fig. 3.2. In the six-dimensional phase space, the particle density can be described by a hyperellipsoid, whose volume is defined as beam emittance. An analytical representation can be given by the second central moments of the distribution for each degree of freedom and by the coupling term for any two of them. Its volume is interpreted as the spread of the particles around some mean position in the phase space.

In terms of rms values the volume of the ellipsoid - the six-dimensional rms beam emittance, is defined as

$$\varepsilon_{rms}^{6D} = \sqrt[6]{\det\left(\Sigma^{6D}\right)}, \tag{3.23}$$

where Σ^{6D} is the covariance matrix

$$\Sigma^{6D} = \begin{pmatrix} \sigma_x^2 & \sigma_{xx'} & \sigma_{xy} & \sigma_{xy'} & \sigma_{xz} & \sigma_{xz'} \\ \sigma_{x'x} & \sigma_{x'}^2 & \sigma_{x'y} & \sigma_{x'y'} & \sigma_{x'z} & \sigma_{x'z'} \\ \sigma_{yx} & \sigma_{yx'} & \sigma_y^2 & \sigma_{yy'} & \sigma_{yz} & \sigma_{yz'} \\ \sigma_{y'x} & \sigma_{y'x'} & \sigma_{y'y} & \sigma_{y'}^2 & \sigma_{y'z} & \sigma_{y'z'} \\ \sigma_{zx} & \sigma_{zx'} & \sigma_{zy} & \sigma_{zy'} & \sigma_z^2 & \sigma_{zz'} \\ \sigma_{z'x} & \sigma_{z'x'} & \sigma_{z'y} & \sigma_{z'y} & \sigma_{z'z} & \sigma_{z'}^2 \end{pmatrix}. \tag{3.24}$$

If the number of particles remains constant with the evolution of the beam and one can exclude interactions between the particles [50], the phase-space volume occupied by the particle density is an invariant of the motion - the six-dimensional emittance does not change. This statement is referred to as the Liouville's theorem [49]. In general the shape of the hyperellipsoid enclosing this volume will change as the beam propagates.

If there is no coupling between the planes (x, x'), (y, y') and (z, z') - that is all the elements besides the ones in the three 2×2 minors around the main diagonal are zeros (the ones enclosed in dashed lines in Eq. (3.24)), rms emittance can be defined for any of the three trace spaces. The determinant of a 2×2 minor around the main diagonal defines the area occupied by the particles in a particular plane. For the horizontal transverse plane the beam sigma matrix

$$\Sigma_x = \begin{pmatrix} \sigma_x^2 & \sigma_{xx'} \\ \sigma_{xx'} & \sigma_{x'}^2 \end{pmatrix} = \begin{pmatrix} \langle x^2 \rangle & \langle xx' \rangle \\ \langle xx' \rangle & \langle x'^2 \rangle \end{pmatrix} \tag{3.25}$$

defines an ellipse, referred to as the rms ellipse. Its area is the emittance [25]

$$\varepsilon_{x,rms} = \sqrt{\langle x^2 \rangle \langle x'^2 \rangle - \langle xx' \rangle^2}. \tag{3.26}$$

Eq. (3.26) defines the rms[1] emittance, called also projected and geometric, in units of $[m\cdot rad]$. In practice $[mm\cdot mrad]$ is more often used. As this quantity represents the area of an ellipse a factor π, usually avoided, needs to be added.

In order to decouple the beam emittance from its momentum and be able to compare emittances of beams with different momenta, it is convenient to introduce the normalized geometric emittance as

$$\varepsilon_{rms,N} = \beta\gamma\varepsilon_{rms} \tag{3.27}$$

where β and γ are the relativistic Lorentz factors.

The general transverse emittance is the geometric mean of the emittances for the two

---

[1]Another definition of the rms emittance, given by Lapostolle [51], uses the concept of an 'equivalent perfect beam' - a beam which has a uniform distribution within an elliptical boundary and the same second moments and intensity. It can be expressed as

$$\varepsilon_{rms} = 4\sqrt{\langle x^2 \rangle \langle x'^2 \rangle - \langle xx' \rangle^2}.$$

This definition is not used here.

separate planes

$$\varepsilon_{xy,N} = \beta\gamma\sqrt{\varepsilon_{x,rms}\varepsilon_{y,rms}}. \tag{3.28}$$

Off-center particles, situated in areas with low charge density, are not representative for the entire distribution. They introduce long tails in the projections used to calculate the rms values and the effective area of the rms ellipse will be overestimated. For that reason it is useful to define emittance out of 90% or 95% of the distribution.

Emittance and Courant-Snyder invariant

Using Eq. (3.19) it can be shown that the maximum excursions of a particle in the horizontal plane are

$$x = A\sqrt{\beta(z)} \ \text{ and } \ x' = \frac{A}{\sqrt{\beta(z)}} \tag{3.29}$$

or in terms of rms values representing the particles' ensemble

$$\sigma_x = A\sqrt{\beta(z)} \ \text{ and } \ \sigma_{x'} = \frac{A}{\sqrt{\beta(z)}}. \tag{3.30}$$

The locus of all possible positions x and angles x' of a particle is an ellipse with area A. Due to the Liouville's theorem a particle enclosed by such an ellipse will stay like that and thus

$$A = \sqrt{\varepsilon}. \tag{3.31}$$

Using an analytical ellipse equation, the area of the phase space in terms of rms values may be defined for each degree of freedom as [48]

$$\sigma_{x'}^2 x^2 - 2\sigma_{xx'}xx' + \sigma_x^2 x'^2 = \varepsilon_x^2 \tag{3.32}$$

which is equivalent to

$$\gamma_x x^2 + 2\alpha_x xx' + \beta_x x'^2 = \varepsilon_x, \tag{3.33}$$

where β_x, α_x and γ_x, defined as

$$\beta_x = \frac{\sigma_x^2}{\varepsilon_x},$$

$$\gamma_x = \frac{\sigma_{x'}^2}{\varepsilon_x}, \tag{3.34}$$

$$\alpha_x = -\frac{\sigma_{xx'}}{\varepsilon_x},$$

are the Twiss parameters of the bunch of particles introduced earlier in Eq. (3.21). Fig. 3.5 shows the relation between the size, slope and area of the rms ellipse called also Courant-Snyder invariant. Using the transport of a particle between two longitudinal positions from
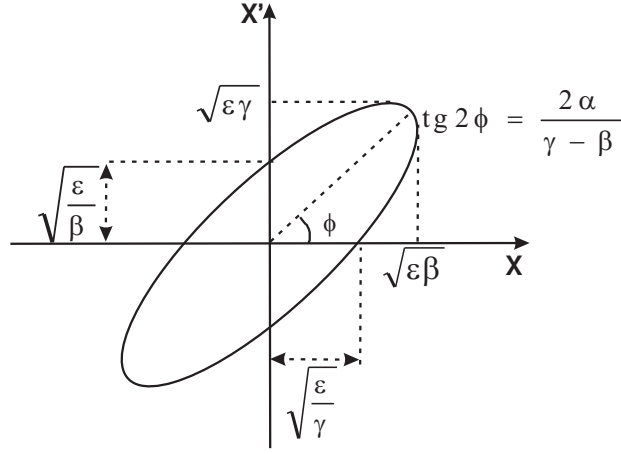
Figure 3.5: RMS ellipse in terms of Twiss parameters.

Eq. (3.5), a handy way to transport the ellipse parameters is given by [47]

$$
\left. \begin{pmatrix} \beta \\ \alpha \\ \gamma \end{pmatrix} \right|_{z_1} = \begin{pmatrix} M_{11}^2 & -2M_{11}M_{12} & M_{12}^2 \\ -M_{11}M_{21} & (M_{22}M_{11} + M_{12}M_{21}) & -M_{12}M_{22} \\ M_{21}^2 & -2M_{21}M_{22} & M_{22}^2 \end{pmatrix} \left. \begin{pmatrix} \beta \\ \alpha \\ \gamma \end{pmatrix} \right|_{z_0} . \tag{3.35}
$$

3.4   Beam mismatch

Let $(\beta, \alpha)_d$ describe the design rms ellipse having a certain area at some longitudinal position of the lattice imposed by machine considerations. If a beam at this position has a distribution in the same transverse plane described by $(\beta, \alpha)_b$ and

$$
(\beta, \alpha)_d = (\beta, \alpha)_b, \tag{3.36}
$$

the beam is called matched [52]. If this is not the case, the beam and the design rms ellipses would not coincide and the real envelope would have some oscillations around the design functions β and α. Those oscillations, termed as beats or β-beating, have twice the betatron frequency and their amplitude is a function of the mismatched ellipse parameters. Measures of the beating and the mismatched ellipse are described in Section 5.

3.5   Space-charge dynamics

During extraction and transport the beam is guided using electromagnetic fields but it con-stitutes of particles of the same polarity, packed in a small volume, and itself is a source of electromagnetic fields. The non-linear part of the direct space-charge fields provoke phenom-ena like increased energy spread, shifts of the betatron frequency and emittance degradation.

The second term in Eq. (3.12) would be sufficient if the phase-space dynamics is defined linearly by external focusing only. Due to the repulsive Coulomb forces an additional term

has to be added. Then Eq. (3.12) transforms into

$$\frac{d^2x}{dz^2} + k_x(z)x - F_x(z)x = 0. \tag{3.37}$$

Coming from the Lorentz force, the electric $\vec{E}$ and magnetic $\vec{B}$ fields exert a force $\vec{F}$ on a particle travelling with velocity v:

$$\vec{F} = q\left(\vec{E} + \vec{v} \times \vec{B}\right). \tag{3.38}$$

With respect to a cylindrical coordinate system the electric force has only a radial component E_r and the magnetic only an angular one B_ϕ. Then it can be shown that the radial component of the space-charge force is proportional to the charge and inversely proportional to the square of the relativistic Lorentz factor [53]:

$$F_r \;=\; q\left(E_r - v_z B_\phi\right) = \cdots = \frac{qE_r}{\gamma^2}. \tag{3.39}$$

Therefore, the space charge will have a defocusing effect for the two transverse planes. Being a linear function of the transverse coordinates - $F_r \propto E_r$, the repulsion nearly cancels at the beam core and increases towards the edges where the strength of the magnetic field is smaller.

Eq. (3.39) shows also that the space-charge defocusing effect can be suppressed by increasing the beam momentum using a strong accelerating field. The contribution of the space charge to the normalized transverse emittance for a laser-driven RF gun can be expressed as [54]

$$\varepsilon_{N,x}^{sc} = \frac{\pi}{4}\frac{1}{\alpha k}\frac{1}{\sin\phi_0}\frac{I_{peak}}{I_0}\mu_x\left(A\right) \tag{3.40}$$

where $\mu_x\left(A\right)$ is a dimensionless space-charge factor representing the density distribution and the bunch aspect ratio $A = \frac{\sigma_x}{\sigma_z}$:

$$\mu_x\left(A\right) = \sqrt{\langle \xi_x^2 \rangle \langle x^2 \rangle - \langle \xi_x x \rangle^2}.$$

$\alpha = \frac{qE_0}{2mc^2k}$ is a dimensionless RF strength parameter for k being the period of the RF wave and E_0 - the peak accelerating field, I_0 is the characteristic Alfven current and I_{peak} - the peak current of the electron bunch. ξ_x represents the horizontal component of the space-charge field. Selecting ϕ_0 - the launching phase of the laser with respect to the phase of the RF wave, close to $^\pi/_2$ would diminish the space-charge emittance growth.

A mechanism to counteract the correlated linear space charge comprises of realignment of different longitudinal slices. The radial space-charge force on a slice is defined by the position of the slice within the bunch and by the longitudinal charge density profile. The space-charge force is stronger in the central part of the bunch than in the head and the tail. Consequently different slices have distinct orientation angles in the phase space and

the projected emittance would accumulate various contributions. Using a solenoid lens, the angles with which different longitudinal slices rotate are matched to a common one at some z–position depending on the solenoid field [55]. In this manner only the representation of the projected phase-space is changed rather than the full phase-space volume. The application of this linear space-charge compensation technique in PITZ is given in [38, 41].

Sacherer [56] has derived the relation between the space-charge force, i.e. the generalized beam perveance $K = \frac{2I_{peak}}{I_0(\beta\gamma)^3}$ with β and γ being the Lorentz factors, and transverse envelopes X and Y as

$$\overline{F_x x} = \frac{K}{2} \frac{X}{X + Y}. \tag{3.41}$$

$\overline{F_x x}$ depends linearly on the rms envelope parameters. Taking into account the last, one can write an rms envelope equation for a bunched beam with elliptical symmetry for each plane as [56, 57]

$$X'' + k_x X - \frac{\varepsilon_x^2}{X^3} - \frac{K}{2(X + Y)} = 0. \tag{3.42}$$

The equations for the two transverse planes are coupled by the term represented in Eq. (3.41). The ratio between the space-charge and the emittance term in Eq. (3.42), known as laminarity parameter, can be used to determine which effects are dominant in the beam envelope evolution. If with Λ_x is denoted

$$\Lambda_x = \frac{K}{2\varepsilon_x^2} \frac{X^3}{X + Y} \tag{3.43}$$

and $\Lambda_x < 1$, the beam is emittance dominated while otherwise the determination of the beam radius is governed by a space-charge dominated regime. For the expected PITZ parameters, $I_{peak} = 50\,\text{A}$, constant perveance for momentum $p = 32\,\text{MeV/c}$ and normalized geometric emittance $\varepsilon_{xy,N} = 1\,\text{mm·mrad}$, the space-charge term is about one order of magnitude higher than the emittance term in front of the first quadrupole magnet along the beamline ($z \simeq 5\,\text{m}$). If the beam drifts about 5 m downstream, its rms size increases from 0.5 mm to 1 mm. Fig. 3.6 shows the evolution of the space charge over emittance ratio for fixed normalized emittance of $\varepsilon_{xy,N} = 0.97\,\text{mm·mrad}$ and different beam momenta for two predefined rms spot sizes of 0.5 mm and 1 mm. The dashed green lines in the figure show an increase of four times of the space charge for a particular momentum of 25 MeV/c if there is no quadrupole focusing applied before 10 m where the matching section of the PITZ tomography module starts. Thus, the focusing strength of the matching quadrupoles would need to be increased which would cause an increase of the betatron phase advance. Having in mind some constraints on the quadrupole gradients, discussed in chapter 5, and the number of Twiss parameters to be adjusted, a matched solution might not be found.

A drift space of length z_d,

$$z_d = 1.31 \times 10^2 \frac{(\gamma^2 - 1)^{\frac{3}{4}}}{\sqrt{I_{peak}}} r_0 \tag{3.44}$$
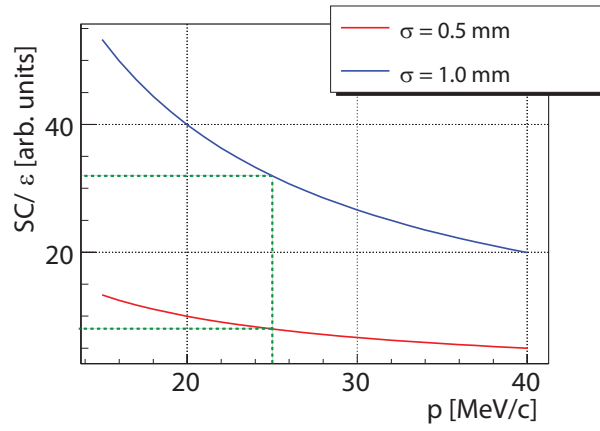
3.5. Space-charge dynamics

Figure 3.6: Decrease of the space charge over emittance ratio for fixed normalized emittance of $\varepsilon_N = 0.97$ mm·mrad versus the range of beam momenta for which the tomography module is designed - [15, 40 MeV/c]. The two different spot sizes are obtained from simulations where $\sigma_{x,y} = 0.5$ mm (red curve) is the spot size at about 5 m from the cathode and $\sigma_{x,y} = 1.0$ mm (blue curve) is the increased spot size at about 10 m downstream the cathode.

with r_0 being the initial beam radius and γ - the reduced energy (Lorentz factor), will lead to doubling of the beam size due to space-charge forces [50]. For the spot sizes used in Fig. 3.6, this reduced-distance concept from Eq. (3.44) states a drift length of about 4.6 m which agrees well with the particularly simulated case for a momentum of p = 32 MeV/c.

As a consequence it is accurate to conclude that smoother matching of the beam to the lattice parameters will be accomplished if the beam is focused earlier. In a matched beam the amplitude of the envelope oscillations is minimized and the space charge force is axially averaged. The decrease of the amplitude of the betatron oscillations is shown in Fig. 3.7 where two different sets of matching quadrupoles have been used for identical beam
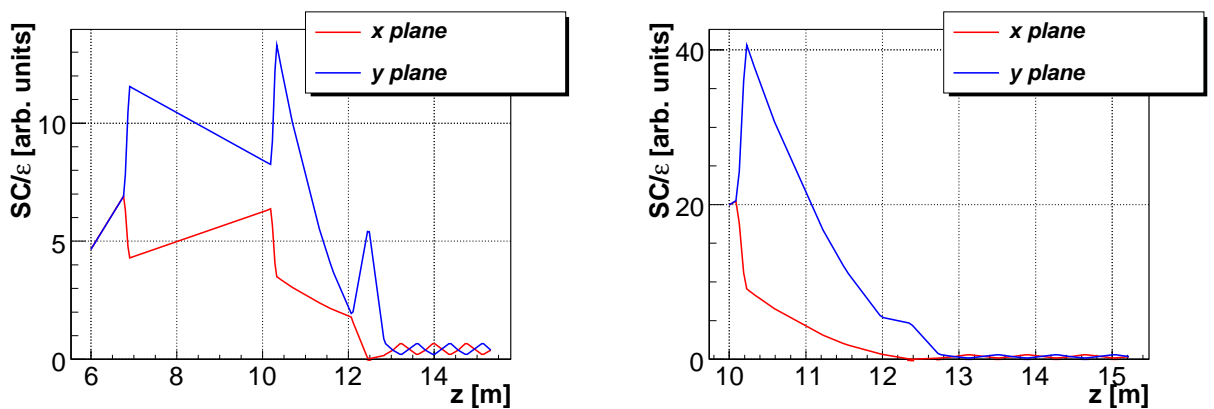
(a) The first matching quadrupole is located ∼6.8 m from the cathode.

(b) The first matching quadrupole is located ∼10.2 m from the cathode.

Figure 3.7: Two different in geometry matching solutions. The periodic behaviour of the space charge-over-emittance ratio along the FODO cells represents minimized amplitute oscillations of the beam envelope.

parameters like momentum, geometric emittance, generalized perveance. Fig. 3.7(a) includes two more matching quadrupoles than Fig. 3.7(b). Being located about 3.4 m upstream of

the first magnet in Fig. 3.7(b), they give the possibility to reduce the extend of the betatron oscillations and the velocity with which the particles traverse the phase-space ellipse.

To reach a state of a matched beam, the strengths of the quadrupole magnets have to be corrected according to [56]

$$\Sigma_x \left. \right|_{z_1} = \left(F_x \Sigma_x + \Sigma_x F_x^T \right) \left. \right|_{z_0} , \tag{3.45}$$

with Σ_x being the beam sigma matrix and

$$F_x = \begin{pmatrix} 0 & 1 \\ -k_x + \frac{K}{\sigma_x^2} & 0 \end{pmatrix}.$$

F_x is a function of the linear part of the space-charge as well as the applied external focusing. These relations are valid for a beam with elliptical symmetry in the transverse planes as the emittance does not degrade which is not the case for PITZ.

3.6   Transverse emittance measurement techniques

In general the transverse beam emittance is measured in a particular plane of interest - i.e. separately for both of the transverse planes, to obtain the values of the horizontal and vertical emittances. Each of the techniques mentioned below requires measuring the beam profile directly by means of different screens or wirescanners, and the angular distribution using apertures or reconstruction techniques [58].

The transverse motion of particles from point z_0 to point z_1 can be expressed using linear approximation by matrix formalism as in Eq. (3.5) and so, using rms values and matrix algebra,

$$\Sigma|_{z_1} = M \Sigma|_{z_0} M^T, \tag{3.46}$$

where M^T is the transpose of the matrix M and Σ is the beam sigma matrix. The rms beam size and divergence may be calculated using

$$\sigma_{x,z_1}^2 = M_{11}^2 \sigma_{x,z_0}^2 + 2 M_{11} M_{12} \sigma_{xx',z_0} + M_{12}^2 \sigma_{x',z_0}^2. \tag{3.47}$$

If there are n measurement points, then

$$\begin{pmatrix} \sigma_{x,z_1}^2 \\ \sigma_{x,z_2}^2 \\ \dots \\ \sigma_{x,z_n}^2 \end{pmatrix} = \begin{pmatrix} (M_{11,z_1})^2 & 2M_{11,z_1}M_{12,z_1} & (M_{12,z_1})^2 \\ (M_{11,z_2})^2 & 2M_{11,z_2}M_{12,z_2} & (M_{12,z_2})^2 \\ \dots \\ (M_{11,z_n})^2 & 2M_{11,z_n}M_{12,z_n} & (M_{12,z_n})^2 \end{pmatrix} \begin{pmatrix} \sigma_{x,z_0}^2 \\ \sigma_{xx',z_0} \\ \sigma_{x',z_0}^2 \end{pmatrix} = M \begin{pmatrix} \sigma_{x,z_0}^2 \\ \sigma_{xx',z_0} \\ \sigma_{x',z_0}^2 \end{pmatrix}$$

$$\tag{3.48}$$

and then the matrix needs to be inverted in order to find the beam size, divergence and

covariance. Provided the matrix M is invertable, for $n = 3$ there is a single solution. For overdetermined systems as $n > 3$, the solution is found in least square sense [58].

3.6.1   Quadrupole scan method

This method includes the usage of one or more quadrupole lenses and an observation screen downstream. The matrix M in Eq. (3.48) is quantified by the quadrupole's strength and length and drift spaces. By varying the field gradient of the magnet, the position of the beam waist is changed with respect to the screen. When the beam size is measured under different focusing conditions different projections of the phase-space ellipse will be seen at the position of observation and in general a full π rotation of the transverse phase space can be achieved. The minimum and maximum gradients can be defined by limitations of the quadrupole itself or by the beam size.

As a function of the focusing strength k_x, the beam size σ_x^2 is fitted with a parabola [58]. A parabolic parametrisation of the fit is

$$\sigma_x^2 = a(k_x - b)^2 + c = ak_x^2 - 2abk_x + (c + ab^2). \tag{3.49}$$

The elements of the transport matrix for the quadrupole scan are functions of the quadrupole strength or, using equation (3.47),

$$\sigma_{x,z_1}^2 = M_{11}^2(k)\sigma_{x,z_0}^2 + 2M_{11}(k)M_{12}(k)\sigma_{xx',z_0} + M_{12}^2(k)\sigma_{x',z_0}^2 \tag{3.50}$$

and thus the a, b, c parameters of Eq. (3.49) and the known M_{ij} can be used to determine $\sigma_x^2, \sigma_{xx'}$ and $\sigma_{x'}^2$. Using the relations between the Twiss parameters, beam size, divergence, covariance and emittance, the Twiss parameters can also be calculated from the fit parameters as

$$\beta = \sqrt{\frac{a}{c}},$$

$$\alpha = \sqrt{\frac{a}{c}}\left(b + \frac{M_{11}}{M_{12}}\right) \text{ and} \tag{3.51}$$

$$\gamma = \frac{M_{12}^2}{\sqrt{ac}}\left[(ab^2 + c) + 2ab\frac{M_{11}}{M_{12}} + a\left(\frac{M_{11}}{M_{12}}\right)^2\right].$$

Since the quadrupole scan technique depicted above uses pure matrix formalism - i.e. nonlinearities in the transformation of the phase space are excluded, it does not take into account the last two terms in Eq. (3.42) and consequently the analysis lacks the effects introduced by space-charge forces. Symmetry around the waist in the spot size versus quadrupole strength does not hold if there are different focusing forces acting on different parts of the beam ellipse and a parabolic fit is problematic [59]. In order to include linear space charge one might consider using a method similar to Eq. (3.45) if the conditions for symmetry and

constant emittance hold.

3.6.2 Multiscreen technique

This method is used when the M matrix in Eq. (3.48) is represented by drift spaces. A variation of this method involves the usage of FODO cells. The technique is not adequate in cases when space-charge forces are involved in the beam transport for the same reason as above. A preceeding matching might be needed in the case FODO cells are used. Thus, the beam size might be decreased significantly in both transverse planes so that according to Eq. (3.43) the beam envelope oscillations are governed by emittance-dominated behaviour. As an example consider an artificially generated elliptical distribution without non-linearities also in the longitudinal plane, and PITZ target parameters - normalized emittance $\varepsilon_{xy,N} = 1$ mm·mrad, beam momentum p $= 32$ MeV/c, $I_{peak} = 50$ A and rms sizes of 0.125 mm at the location of the first observation position. The space charge-over-emittance ratio is calculated as 0.4 and the beam is undergoing emittance-dominated regime. The normalized geometric emittance calculated in this way agrees within 1% with the value from numerical particle tracking.

Both of the techniques described above exceedingly rely on the assumption of linear transport and therefore are better suitable for high-energy machines. A method suitable for photo-injector energy ranges is the slit scan.

3.6.3 Slit-scan technique

This technique is applicable for high-current low-energy beams which are space-charge dominated. A transverse slice of the space-charge dominated beam is cut so that the resulting beamlet is emittance dominated. The beamlet is analyzed by a screen downstream of the slit. The beamlet spatial profile at the position of observation is a direct measure of the angular distribution of the beam at the position of the slit. If the slit and the observation position are separated by a drift of length L, the local divergence at the position of the slit is

$$\sigma_{x',i} = \frac{\sigma_{x,i}}{L}, \tag{3.52}$$

where $\sigma_{x,i}$ is the i$^{\text{th}}$ beamlet rms size across the transverse spot distribution. Weighing each measurement of the divergence according to the beamlet intensity and averaging over the number of measurements provides the sheared divergence of the full beam. By mapping the beamlet projection onto its position across the beam, the correlated divergence and the covariance can be calculated [41]. Phase-space portraits revealing the charge density in different parts of the phase space can be reconstructed as well.

The horizontal emittance is obtained when scanning the beam with a vertical slit and vice versa. The resolution of the method depends on the sampling of the initial beam, i.e. the number of divergence measurements, slit opening and choice of the drift length L. Problems for this procedure are the small signal-to-noise ratio of edge beamlets and that a detailed

measurement of the phase space requires many subsequent scans for both transverse spatial coordinates.

3.6.4   Tomographic phase-space reconstruction

Combining the first two methods described above with techniques used in image reconstruction gives the possibility to reconstruct the phase-space density distribution and, consequently, to calculate the projected emittance. The phase space is reconstructed from a number of one-dimensional projections of the beam. The minimum number of projections when using FODO cells to rotate the beam in the phase space is dictated by the minimum number of spot-size measurements needed in order to define a matched periodic solution. Each projection represents a different viewing angle of the phase-space ellipse. The usage of the method is limited to emittance-dominated beams since it relies on a valid linear transport when mapping the projections to the position of reconstruction. Therefore it is necessary to bring the beam to an emittance-dominated regime beforehand or carefully adjust the focusing properties of the lattice as this is to be done in PITZ. Detailed description of the procedure is given in Chapter 5.

The emittance, measured by the afore mentioned methods, is time averaged, because the total emittance is determined from a number of beam pulses. Combining tomographic reconstruction and kicker magnets gives the possibility to measure pulse-by-pulse beam properties.

Conclusions

An introduction to the PITZ facility and the beam properties that are being characterized was given in chapter 2. How these properties are defined was shown in this chapter 3, including:

1. concepts like transverse emittance, Twiss parameters, space-charge dynamics, periodic focusing, etc., needed to be understood in order to be able to perform tomography;

2. space-charge dynamics, combined with beam focusing, was exemplified with realistic for PITZ situations; in this manner it was shown that the designed tomography module will benefit if the electron beam starts to be focused closer to the booster exit;

3. the tomographic reconstruction will be used as a method for transverse phase-space measurements and in private for emittance measurements, therefore other techniques with the same application were described; positive and negative aspects of the quadrupole scan, the multiscreen technique and the slit scan were discussed;

4. the tomographic phase-space reconstruction was introduced briefly as the last measurement method; this method will give the possibility to measure the phase-space density distributions of the two transverse planes simultaneously with improved signal-to-noise

ratio for short pulse trains; the last three advantages give the possibility to measure selected single pulses from the pulse train, provided that deflecting kicker magnets are installed.

Chapter 4

Mathematical background of tomographic reconstruction

Tomography deals with the reconstruction of a multidimensional function from a number of its projections calculated or measured at different observation angles. The solution of the problem was originally given in 1917 by Johann Radon [60] but it was not practically recognized until Hounsfield and Cormack, independent from each other, invented the X-ray scanner and some of the algorithms needed. The constructive proof of Hounsfield and Cormack was rewarded with a Nobel prize in 1979 [61, 62]. A great number of scientific and practical areas are using the ideas behind tomography - medical diagnosis is interested in cross sections of the human body, oceanographers are able to reveal 3D flow patterns, archaeology needs non-destructive material inspection. The fundamentals of the theory involved are the mathematical procedures of tomographic reconstruction. This chapter introduces some basics of tomography.

In what follows, the figures showing reconstruction results are obtained with codes, explicitly adapted or developed by the author of this thesis for PITZ experimental and simulation data. Each algorithm is realized in C++ and the visualization, as well as some of the calculations, are based on the ROOT [63] framework. Initially the MENT algorithm described in Section 4.5 was realized by J. Scheins [64] and now has been modified with procedures more convenient for PITZ.

4.1 The Radon Transform

Let the two-dimensional density function ρ be defined in (x, y) and (x_θ, y_θ) represents a rotation with an angle θ - Fig 4.1. A point in the plane defined by the pair (x_θ, y_θ) has coordinates according to the rotation rule

$$\begin{pmatrix} x_\theta \\ y_\theta \end{pmatrix} = \begin{pmatrix} \cos\theta & \sin\theta \\ -\sin\theta & \cos\theta \end{pmatrix} \begin{pmatrix} x \\ y \end{pmatrix}. \tag{4.1}$$
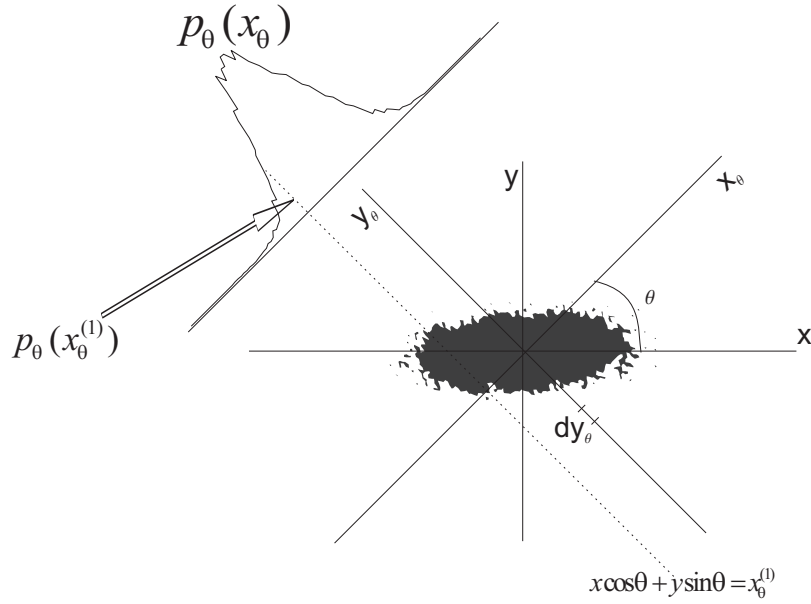
Figure 4.1: A density function ρ and its projection p_θ - Radon transform, at an angle θ.

Integration over a path orthogonal to the projection plane defines a line integral $p_\theta(x_\theta)$

$$p_\theta(x_\theta) = \int_{x_\theta} \rho(x, y) dy_\theta. \tag{4.2}$$

Using a Dirac delta function to show the path of the line integral and integrating over different paths $x_\theta^{(i)}$ Eq. (4.2) can be rewritten as

$$p_\theta(x_\theta) = \int_{-\infty}^{\infty} \int_{-\infty}^{\infty} \rho(x, y) \delta(x \cos \theta + y \sin \theta - x_\theta) dx dy. \tag{4.3}$$

The right hand side of Eq. (4.3) is known as the Radon transform $[\mathcal{R}\rho](\theta, x_\theta)$ of the function $\rho(x, y)$ [65]. The Radon transform is an operator, i.e., when acting on a function in the (x, y) space it produces another function in the (θ, x_θ) space. According to the definition given above, a point in the (θ, x_θ) space corresponds to a line $x_\theta^{(i)}$ in the (x, y) space as far as $x_\theta^{(i)}$ is defined.

Let $p_{\theta_i}(x_{\theta_i})$, $i = 0, \ldots, (N-1)$, be N projections for θ_i in $[0, \pi]$. A simplified statement of the problem of reconstruction would be: if given the functions $p_{\theta_i}(x_{\theta_i})$ find an estimate $\widehat{\rho}$ of the function ρ. The solution is given as [60]

$$\widehat{\rho}(x, y) = \frac{1}{2\pi^2} \int_0^\pi \int_{-\infty}^{\infty} \frac{\frac{\partial p_\theta}{\partial x_\theta}}{x \cos \theta + y \sin \theta - x_\theta} dx_\theta d\theta. \tag{4.4}$$

The last assumes that there is an infinite number of projections. Provided this assumption does not hold, i.e., there is a finite number of $p_{\theta_i}(x_{\theta_i})$, one needs to find a discrete approximation of $\widehat{\rho}$.

In the following some fundamental methods for inversion of the Radon transform are given. The Fourier Slice Theorem [61], discussed first, determines the classification of the convolution or Fourier methods. Another class of reconstruction algorithms uses the Back-projection method [61] wherefrom they are grouped as iterative backprojection techniques.

4.2 The Fourier Slice Theorem

An approach to find an inversion of the Radon transform is using the Fourier Slice Theorem, also called Projection Slice Theorem [66] or Central Section Theorem [67]. The Fourier Slice Theorem states that the one-dimensional Fourier transform of a projection of a two-dimensional function is equal to a slice of the two-dimensional Fourier transform of the function at the angle of the projection [61, 68].

The two-dimensional Fourier transform of a function ρ in the Fourier domain (ζ, η) is [61]

$$R\left(\zeta, \eta\right) = \int_{-\infty}^{\infty} \int_{-\infty}^{\infty} \rho\left(x, y\right) e^{-j2\pi(\zeta x + \eta y)} dxdy \tag{4.5}$$

where $j^2 = -1$. Then the inverse transform is

$$\rho\left(x, y\right) = \int_{-\infty}^{\infty} \int_{-\infty}^{\infty} R\left(\zeta, \eta\right) e^{j2\pi(\zeta x + \eta y)} d\zeta d\eta. \tag{4.6}$$

The angular orientation of the reference frame (x, y) is arbitrary, so for the sake of simplicity let's assume $\theta = 0$. Then Eq. (4.3) takes the form

$$p_0(x) = \int_{-\infty}^{\infty} \rho(x, y) dy. \tag{4.7}$$

Applying one-dimensional Fourier transform on both sides of the last leads to

$$
\begin{aligned}
P_0(\zeta) &= \int_{-\infty}^{\infty} p_0(x) e^{-j2\pi\zeta x} dx \\
&= \int_{-\infty}^{\infty} \int_{-\infty}^{\infty} \rho(x, y) e^{-j2\pi\zeta x} dydx
\end{aligned}
\tag{4.8}
$$

The last line of Eq. (4.8) is the two-dimensional Fourier transform as in Eq. (4.5) for $\eta = 0$. So,

$$P_0(\zeta) = R(\zeta, 0) \tag{4.9}$$

or the one-dimensional Fourier transform of a projection is the value of the two-dimensional Fourier transform along a line. The general result for arbitrary angle θ is

$$P_\theta(\zeta) = R(\zeta, \eta). \tag{4.10}$$

A rigorous mathematical proof is given in [65].

The Fourier reconstruction method directly implements the Fourier Slice Theorem in a number of steps: derive the one-dimensional Fourier transform for each projection - each of them is a radial section in the two-dimensional Fourier space. Thus, invert the two-dimensional Fourier transform to obtain $\widehat{\rho}$. If there is finite number of projections which do not span equidistantly over the entire angular range, the number of axial slices in the Fourier space is small. Thus, the distance between adjacent points in a radial grid defined in (ζ, η) increases with the frequency and artifacts are introduced.

4.3 Filtered Backprojection

Fig. 4.1 shows that a point of $\rho(x, y)$ contributes to a single line integral $x_\theta^{(i)}$ in the projection $p_\theta(x_\theta)$. In this way it contributes to projections at different angles. Integration over all the line integrals for the possible projections through this point would represent the relative density at this point. This technique is regarded to as backprojection. Defined like this, an inversion of the Radon transform can be written as

$$\rho(x, y) = \int_0^\pi p_\theta(x_\theta)\, d\theta. \tag{4.11}$$

But a line integral passes at least through two points in the (x, y) space and those points are then added in the final integral and, thus, ρ will be smeared.

Fig. 4.2 shows a comparison between an original phantom constituting of two Gaussian distributions and the reconstruction result with backprojection (BP) using four equidistant angular steps over full π. The off-center ridges at the base of the reconstructed image decrease with the number of projections as shown in Fig. 4.3 where 32 projections are used.

The quality of the reconstruction can be improved with additional filter applied to the projections and the result is then subject to integration. This defines the essence of the Filtered Backprojection (FBP). Analytically this can be written as

$$\rho(x, y) = \int_0^\pi \widehat{p_\theta}(x_\theta)\, d\theta, \tag{4.12}$$

where $\widehat{p_\theta}(x_\theta)$ is the filtered projection

$$\widehat{p_\theta}(x_\theta) = \int_{-\infty}^\infty p_\theta(r)|r|e^{j2\pi rt} dr. \tag{4.13}$$

It is the one-dimensional Fourier transform of the product between a ramp filter $|r|$ and a projection defined in polar coordinates (r, θ). The logical consequence used to obtain the last equation is given in [67–69]. An intermediate step worth mentioning is the use of the Fourier Slice Theorem in order to derive Eq. (4.12) from Eq. (4.6).

4.3. Filtered Backprojection

(a) Original phantom distribution.

(b) Reconstruction result using backprojection of four projections equidistantly spaced over π.
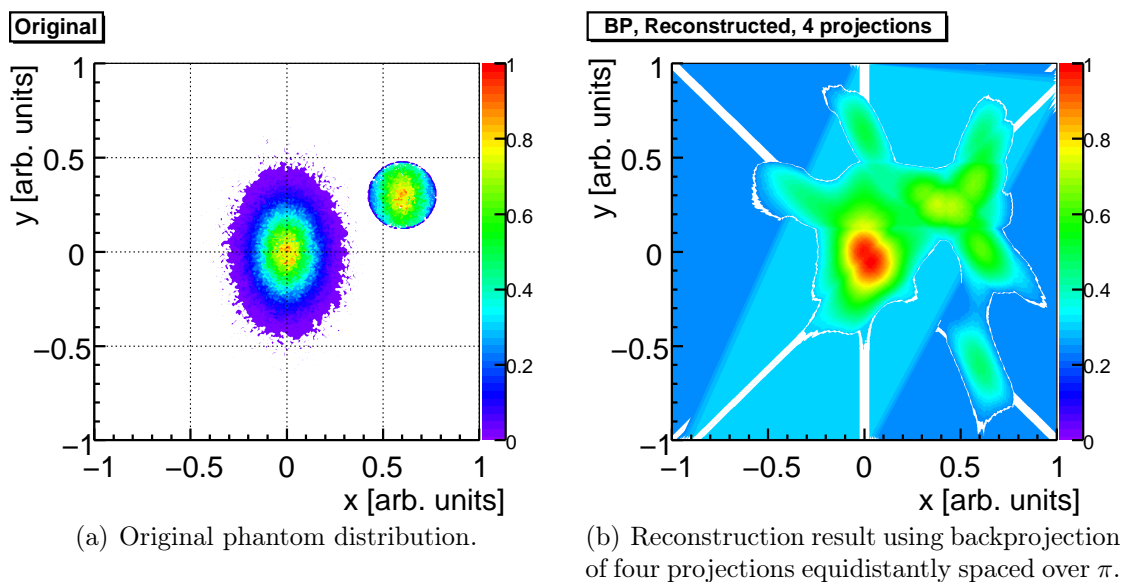
Figure 4.2: Comparison between an original distribution and its reconstructed one using BP. Both distributions are drawn as contour plots. The ridges on the reconstructed distribution decrease with the number of angular steps, see Fig. 4.3.
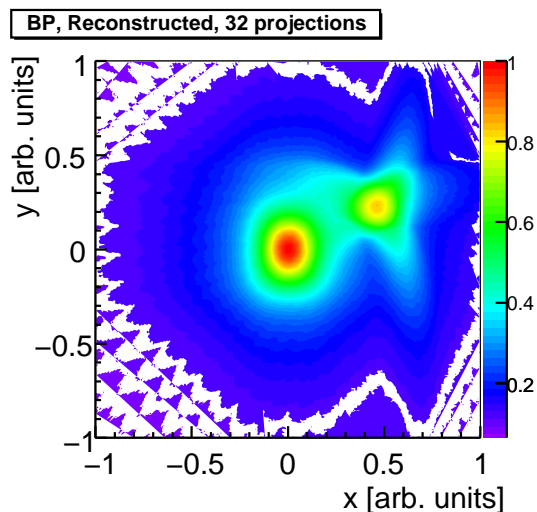

Figure 4.3: Reconstructed distribution drawn as a contour plot using BP of 32 equidistant angular steps. The edge ridges decrease as the number of projections used increases, see Fig. 4.2(b).

As in Eq. 4.13 $|r|$ represents the determinant of the Jacobian of the change from rectangular to polar coordinates, it will introduce negative values in the filtered projections $\widehat{p}_\theta\,(x_\theta)$. They are necessary to correct for projections from other angles. Visually, the filter decreases the excess of positive values at the rims of the object being reconstructed. This might be seen in Fig. 4.4 where the distribution function from Fig. 4.2(a) is reconstructed using filtering prior to the backprojection. In the case of 32 projections the ridges are very slightly smoother with lower amplitude than in Fig. 4.3, while there is hardly a visible difference for the case of four projections. The shape of the central core resembles closer the phantom than the result of BP.

(a) Reconstruction from four equidistant projections.

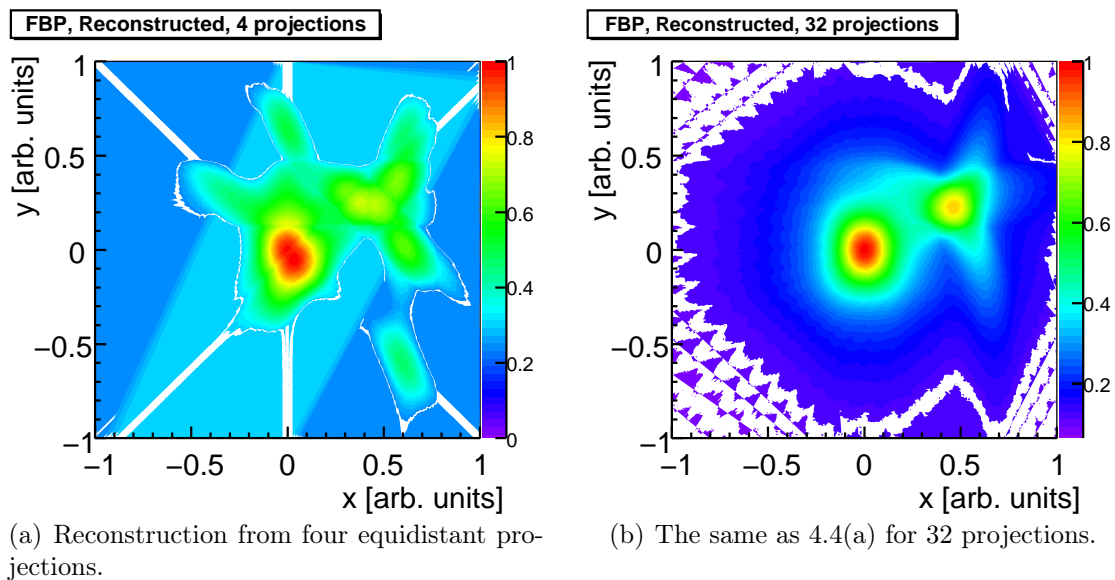(b) The same as 4.4(a) for 32 projections.

Figure 4.4: Comparison between two reconstructions of the Gaussian distribution in Fig. 4.2(a) using four and 32 projections as input to the FBP. Contour plots are used for the graphical representation.

For Fig. 4.4 the following discrete filtering procedure was used [69] as a test:

$$\widehat{p_\theta}(m\tau) = \tau \sum_{n=1}^{N} p_\theta(n\tau)h(m\tau - n\tau), \qquad (4.14)$$

with N being the number of projections, τ is the sampling interval. Each original projection is convoluted with the Ramachandran-Lakshminarayanan filter function h for which [69]

$$h(l\tau) = \begin{cases} \frac{1}{4\tau^2}, & l = 0; \\ 0, & l \, \text{even integer} \\ -\frac{1}{(l\tau\pi)^2}, & l \, \text{odd} \end{cases} . \qquad (4.15)$$

The sampling interval τ is defined with respect to the conditions of the Nyquist-Shannon sampling theorem [61]: $\tau \leq \frac{1}{r_{max}}$. In the depicted case $\tau \leq \frac{w}{2}$ if w is the frequency band.

Filters might be specified in many ways but the common feature is that they approximate the absolute value of the frequency parameter w at low frequencies. Therefore a ramp filter amplifies big spatial frequencies and one might concider using some type of window function. In [70] various filtering window functions are discussed.

From the examples shown it is clear that smearing of the projection data over the space of the wanted distribution, even after filtering, is not an efficient approach for reconstruction with limited number of projection data. Therefore, the backprojection and filtered backprojection methods cannot be applied at PITZ where projections can be snapped for only four rotations of the underlying phase space.

4.4 Algebraic Reconstruction Technique

Inversion of the Radon transform is not necessarily based on a direct analytical approach as described until now. A different class of reconstruction techniques is based on the Algebraic reconstruction technique(ART) which, as the name implies, uses algebraic mechanisms.

The ART has been used by Hounsfield and Cormack in the very first reconstruction of images. Originally the algorithm has been developed as the Kaczmarz method [71]. It uses a formalism where the different projections are treated as a set of linear equations with the values of the function to be reconstructed as unknown variables. The reconstructed function ρ is an image that can be distributed in M pixel values with ρ_m denoting the optical density in the mth pixel. A projection $p(\theta_n, x)$ is defined as

$$p(\theta_n, x) = \sum_{m=1}^{M} w_{nm}\rho_m \tag{4.16}$$

with index n denoting one of the N available projections at an angle θ_n. The weight factors w_{nm} show the contribution of the mth image pixel to the nth projection - Fig. 4.5, meaning it is the fractional area of the mth-cell crossed by the nth projection. Fig. 4.5 also shows how ART incorporates the projection data - here a ray of a projection is used as this is a narrow band across the plane [72], discretized with the dimensions of the detector. In other words, it is the bin of the histogram representing a projection. In this context, a projection might be used as it should be interpreted as a set of rays.
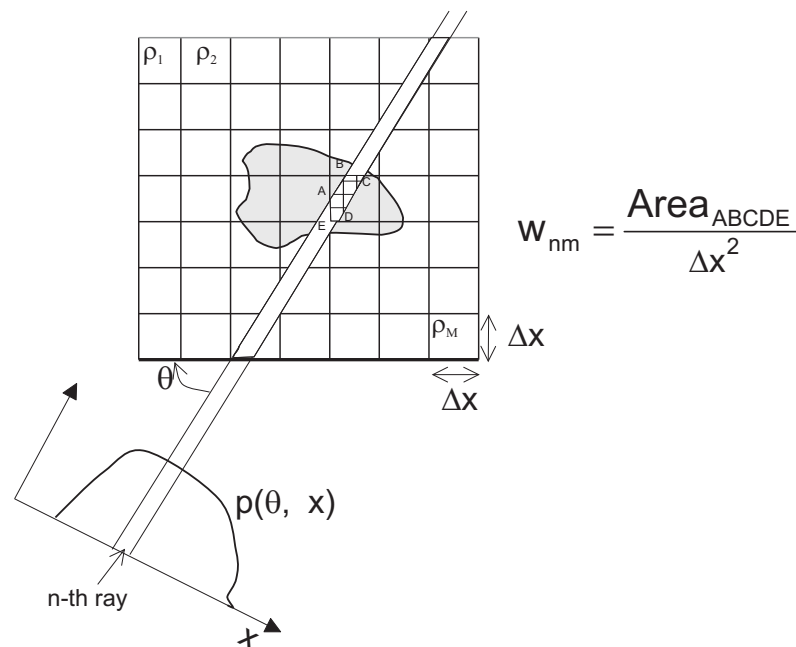

Figure 4.5: In ART the object of the reconstruction is represented as a matrix with M cells. The fraction of the area of the cross-section between the mth pixel and the nth ray of a projection is the weighting factor w_{nm}. Here it is assumed that a pixel has square geometry.

Written as a set of equations the above Eq. (4.16) takes the form

$$
\begin{aligned}
w_{11}\rho_1 + w_{12}\rho_2 + \cdots + w_{1M}\rho_M &= p(\theta_1), \\
w_{21}\rho_1 + w_{22}\rho_2 + \cdots + w_{2M}\rho_M &= p(\theta_2), \\
&\vdots \\
w_{N1}\rho_1 + w_{N2}\rho_2 + \cdots + w_{NM}\rho_M &= p(\theta_N).
\end{aligned}
\tag{4.17}
$$

Not all of the coefficients w_{nm} are non-zero in each equation since not all of the image pixels contribute to a projection. They are calculated only once.

A solution of (4.17) does not exist if the system is underdetermined - that is if the number of projections is less than the number of pixels. If the system is overdetermined - the number of projections is greater than the dimensions of the object, either a multiplicity of solutions exists or none. The algebraic representation of the problem in tomography shows also the significance of having equidistant angular steps - the sparser the matrix to be solved, the greater the uncertainty of finding a unique solution.

ART is an iterative algorithm - ρ is calculated over a sequence of steps as after each step projections from the current guess are snapped. The repetitive procedure continues until the computed projections most closely resemble the given projections according to some set of criteria. The corrections applied to the ρ_m on each successive step might be calculated in a different manner with the aim to cut out fragments from the current guess which are inconsistent with the available data. Let $\rho_m^{(i-1)}$ denotes the mth pixel value obtained in the $(i-1)^{st}$ iteration. In the next iteration a correction $\Delta\rho_m^{(i)}$ for which

$$
\Delta\rho_m^{(i)} = \rho_m^{(i)} - \rho_m^{(i-1)} = \left(\frac{p_i - q_i}{\sum\limits_{j=1}^{M} w_{ij}^2} \right) w_{im}
\tag{4.18}
$$

where $q_i = \vec{\rho}^{(i-1)} \cdot \vec{w}_i = \sum_{j=1}^{M} \rho_j^{(i-1)} w_{ij}$ is the ith ray estimated from the previous guess and p_i is the measured ray-sum along the ith ray [61]. The term $(p_i - q_i)$ is the error in the estimation, which normalized, is applied as a correction term to all the pixels with the appropriate weight. A modification of ART employs the idea that a weight factor is one if the ray-trace from a projection crosses an image cell at its center and zero otherwise [73]. In this case the normalizing sum is equal to the number of cells crossed by the ith ray-trace or $\sum_{j=1}^{M} w_{ij}^2 = W_i$ and the correction needed is $\frac{p_i - q_i}{W_i}$.

In the above, the correction coefficients are added to the image cells and this defines the additive ART. A correction might introduce a negative pixel value which might not make sense depending on the application. Then one applies constrainted ART - negative object estimates are set to zero. Due to the last, an initial guess can be $\rho_m^{(0)} = 0$. An example of constrainted additive ART (caART) is given in Fig. 4.6 where a constraint is non-negative

pixel intensity and the correction coefficients are added to the previous iteration. Comparing Fig. 4.4(a) and Fig. 4.4(b) - Filtered Backprojection with 4 and 32 projections, and Fig. 4.6, one can conclude visually that constrainted additive ART performs better in the case of small number of input projections.
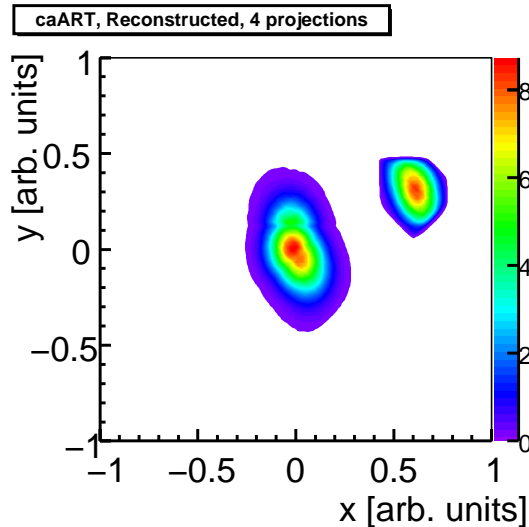

Figure 4.6: Reconstruction of the distribution in Fig. 4.2(a) using four equidistant angular steps in constrainted additive ART. A contour plot is used for the graphical representation.

Another modification is the multiplicative ART [72, 73] - here the pixel value in each successive iteration is defined as

$$\rho_m^{(i+1)} = \rho_m^{(i)} \frac{p_{(i+1)}}{q_{(i+1)}}. \tag{4.19}$$

Multiplicative ART must be started with an initial guess $\rho_m^{(0)} > 0$. Gordon et. al [72] estimate that the multiplicative ART converges to a solution with the largest entropy and is therefore suitable for ill-posed problems such as the case with incomplete projection set. In information theory the entropy is meant as a measure of the uncertainty - with equally likely events to occur there is more choice, i.e. the uncertainty of occurrence of a particular event is bigger. Shannon introduces the entropy as a measure of choice [74] as by definition

$$\mathcal{H}(p_1, \cdots, p_n) = - \sum_{i=1}^{n} p_i \ln(p_i), \tag{4.20}$$

where p_i denotes the probability for outcome i. The next section introduces the concept of entropy in tomographic image reconstruction.

4.5 Maximum Entropy Algorithm

The maximum entropy algorithm (MENT) concept is to choose the solution with the biggest configurational entropy - the one which is most consistent with the measured data and

maximally uncommittal about the unmeasured [75].

Let the function, subject of reconstruction, be defined as in Fig. 4.1 and, for the sake of clarity of the subscripts, (s, t) is the coordinate system after a rotation with an angle θ_i. A ray trace from a projection at an angle θ_i can be written as [76]

$$p_{im} = \int_{s_{im}}^{s_{i(m+1)}} ds \int_{-\infty}^{\infty} dt \rho(s \cos \theta_i - t \sin \theta_i, s \sin \theta_i + t \cos \theta_i) \tag{4.21}$$

for m indicating the number of ray traces, $m = 1, \ldots, M(i)$, i indicates the projection as above, $i = 1, \ldots, N$ for N the available projections. $s_{i1}, \ldots, s_{iM(i)}$ are the set of abscissas for the ith projection. In experimental data $s_{iM(i)}$ defines the bins in the measured projections. Let for an abscissa interval $[s_{im}, s_{i(m+1)})$, defined in the frame of reference of a rotation with an angle θ_i, X_{im} be a characteristic function that

$$X_{im}(s_i) = \begin{cases} 1, & s_{im} \leq s_i < s_{i(m+1)}; \\ 0, & \text{otherwise} \end{cases} . \tag{4.22}$$

Looking back in Fig. 4.1 and substituting the mth interval having width of ds

$$s_{i(m+1)} - s_{im} = ds \left(s \cos \theta_i + t \sin \theta_i \right),$$

it is visible that $X_{im}(s_i)$ extracts a strip from the full parameter space. Introducing the interval characteristic function in Eq. (4.21) allows integration over the entire parameter space of the initial coordinates [64, 76]:

$$p_{im} = \int_{-\infty}^{\infty} dx \int_{-\infty}^{\infty} dy \rho(x, y) X_{im}(x \cos \theta_i + y \sin \theta_i). \tag{4.23}$$

The maximization of the entropy is a constrainted optimization problem of a function of several variables[1]. To maximize the entropy [76–78] use the method of Lagrange multipliers subject to the constraints:

$$\begin{vmatrix} \rho(x, y) \geq 0 \\ \\ \int dx \int_D dy \rho(x, y) = 1 \\ \\ \text{Eq. (4.21)} \end{vmatrix} \tag{4.24}$$

---

[1]The optimization theory uses Lagrange multipliers to find the extremum of a function of several variables $f(x, y)$ which is subject to a constraint $g(x, y) = \text{const}$. For simplicity it is assumed that there are only two variables. In terms of differential geometry the function f defines a hyperplane and at the point of extremum of f its level curve is tangent to the constraint g, i.e. the normal vectors of f and g are co-linear. This is equivalent to the fact that $\nabla f = \lambda \nabla g$ for a scalar λ being the so called Lagrange multiplier. In the particular example f is a two-variable function defined by a single equation. λ introduces one more dimension and two more variables defined with the partial differential equations of the gradient vectors. Thus, instead of solving one equation for two variables with one constraint, the task concludes to solving a system of three equations with three variables.

4.5. Maximum Entropy Algorithm

where D is a compact support of the function $\rho(x, y)$. Due to the first two conditions ρ can be treated as a probability distribution. The requirement of the second equation can be achieved with a proper normalization. As a consequence one requires also that

$$
\left|
\begin{aligned}
&p_{im} \geq 0 \\[1em]
&\sum_{m=1}^{M(i)} p_{im} = 1.
\end{aligned}
\right.
\tag{4.25}
$$

The entropy of ρ is defined as [64, 76]

$$
\mathcal{H}(\rho) = -\int_{-\infty}^{\infty} dx \int_D dy \rho(x, y) \ln(\rho(x, y)).
\tag{4.26}
$$

The task is to find the extremum of Eq. (4.26) subject to constraints Eq. (4.24) or, with the help of Lagrange multipliers Λ_{im}, introduced for each of the Eq. (4.23), it is necessary to find the extremum of a function defined as [76]

$$
\Psi(\rho, \Lambda) = \mathcal{H}(\rho) - \sum_{i=1}^{N} \sum_{m=1}^{M(i)} \Lambda_{im} \left[p_{im} - \int_{s_{im}}^{s_{i(m+1)}} dx \int_D dy \rho(x, y) X_{im}(x \cos \theta_i + y \sin \theta_i) \right].
\tag{4.27}
$$

The derivative of the Lagrangian Eq. (4.27) with respect to $\rho(x, y)$ is [76, 78]

$$
\frac{\partial \Psi}{\partial \rho} = -\ln(\rho(x, y)) - 1 + \sum_{i=1}^{N} \sum_{m=1}^{M(i)} \Lambda_{im} X_{im}(x \cos \theta_i + y \sin \theta_i) = 0
\tag{4.28}
$$

and directly

$$
\rho(x, y) = e^{-1 + \sum_{i=1}^{N} \sum_{m=1}^{M(i)} \Lambda_{im} X_{im}(x \cos \theta_i + y \sin \theta_i)}.
\tag{4.29}
$$

The above equation transforms into [64, 76]

$$
\rho(x, y) = \prod_{i=1}^{N} \sum_{m=1}^{M(i)} H_{im} X_{im}(x \cos \theta_i + y \sin \theta_i),
\tag{4.30}
$$

where $H_{im} = e^{\Lambda_{im} - \frac{1}{N}}$. Incorporating Eq. (4.30) into Eq. (4.23) the task is already to find the coefficients H_{im}. Ref. [64] gives an analytical solution as

$$
H_{im} = \frac{p_{im}}{\int \int dx dy X_{im}(x \cos \theta_i + y \sin \theta_i) \prod_{k \neq i} \sum_{l} H_{kl} X_{kl}(x \cos \theta_k + \sin \theta_k)}.
\tag{4.31}
$$

Each H_{im} is defined by p_{im} and the characteristic functions X_{im} and H_{kl} which are defined for different projections. If p_{im} is zero, correspondingly, H_{im} is set to zero. The dependence

on H_{kl} for $k \neq i$ is suppressed by the sum over many products.

Minerbo [76] uses a nonlinear iterative method to find H_{im}. The initial guess starts with $H_{im}^{(0)} \equiv 1$ for im so that the contribution of the bin p_{im} in the available projection data is not zero. The update on an iterative step $(s+1)$ is

$$H_{im}^{(s+1)} = H_{im}^{(s)} \frac{p_{im}}{p_{im}^{(s)}} \qquad (4.32)$$

as

$$p_{im}^{(s)} = \int_{-\infty}^{\infty} dx \int_{-\infty}^{\infty} dy X_{im} \left(x \cos \theta_i + y \sin \theta_i \right) \cdot$$

$$\prod_{k=1, k \neq i}^{n} \sum_{l=1}^{M(k)} H_{kl}^{(s+\delta(k))} X_{kl} \left(x \cos \theta_k + y \sin \theta_k \right). \quad (4.33)$$

$p_{im}^{(s)}$ is defined by the value of H_{kl} for $i \neq k$ and therefore an iteration has to include all the projections for every ray trace m and fixed i. $(s + \delta(k))$ defines the update order of the coefficients H so that

$$\delta(k) = \begin{cases} 1, k \text{ is already updated} \\ 0, \text{otherwise (this cycle)} \end{cases} . \qquad (4.34)$$

Because the current $H_{im}^{(s)}$ depends on the next $H_{im}^{(s+1)}$, Eq. (4.33) shows that the update procedure is not only iterative over the different m but also recursive.

The MENT algorithm has an elegant geometrical interpretation. The cross-section of strips defined by non-zero characteristic functions $X_{im}(s_i)$ defines a polygon common for all the projections - Fig. 4.7. Each p_{im} is defined by a set of polygons and

$$p_{im} = \sum_{\cup \Delta_{m_1, \cdots, m_n}} A\rho, \text{ A being the corresponding area of the polygon.} \qquad (4.35)$$

The edges of the polygons are defined by the intersection between different bins in the projections and therefore a polygon includes the points where the target function is constant. Integration over those polygons is the area where ρ is defined.

Fig. 4.8 shows the reconstruction result from four equidistant projections for the input distribution used above. Clearly, the result has less artifacts than with Backprojection or Filtered Backprojection and it is comparable with the ART results. The convergence of the algorithm defined as the relative deviation of the reconstructed distribution from the original as a function of the number of iteration steps for different number of input projections and characteristic distributions is shown in [64]. After some iteration steps $\mathcal{O}(10)$ the function becomes monotonous. Here 30 cycles have been used.

This section has introduced some fundamental mathematical logic that will be used further in the reconstruction of the transverse phase space of an electron beam. No analytical means for comparison of results have been used since the differences are believed to be clearly
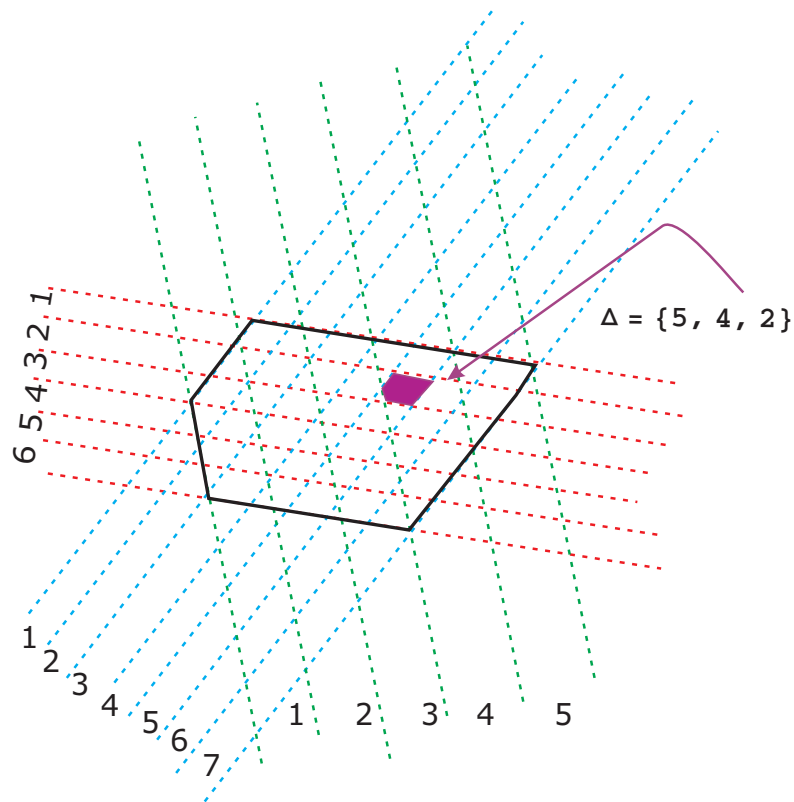
Figure 4.7: The Cross-section of strips defined by non-zero characteristic functions $X_{im}(x \cos \theta_i + y \sin \theta_i)$ for different projections defines the unique polygon $\Delta_{m_1, \cdots, m_n}$.
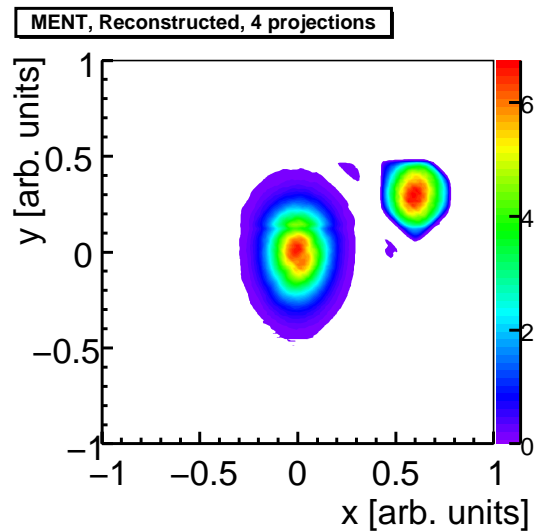

Figure 4.8: Reconstructions with the MENT algorithm over four equidistant projections. Artifacts like the above ridge formation are not present even with the smaller number of rotations. A contour plot representation is used.

visible. Nevertheless, the performance of different algorithms will be compared later when treating simulated electron beam distributions.

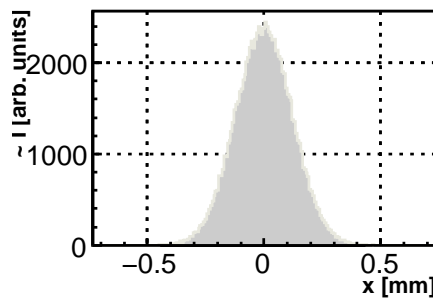## 4.6 Application of Tomographic Reconstruction to the Transverse Beam Dynamics

In the transverse beam dynamics one is interested in the density distribution of the electron bunch at a given position along the beamline. The parameter space needed is $\rho(x, x', y, y')$. Meeting an observation screen, the four-dimensional phase space is projected onto a spatial distribution (x, y) and, thus, a projection of a spatial distribution is identical to a projection of the four-dimensional phase space distribution onto the spatial coordinate. This can be seen in Fig. 4.9.
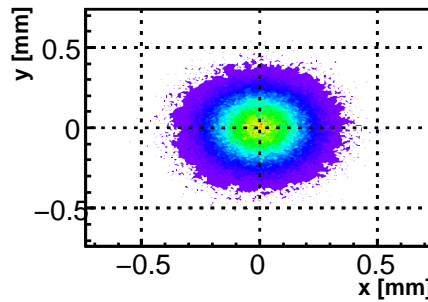
(a) Spatial distribution as seen on an observation screen.
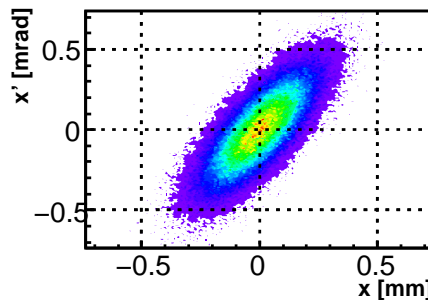
(b) Horizontal phase space distribution

(c) Projection of the spatial distribution onto the horizontal axis.

Figure 4.9: The spatial intensity distribution on a screen is a two-dimensional projection of the phase space. The projection of the intensity on either of the axes is equal to the projection of the phase space on the same axis.

4.6. Application of Tomographic Reconstruction to the Transverse Beam Dynamics

A number of spatial distributions are needed as reconstruction input data and therefore one needs to alter the orientation of the phase space on the screen. Change of the betatron phase advance in front of the observation position is equivalent to rotation of the beam in the phase space. Thus, varying the focusing conditions by means of magnets would produce the needed transformations. Under the assumption of linear transport, the rotation from Eq. (4.1) changes to a transfer matrix M from the position of reconstruction z_i to the position of observation z_f and the needed transformations obey the rule:

$$\left. \begin{pmatrix} x \\ x' \end{pmatrix} \right|_{z_f} = M \left. \begin{pmatrix} x \\ x' \end{pmatrix} \right|_{z_i}. \tag{4.36}$$

Here the horizontal plane of the phase space is treated while the same relations are valid for the vertical.

Projecting a spatial distribution onto the horizontal or vertical axes delivers the wanted intensity distributions as shown in Fig. 4.9. Considering this, a projection of the phase space onto the horizontal axis can be written as

$$p(x_f) = \int \rho(x_f, x'_f) dx'_f \tag{4.37}$$

where ρ denotes the phase-space density distribution. Using the same arguments as in section 4.1 one obtains an expression for a projection at the position of observation as a function of the initial phase-space coordinates

$$p(x_f) = \int \int \rho(x_i, x'_i) \delta(x_f - M_{11} x_i - M_{12} x'_i) dx_i dx'_i. \tag{4.38}$$

The above is the Radon transform of the phase-space distribution under the transformation defined by M.

In the beam dynamics M is not simply a rotation matrix. It introduces also some shearing of the initial distribution. If the rotation of the beam is achieved with quadropole magnets, then M contains some elements representing the focusing of a quadropole lens. The profile of the magnetic field along z of a quadropole presented in chapter 3 has the shape of a square function. This ideal model of the so called hard-edge quadropole assumes constant field along the length of the magnets. This does not hold in reality where the profile has a trapezoidal shape as the field increases from zero outside the quadropole to maximum at its middle assuming the effective length is bigger than the bore radius. Dividing a hard-edge quadropole magnet into smaller ones for which the strength is symmetric around the center, i.e. gradually decreases from the center towards the edges, and integration over them represents the total focusing effect more closely to reality.

If the beam is space-charge dominated one should also care about the additional defocusing strength when adjusting a quadropole. Linear space-charge force can be included in M if the

transport lattice is divided into sections and an additional quadropole magnet is included in some sections [79].

Conclusions

Some remarks on the tomographic reconstruction were described above, including:

1. basic theory on tomography;

2. examples of the performance of BP, FBP, ART and MENT reconstruction algorithms with an artificially generated distribution with specific features were shown; they ruled out that the last two have obvious advantages when the reconstruction is performed on limited data sets; here four projections were used since that much will be available at PITZ;

3. the application of the tomographic reconstruction in the transverse beam dynamics was discussed; how such studies are performed in PITZ is described in detail in the following chapter 5.

Chapter 5

Tomography of the transverse phase space at PITZ

The transverse phase-space distribution of a particle beam can be studied using tomographic techniques and a setup of a number of quadropole magnets and observation screens. In the previous chapter 4 is has been shown how the reconstruction itself works. Evidently, increasing the number of angular steps improves the reliability of the reconstruction. A simplified quadrupole scan setup is needed to be able to study one of the transverse phase spaces. But this is not sufficient if one needs to reconstruct both phase spaces simultaneously. In such a case it is useful to incorporate means of multi-screen measurements and a periodic FODO structure. Such a structure is adopted in PITZ. It consists of four observation screens separated by three FODO cells. Having appropriate gradients, the quadrupole magnets in a FODO cell induce equal in absolute unit changes in the phase advances for the two transverse planes. The phase advance is measured from one screen to the next. This implies also that the Twiss functions are equal on each of the four screens.

At the beginning of this chapter the codes used for numerical simulations of the beam evolution along the beamline are described. Since some of them are well known in the community, details are given only on those which involve postprocessing of the results of them or are explicitly developed. Details on the design and expectations on the performance of the tomography module are discussed afterwards.

5.1 Simulation tools for modeling a transverse phase-space tomography experiment

ASTRA

A Space-charge **TR**acking **A**lgorithm [80] is a suite of programs for generation, tracking and visualization of macroparticle bunches. The tracking routines trace point-like macroparticles through external electric and magnetic fields taking into account the internal repulsive forces

in the bunch. The integration of the equations of motion of a particle in an electro-magnetic field is done via Runge-Kutta algorithm with variable time step. 3D field maps have recently been included - in PITZ for example they are used for simulations of the transverse deflecting structure cavity.

There are two algorithms provided for calculation of the space-charge fields: cylindrical symmetric and 3D [81,82]. The last is needed for instance when the transverse bunch shape is changed using quadrupoles.

MAD

Methodical **A**ccelerator **D**esign [83] is a well known code able to calculate, match and visualize optics parameters from a machine description and a predefined set of input beam parameters. It also incorporates routines for simulations and corrections of machine imperfections. It is completely modular and its interpreter-like interface allows usage of standard programming tools like assignments and loops. The beam transport is modeled via transfer maps.

In the frame of this work only the matching and error-calculation routines are used due to the fact that MAD is not able to take into account the influence of space-charge forces and, thus, it's mainly applicable for high-energy machines. Having in mind the aforementioned and the simplicity and speed of the calculations, MAD is a perfect tool for initial matching and comparison between a theoretical model and resulting ASTRA simulation or real experiment.

TRACE-3D

TRACE-3D [84], like MAD, is able to calculate, match and visualize optics parameters for bunched beams for a given machine description. Unlike MAD, it is designed to be able to calculate also linear space-charge forces and therefore it represents the beam by its six-dimensional sigma matrix. A particle beam is treated via the theory of equivalent beams [56] and emittance degradation cannot be predicted.

The beam transport is also linearized to the use of transfer matrices.

Monte Carlo simulations of emittance measurements

Monte Carlo simulation [85] is a technique used to evaluate the outcome of a process using random inputs. In the case described here, the expected performance of the tomography module has been simulated using a predefined geometry and input beam parameters. The object being seeded is an emittance measurement, thus N seeds are identical to N simulated measurements. For each seed relative deviations in the measured rms spot sizes on the four screens of the PITZ tomography module have been simulated. An error is accepted if it can be resolved experimentally, i.e. if it is greater than the resolution of the optical system. Discussion on the results can be found in the section 5.4 while underlying basic points are

5.1. Simulation tools for modeling a transverse phase-space tomography experiment

given here.

Theoretically it can be shown that the normalized emittance is independent of the uncertainty in the beam momentum measurement [86,87]. This is not the case for the geometrical emittance when it comes to matching of the beam parameters to a lattice structure. A periodic solution of the particles' trajectories is defined by the quadrupole strength using Eq. (3.9) and in fact the gradient is the parameter known explicitly from the hysteresis curve. Thus, a deviation in the strength of a magnet would introduce some mismatch and is related to deviations in the beam size.

Major contribution to the emittance measurement uncertainty comes from off-axis particles, producing long tails in the spatial distribution and, thus, big rms beam sizes. A Gaussian distribution is correctly represented by points situated within 3σ around the mean and it is common to calculate emittance out of particles within 3σ calculated from beam profiles - 90-95 %. The physical representation of such particles in the tails fully depends on the resolution of the optical setup and for PITZ this has been found to be in the range of $(20\text{--}50)$ lp mm^{-1} or down to 10 % for a spot size of 0.1 mm [27].

A basic assumption in the simulations is a good matching of the Twiss parameters to the optics of the lattice. Therefore, the values of the design Twiss parameters are calculated for some predefined normalized geometrical emittance. In any seed the beam spot size on the four screens is measured and a Gaussian error with sigma between 5 % and 33 % is added to each of the four spot sizes for different values of the phase advance between the FODO cells in the range $10°$ to $65°$. Those four perturbed values are the input parameters for the inversion of Eq. (3.48) where the emittance and the Twiss parameters are calculated using linear beam optics and the multi-screen approach at the position of the first screen. The resulting $\beta_{measured}$ function represents the β-beating - denoted as $\Delta\beta(z)$, defined as the mismatch relative to a design periodic solution for particle trajectories as

$$\Delta\beta(z) = \max \left\{ \frac{\beta_{\text{measured}} - \beta_{\text{design}}}{\beta_{\text{design}}} \right\} \Bigg|_{\text{on screen}}. \tag{5.1}$$

This $\Delta\beta$ will be called β-mismatch. The result is used to find the phase advance which delivers the smallest emittance measurement deviation using the four-screen method with respect to the different relative spot size deviations. Knowing this phase advance, the contribution of the spot size errors can be further evaluated to find a statistical confidence interval within which the measurement is representative for a given emittance value. The variance of the β-beating can be found as well.

As a next step the probablity to find no practically consistent, i.e. real, solution of the emittance equation Eq. (3.26) is evaluated as a function of different relative errors in the beam size. As it will be shown, the relative emittance deviation scales with the relative beam size deviation when the later one is below some threshold.

5.2 FODO lattice geometry

Since a quadrupole is focusing for one of the transverse planes and defocusing for the second, a combination of two identical magnets with opposite polarity has to be used to be able to resolve both transverse planes simultaneously. Using multiscreen technique, at least three values of the beam size have to be known for different transport conditions - Eq. (3.48). To provide better accuracy the here described module contains four screens. Assuming a quadrupole effective length of 0.043 m, geometrically the shortest drift space allowed between two adjacent magnets is 0.26 m. The drifts between the quadrupoles in the first two cells, marked with 1st and 2nd in Fig. 5.1(a), and the one between the quadrupoles in an identical cell upstream, used for matching - marked with 0th, have to accommodate kicker magnets for extraction of a single bunch from the bunch train. From the point of view of motion stability - see Eq. (3.4), the quadrupole effective length allows the use of any drift for which the trace of the transport matrix M from screen to screen obeys

$$|\cos \varphi| = \left| \frac{M_{11} + M_{22}}{2} \right| \leq 1, \tag{5.2}$$

where φ is the phase advance, or maximum 0.46 m [88]. Otherwise the particles' trajectories do not close on themselves. Considering the possible length of a kicker magnet, the chosen drift length between two adjacent quadrupoles is 0.337 m.

5.3 Design of the experimental setup

The objective of PITZ as a photo-injector test stand to some extend defines the energies that are reached and the size of the full setup. The overall length of PITZ is about 20 m, compactly packed with a lot of diagnostics components. Therefore the length of the tomography section has to be kept as short as possible.

The physical design of the tomography module has been a joint effort between DESY and ASTeC, STFC Daresbury Laboratory. A number of iterations [88–92] led the way to the final design. Here only the last layout is discussed. The setup cannot be understood as a stand alone but, on the contrary, it requires an additional upstream section used for adjusting the beam Twiss parameters to the optics of the lattice. This upstream part of the beamline is referred to as matching section. A schematics of the two sections is given in Fig. 5.1(a).

5.3. Design of the experimental setup
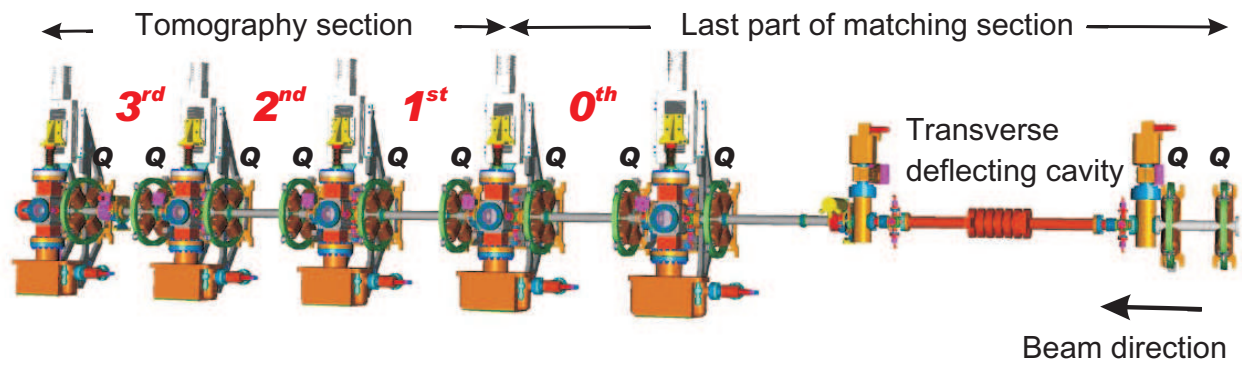
(a) Matching and tomography sections top view. The quadrupole magnets are marked with **Q**.
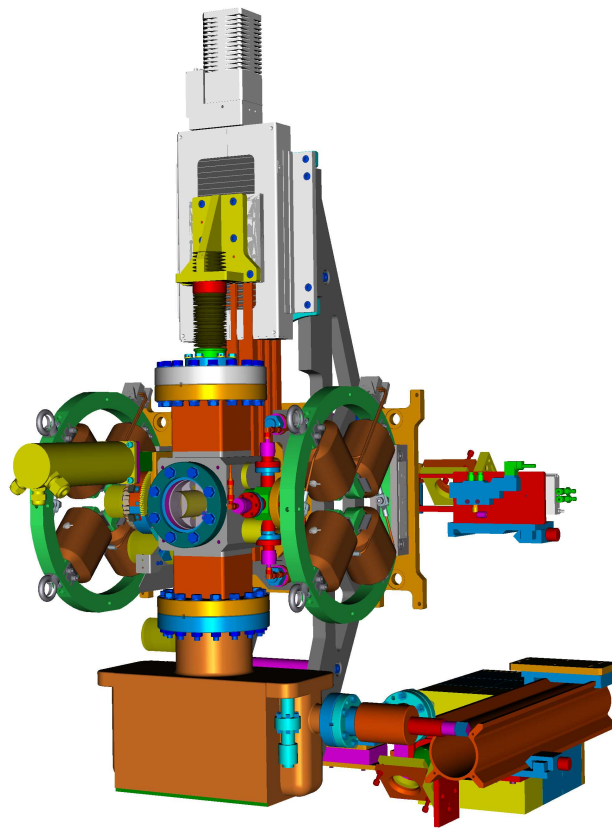
(b) A screen station with the surrounding quadrupole magnets, a BPM in front of it and a steering magnet behind.

Figure 5.1: Matching and tomography section components overview.

The matching section consists mainly of quadrupoles as there are five default ones as shown in Fig. 5.1(a) and two more pairs, not necessarily to be used as doublets, located further upstream at approximately 5 and 6 m from the cathode. Behind the first two quadrupoles in Fig. 5.1(a) there is a long drift that is planned to be occupied later by a transverse deflecting cavity, followed by a quadrupole, a screen station and two more quadrupoles. The rest of the setup is occupied by FODO cells. There are three FODO cells as each is surrounded by two screen stations - in total four observations screens and

59

six quadrupoles. The last two magnets from the matching section, together with the screen in front of them, represent an identical cell - called the 0th cell in Fig. 5.1(a). Except the quadrupoles and the screens, each cell has a beam position monitor (BPM), mounted on the flange right in front of a screen station and a rotatable steering magnet behind it - Fig. 5.1(b).

5.3.1   Quadrupole magnets

The quadrupole magnets in the FODO lattice are used to rotate the beam in the phase space as a sequence of focusing-defocusing lens with respect to the vertical transverse plane is used. A pair of quadrupoles defining a FODO cell is needed in order to obtain a symmetric transformation of both transverse planes. The quadrupoles in the matching section are used to adjust the beam envelope parameters so that periodic particle trajectories with certain phase advance between the FODO cells can be obtained.

All the quadrupoles used for matching and within the FODO cells are identical, produced and measured by DANFYSIK [93]. Acceptance tests have been done on-site. Basic parameters of such a magnet are given in Table 5.1. The measurements include geometry control

Table 5.1: Main parameters of the quadrupole magnets. Effective length and required current are measured at nominal gradient of 5.6 T/m.

Average effective length	0.043	m
Average required current	7.3	A
Physical length	0.063	m
Maximum gradient	7.5	T/m
Bore radius	0.02	m

of aperture and reference points, power tests, hysteresis curve, effective length, correlation between magnetic and geometrical axis and higher harmonic content for n = 3,···, 10. As it can be seen in Fig. 5.2, where the measured field gradient as a function of the applied current is shown, the field stays linear below 7 T/m. For that reason the magnets should be operated with gradients below that value.

The magnetic field measured as a function of the longitudinal position for the nominal gradient of 5.6 T/m is shown in Fig. 5.3. It can be seen that the shape of the field lacks a flat-top region around the center of the magnet due to the fact that the effective length is comparable to the bore radius. Additionally a map with a gradient of 7.5 T/m has been done.

Each quadrupole magnet is powered by a separate power supply delivering accuracy of the field of 10^{-4}.
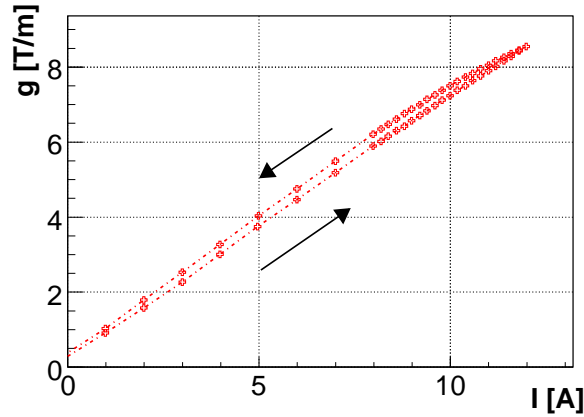
Figure 5.2: Field gradient as a function of the applied current. The data are extracted from the DANFYSIK measurements [94].
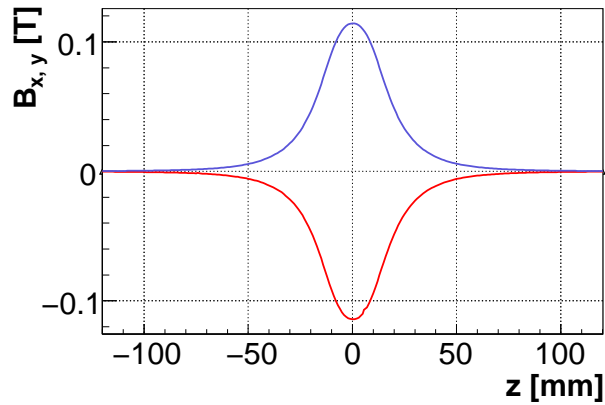

Figure 5.3: Magnetic field mapping as a function of the longitudinal position along the quadrupole for the nominal gradient of 5.6 T/m. The data are taken from quadrupole measurements done by DANFYSIK [94].

5.3.2   Screen stations

A projection of the beam is recorded as the four-dimensional transverse phase space is mapped onto a spatial projection on a screen. Each two cells in the tomography module are separated by a screen station as those around the 1st, 2nd and 3rd cells are the same and the fifth screen station in front of the 0th additional cell has a different design. A screen station consists of a horizontal actuator housing two screens - a YAG and an OTR with a gap between them - Fig. 5.4. The dimensions of the screens are defined with respect to the desired resolution of the transverse deflecting cavity and so is the gap between the screens. This gap is to be used for bunch-by-bunch measurements when only a single bunch is deflected towards a screen by a kicker magnet located one cell upstream and the rest of the train goes straight without a kick. The actuator holding the screens is inserted across the beamline with a linear stage drive thus giving the possibility to precisely position a screen with respect to the applied angular kick.

In the screen stations along the tomography section the OTR mirror meets the beam at an incidence angle of 45° and the YAG is orthogonal to the beam direction as there is a 45° inclined mirror behind it guiding the light out of the vacuum pipe - Fig. 5.4(a).
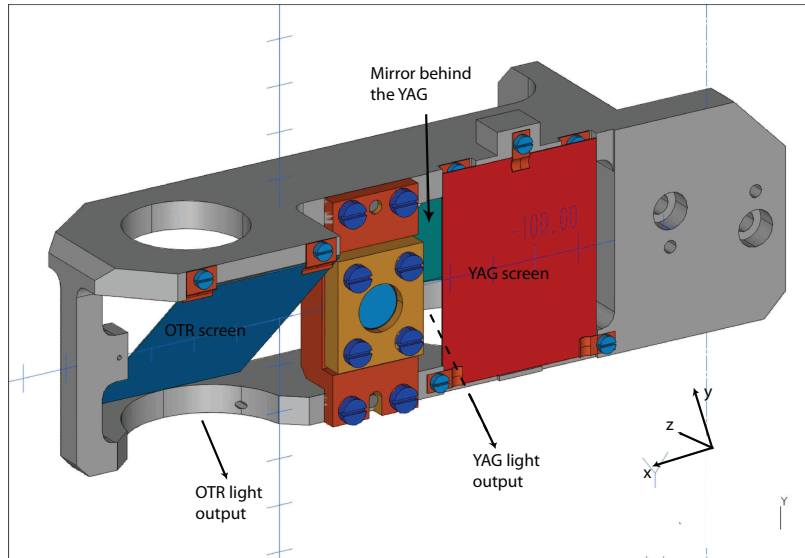
(a) Actuator with mounted 90° YAG and 45° OTR screens along the tomography module. The two screens have the same horizontal axis and an additional movable mirror under the vacuum chamber is used to compensate the different path of the light from the screen to one common CCD camera used for the two screens.
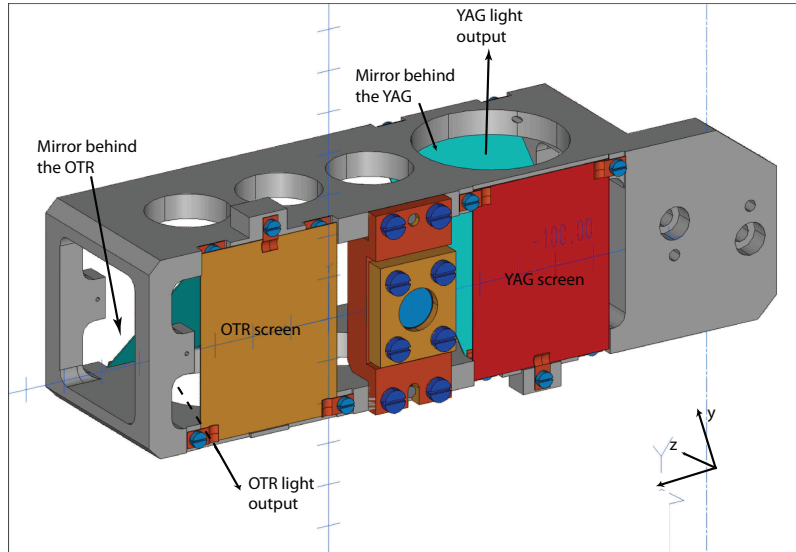
(b) Actuator with mounted 90° YAG and 90° OTR screens in front of the 0th cell from Fig. 5.1(a). There are two physically different optical readout systems used for the two screen types.

Figure 5.4: Two different actuator designs along the tomography and matching sections. Here a ball used for alignment fills the the space between the two screens - it is removed after the installation of the screen stations.

In this figure it is shown that the surfaces of the two screens have the same horizontal axis and consequently the optical path of the outgoing light is different. In order to have common optical readout there is an additional movable mirror outside of the vacuum chamber used

to compensate this difference. The very first screen station in front of the 0th cell has the same YAG geometry but a 90° OTR followed by a 45° mirror - Fig. 5.4(b). The advantage of having an OTR surface orthogonal to the direction of the beam is minimizing depth of focus problems. At the same time the mirror behind it, being a source of OTR too, might lead to interference of two light beams - the forward cone from the 90° surface and the backward from the mirror. This screen configuration is installed for test purposes. Thus, there are two designs of the screen station actuators as shown in Fig. 5.4(a) and 5.4(b).

The transverse intensity distribution of the light emitted out of a scintillating medium is a direct measure of the bunch charge density in the transverse plane. For beam energies below a certain threshold YAG screens are to be used, since, below this threshold, the angular distribution from an OTR is wide and therefore the photon count, i.e. intensity reaching the CCD chip, is not sufficient. On the other side, YAG crystals experience saturation for high charge densities. Using the minimum expected rms size after quadrupole focusing in the tomography module - 125 μm for beam momentum of about 32 MeV/c and charge of 1 nC, one can calculate an expected charge density of $10 \, ^{fC}/_{\mu m^2}$ and according to [95] this value could introduce saturation effects.

The minimum spot size resolvable by a YAG screen is limited by multiple scatering and by generation of bremsstrahlung. To calculate the minimum resolvable spot size at PITZ, different thicknesses d of the Si substrate of a YAG-doped screen with constant concentration of Ce atoms of N $= 2.5 \times 10^{19}$ cm^{-3} were used, yielding results as shown in Fig. 5.5(a) using
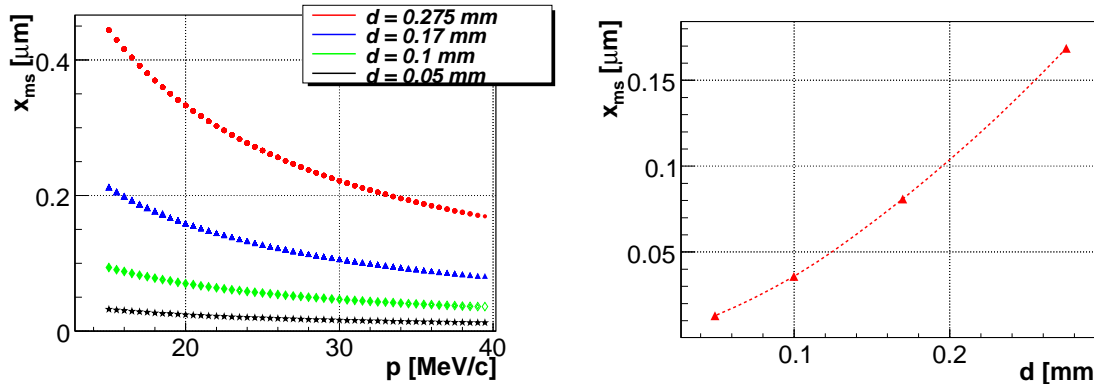
(a) Minimum spot size for different beam momenta in the PITZ range.

(b) Minimum spot size for different thicknesses of the Si layer of a YAG-powdered screen and beam momentum of 40 MeV/c.

Figure 5.5: Beam size limited by multiple scattering, x_{ms}, in a YAG-powdered screen.

$$\theta_{ms}[mrad] = \frac{13.6 MeV/c}{p} \times \sqrt{\frac{d}{Z0}} \times \left[1 + 0.038 \times \ln \frac{d}{Z0} \right], \tag{5.3}$$

as in [96] where $^d/_{Z0}$ is the thickness of the medium in radiation lengths $Z0$ and for the spot size

$$x_{ms}[\mu m] = \int_0^d \theta_{ms}(d) \mathrm{d}d. \tag{5.4}$$

As expected, with higher energies the beam size resolvable by the YAG screen is more limited, seen by the negative trend of the curves in Fig.5.5(a). For the minimum expected design value of $\sigma_{x,y} = 0.125$ mm, momentum of 32 MeV/c and nominal bunch charge of 1 nC, the beam size is still larger than those limits for thicknesses of 0.170 mm and below. Therefore, the thickness of the screens in the tomography module was chosen to be 100 μm.

To evaluate the efficiency of an OTR screen, the photon count defined by [97]

$$N_{photons} = QE \cdot \frac{Q}{q}, \tag{5.5}$$

where Q is the bunch charge and q - elementary charge, can be estimated. The factor QE - quantum efficiency, the number of photons generated in the optical band (λ_1, λ_2) from a single electron incident on the OTR foil, can be calculated using [97]

$$QE = \frac{\alpha}{\pi} (2 \ln \gamma - 1) \ln \left(\frac{\lambda_2}{\lambda_1} \right), \tag{5.6}$$

for $\alpha \approx {}^1/_{137}$ defined as fine structure constant. As it can be seen in Fig. 5.6(a) and 5.6(b), the QE and the photon count increase with the energy - as a reminder the CDS booster cavity is designed to reach beam momentum 40 MeV/c.

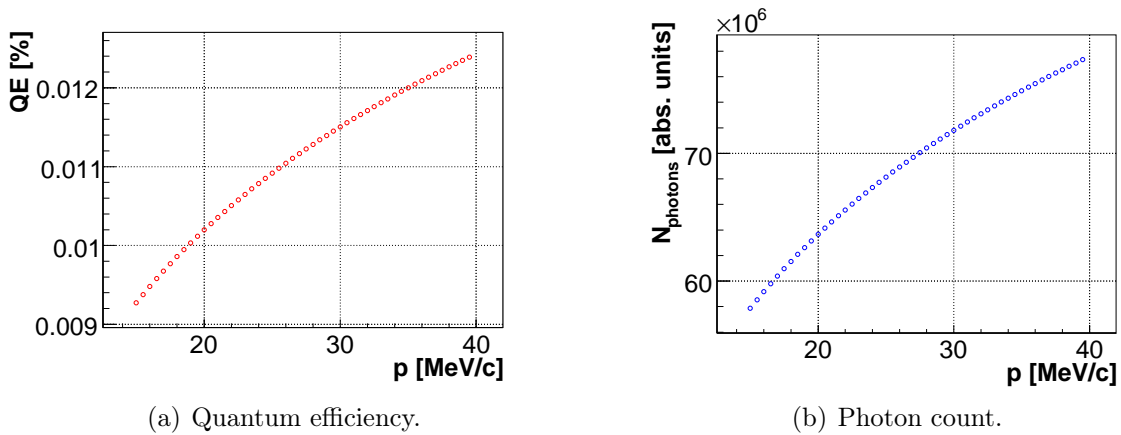(a) Quantum efficiency.

(b) Photon count.

Figure 5.6: Expected QE (left) and photon count (right) from an OTR screen for beam momentum between 15 MeV/c and 40 MeV/c, bunch charge of 1 nC and optical band in the visible spectrum 400–800 nm.

The OTR screens in the FODO lattice intercept the beam in skewed incidence and backward OTR is emitted at an angle θ $[rad] = {}^1/_\gamma$, where for PITZ, $\theta = [0.013, 0.034]$ inversely scaled to the energy. As it can be seen in Fig. 5.7(a), the peak intensity increases with the increase of the energy as this has already been demonstated many times. The optical aperture is estimated as $\theta_m = [-0.1; 0.1]$ rad [27] and therefore it is not expected that for low beam momenta a significant ammount of the light is lost.

The OTR screen at the entrance of the additional upstream FODO cell meets the beam at normal incidence, therefore the forward transition radiation is caught by the following mirror.
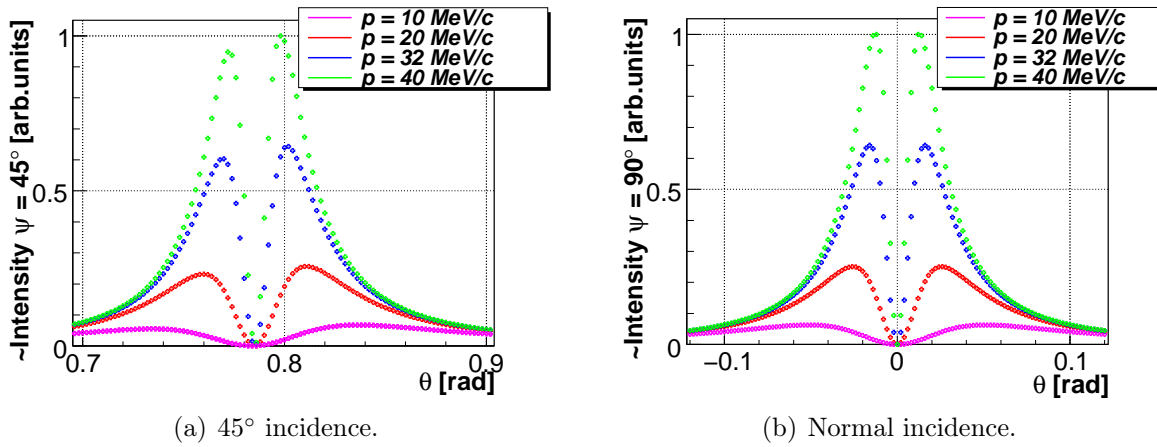
(a) 45° incidence. (b) Normal incidence.

Figure 5.7: Angular distribution of OTR for various beam momenta for 45° and normal incidence of the velocity vector. The intensity is normalized to the maximum one.

In this case the orthogonal component of the radiation vanishes [79]. The expected intensity, normalized to the maximum intensity, of the forward emission is shown in Fig. 5.7(b). The formulae used to obtain Fig. 5.7(a) and 5.7(b) can be found in [79,97].

5.3.3 FODO cells

An overview of a FODO cell with its corresponding BPM and steering magnet is shown in Fig. 5.8. The definition of a FODO cell requires two quadrupoles operated with opposite polarity separated by a drift space. In PITZ a cell is defined from screen to screen - it starts with a screen, followed by a drift space of length 0.1685 m defined as the distance between the edge of a quadrupole and the screen surface, a focusing quadrupole, drift of twice the length of the previous, a defocusing quadrupole and a drift identical to the first. Thus, the overall length of a cell is 0.76 m.

5.3.4 Components mounting tolerances

The performance of the tomography module stronly depends on the precision with which the components are mounted along the beamline. In this section the allowed misplacement of a component is discussed. For a quadrupole a misplacement might be related to:

- offset along the $z-$axis
- offset in the transverse planes
- rotation around the $z-$axis, i.e. roll angle
- rotation around the $x-$axis, i.e. pitch angle
- rotation around the $y-$axis, i.e. yaw angle

The quadrupoles along the matching section are subject only to transverse and angular misplacement. For the matching procedure it is sufficient to know with a good precision only their longitudinal position.

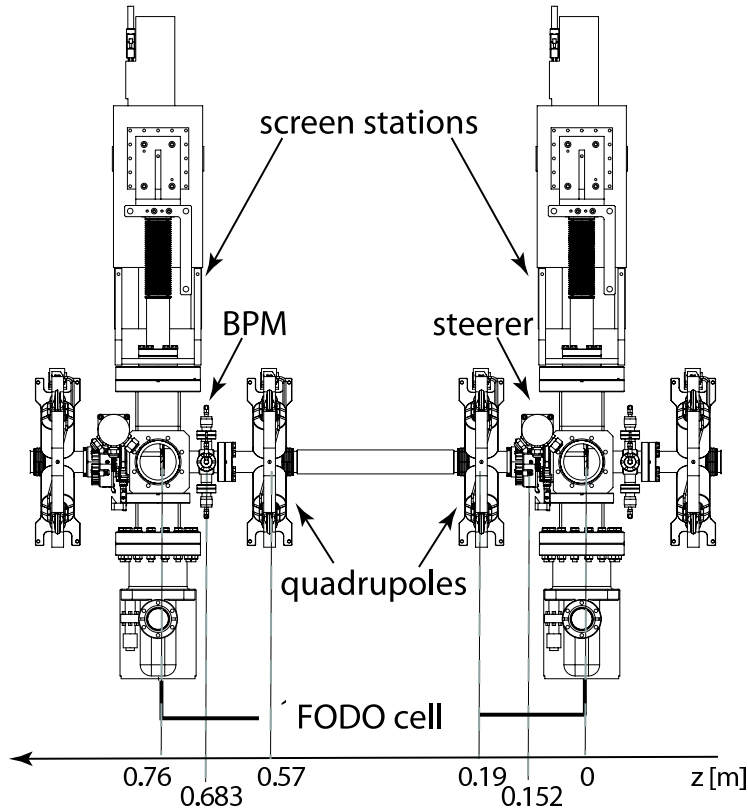A misplacement of a screen station is evaluated for:

Figure 5.8: Top view of a FODO cell with its quadrupoles, screen stations, a BPM and a steerer. The coordinate axis shows the middle positions of the components with respect to the beginning of the cell.

- offset along the $z-$axis
- rotation around the $x-$ and $y-$axis.

In order to stay within the conditions for identical cells, a maximum longitudinal offset of a screen and a quadrupole along the FODO lattice with respect to the first screen has to be defined. Since the matching is more sensitive for higher energies, the necessary calculations are performed on a model beam with a momentum of 32 MeV/c, normalized rms emittance of 1 mm.mrad, elliptical symmetry in the transverse planes and close to zero momentum spread so that a perfect matching along the tomography and matching sections can be achieved and linear transport is applicable. Such assumptions are optimistic for a real experiment. In what follows a random Gaussian error with standard deviation within some range is assigned to a component and the calculated parameter for each type of misalignment is the maximum mismatch of the resulting β functions in the horizontal and vertical planes compared to a matched periodic solution.

As the cell dimensions are small and the focusing is rather strong, the misplacement of an element has a strong impact. PITZ aims to measure emittances with a systematic error better that 10 % and, as it will be shown in chapter 5.4, this corresponds to an uncertainty of about 10 % in the measured spot size. The corresponding uncertainty in the Twiss β function in absolute units is about 0.05 m or in relative units 5 % of its design value of 0.999 m using

5.3. Design of the experimental setup

Eq. (5.1). Figure 5.9 shows the evolution of the β function along the FODO structure for
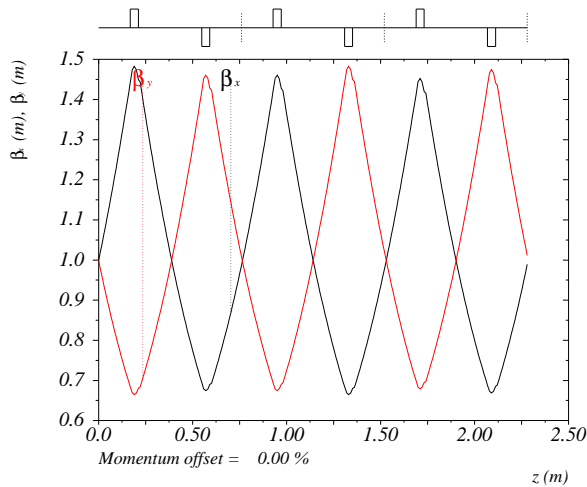

Figure 5.9: Twiss β function along the FODO lattice assuming only longitudinal misplacement of the quadrupoles. A random Gaussian error with $\sigma = 0.1$ is assigned to the positions of all the magnets in the FODO lattice. No other errors in the alignment are assumed.

a quadrupole misalignment of 0.1 mm in RMS units - the final mismatch is smaller than the required 5 %. No other possible alignment errors are assumed. Despite that on Fig. 5.9 the final β function is within the needed 5%, in the following it will be shown that this value, superimposed with other errors, will introduce a significant mismatch. Misplacement smaller than 0.2 mm is unrealistic due to the precision of the reference points drilled on the magnets shells by the producer for alignment purposes. Consequently, the smallest possible misalignment during the mounting is preferred as this value is 0.1 mm in rms units or twice that in absolute units. The same is valid for a translation in the x or y planes.

A roll angle introduces a dipole component in the magnetic field and cannot be compensated since there is no space for additional magnets along the beamline. The impact of 10 mrad and 15 mrad roll angle of a quadrupole as the x, y and z-offsets are within the above mentioned ranges is shown in Fig. 5.10(a) and Fig. 5.10(b). Except the exceedingly worse symmetricity of the beam envelope in the case of 15 mrad, the mismatch builds up to about 5 % on the last screen as opposed to the case of 10 mrad. Opposed to Fig. 5.9, the resulting β functions are underestimated which, as it will be shown in chapter 5.4, assumes an underestimation of the beam size and the measured emittance using a multi-screen technique.

A quadrupole can be misplaced in the (y, z) plane with an angle $d\phi$ as shown in Fig. 5.11. Magnets located all along the beamline are considered when evaluating $d\phi$. Simulations show that an rms value of 20 mrad keeps the β-mismatch below 1 % and the result is shown in Fig. 5.12. The same is the required value for rotation around the $y-$axis.

For considerations similar to the longitudinal misplacement of a magnet, the screens are limited to 0.1 mm offset in the z-direction. This can also be shown using equivalent triangles

(a) Twiss β functions along the FODO lattice resulting from a quadrupole roll angle of 10 mrad.

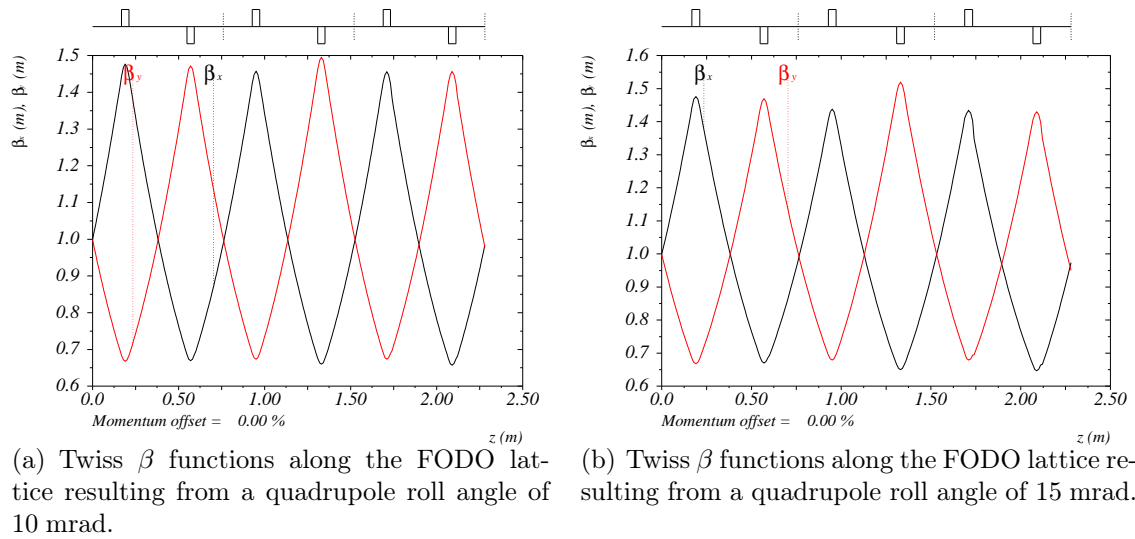(b) Twiss β functions along the FODO lattice resulting from a quadrupole roll angle of 15 mrad.

Figure 5.10: β-beating along the FODO lattice introduced by a quadrupole roll angle of 10 mrad and 15 mrad in RMS units. The misplacements along x, y and z-axes are allowed to be within the specified ranges of 0.1 mm.
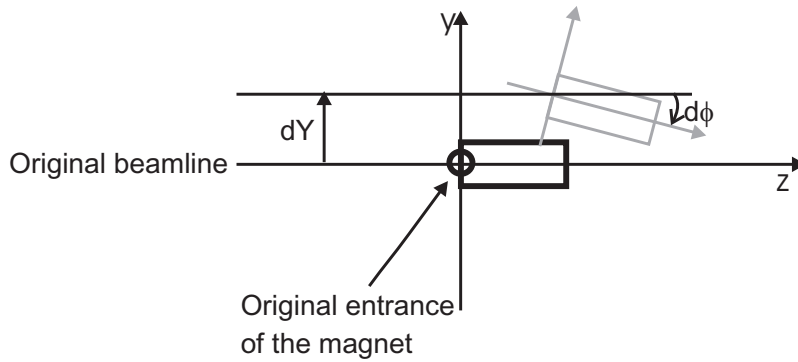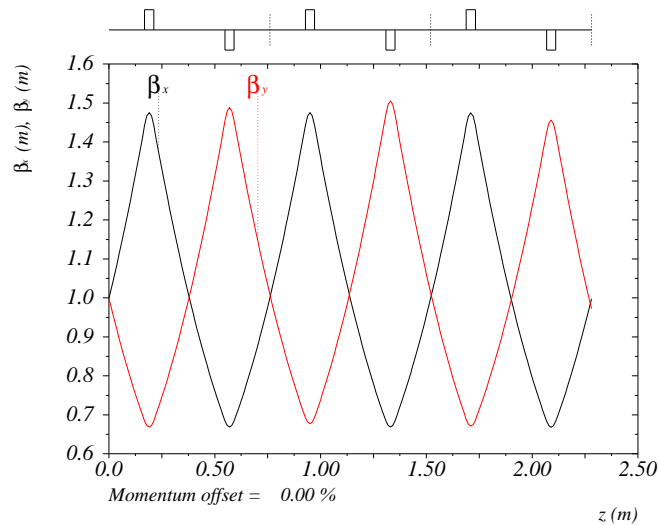
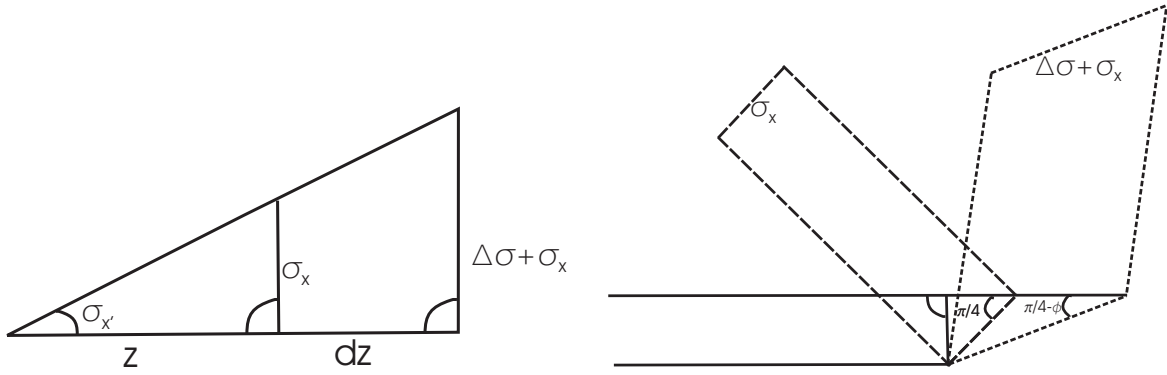

Figure 5.11: Quadrupole misalignment in (y, z) plane.

Figure 5.12: Twiss β functions along the FODO lattice resulting from a random quadrupole misplacement in (y, z) plane of $d\phi = 20$ mrad.

from Fig. 5.13(a) and the inherent beam divergence of 0.18 mrad for the above mentioned 1 mm.mrad transverse emittance and 32 MeV/c beam momentum. From geometrical con-

(a) Equivalent triangles can be used to define the maximum allowed misalignment dz of a screen along z, proportional to the allowed uncertainty in the measured beam size and the beam divergence.

(b) Geometry used to define the maximum allowed angle of rotation of a screen.

Figure 5.13: Geometries used to define screen tolerances. $\Delta\sigma$ denotes the uncertainty in the measured beam size, σ_x and $\sigma_{x'}$ are the real beam size and divergence.

siderations shown in Fig. 5.13(b) the maximal rotations around the x- and y- axes should be 10 mrad in RMS units.

In a summary the allowed misalignment tolerances are listed in Table 5.2.

Table 5.2: Alignment tolerances of components along the tomography and matching sections.

Element	Misalignment type	Range in RMS units	Units
	offset along z	0.1	mm
	offset in transverse planes	0.1	mm
Quadrupole	rotation around x-axis	20	mrad
	rotation around y-axis	20	mrad
	rotation around z-axis	10	mrad
	offset along z	0.1	mm
Screen	rotation around x-axis	10	mrad
	rotation around y-axis	10	mrad

5.4 Modeling a tomographic experiment

5.4.1 Monte Carlo simulations

The performance of the tomography module is studied with respect to errors in the parameters needed for emittance calculations. As the module can be used for multiscreen measurements as well as for tomographic reconstruction, both options are taken into account. Moreover, the performance of the reconstruction depends strongly on the accuracy of the matrix transport and, therefore, the multiscreen approach is needed for matching.

The phase advance between the FODO cells has been chosen so that there is a minimum error in the measured emittance for a setup consisting of four screens. By definition the tomographic reconstruction requires equidistant angular steps, therefore the phase advance has to be 45°. Using Monte Carlo simulations described in chapter 5.1, it has been shown that the deviation in emittance, calculated by the multiscreen approach, is minimized for this phase advance for both transverse planes - Fig. 5.14. In the simulations a normalized
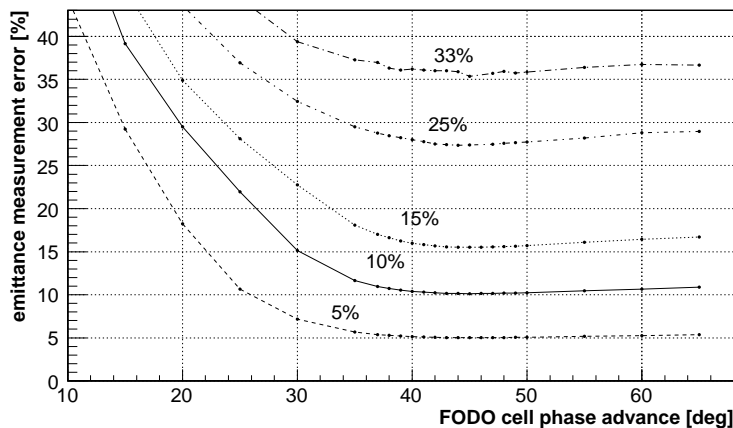

Figure 5.14: Emittance measurement error as a function of the phase advance for different initial beam size errors. The Monte Carlo simulations decribed in Chapter 5.1 have been used to obtain the results.

geometrical emittance of 0.9 mm.mrad as needed for the XFEL injector setup and a beam energy of 32 MeV were assumed. The bunch charge is 1 nC even though this is irrelevant because the Monte Carlo simulations use a linear matrix approach. For the full range of assumed beam size errors between 5 % and 33 %, the error in the measured emittance is minimal for a phase advance between two neighbouring screens of $\pi/4$.

Taking into account the FODO cell geometry and the required phase advance between two screens the design Twiss parameters can be found. They are listed in Table 5.3. A graphical representation of the Twiss β function is given in Fig. 5.15.

Table 5.3: Twiss parameters on the screens as needed for a phase advance of 45° between the FODO cells.

Parameter	x-plane	y-plane
$\beta[m]$	0.999	0.999
α	-1.125	1.125

In an experiment the Twiss parameters are periodic only if they are properly matched to the optics of the lattice. If they are different the beam is mismatched - see chapter 3.4. A way to estimate the mismatch in the β function is given by Eq. (5.1). An equivalent method is to analyse the correspondence of the experimental ellipse parameters to the designed ones

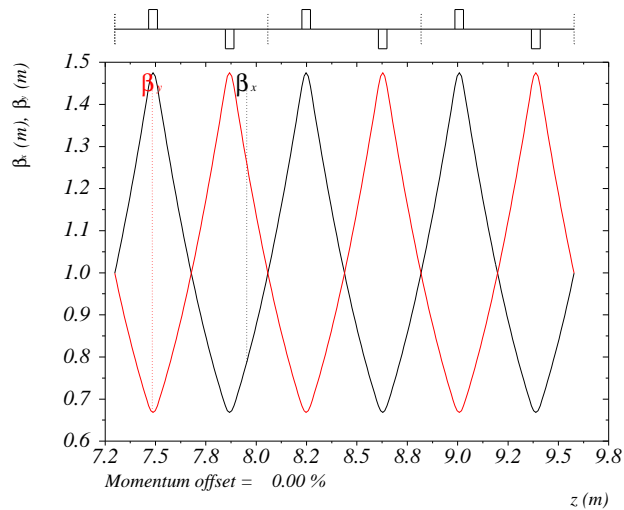## 5.4. Modeling a tomographic experiment

Figure 5.15: Theoretical β function along the tomography section. The z-coordinate is with respect to the position of the first matching element used in the simulation - as a rule of thumb this is a screen station along the PITZ beamline. The arrangement on the top shows the sequence along the lattice - a dashed vertical line represents a screen, a box on the upper side is a quadrupole focusing the horizontal plane, a box on the lower side - a vertically focusing magnet. The MAD code was used to obtain the needed quadrupole strengths.

or the parameter ξ defined as in [98]

$$\xi = \frac{1}{2} \left(\beta \gamma_d - 2\alpha\alpha_d + \gamma\beta_d \right),$$ (5.7)

where the subscript d denotes the design values. For an ideal matching $\xi = 1$. If the beam is mismatched the parameter $\xi \cdot \varepsilon$ shows the increase in emittance. In order to distinguish Eq. (5.7) from Eq. (5.1), Eq. (5.7) will be called phase-space mismatch.

A graphical representation of the quality of the match can be achieved considering the design ellipse at the location of observation plotted in normalized phase-space coordinates

$$\left(\frac{x}{\sqrt{\beta_x}}, \frac{\alpha_x x + \beta_x x'}{\sqrt{\beta_x}} \right)$$ (5.8)

and normalized to unit radius. Then, an ellipse, derived from a phase-space distribution and normalized to the design one, is superimposed on it. The orientation of this ellipse corresponds to the angle enclosed between the major semi-axis and the abscissa of the normalized phase space and shows the possibly mismatched phase [52]. This angle is defined in the same way as in Fig. 3.5. The mismatch in the areas of the two ellipses represents the emittance deviation. Such an example for the horizontal plane is given in Fig. 5.16. The design ellipse there corresponds to an ellipse, having design Twiss parameters, defined on a screen along the tomography module. If, for some reason, the Twiss β is well adjusted but the α is not as the beam meets an observation location downstream, the ellipse at that location will transform to one like the black or the green.
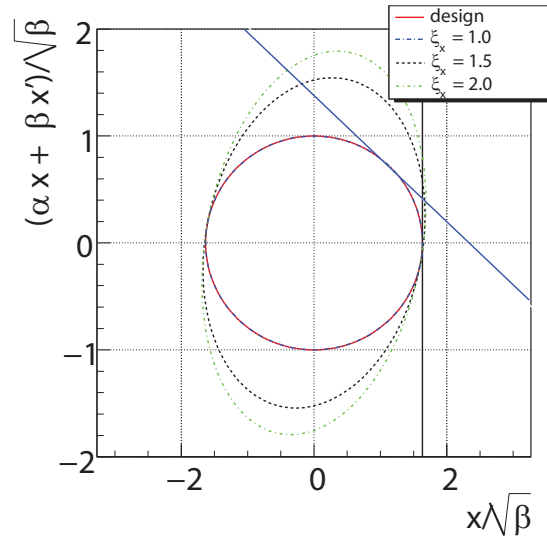
Figure 5.16: A design ellipse in normalized phase-space coordinates in solid red superimposed to ellipses corresponding to certain phase-space distributions in dashed blue, black and light green. The location of observation here is chosen to be screens along the tomography module. The lines represent the rms spot sizes, normalized to the design values and rotated to the phase advance at the observation locations. Their orientation shows the coverage of the phase space. The mismatched ellipses are generated so that the β function corresponds to the design one and the α does not. If the injected beam is matched on the first screen along the tomography module it is represented by the blue circle. If then, due to wrong transport, the beam propagates downstream to the next screen having the same β but different α, the blue circle is transformed into an ellipse like the black or the green.

As the matching relies on the measured beam sizes, errors in those values will contribute to the final emittance. Furthermore, multiscreen measurements make use of Eq. (3.26) which might not have a real solution. This probability and the error in the emittance for different relative spot size errors are shown in Fig. 5.17. Here one assumes some uncertainty in the
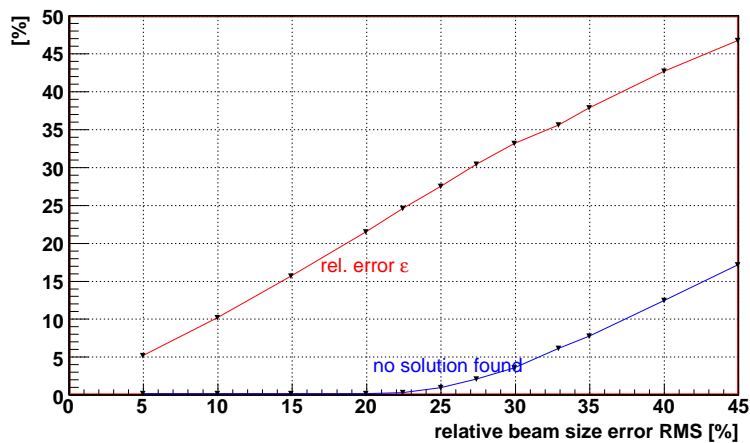

Figure 5.17: Relative emittance deviation and rate of no solution of the emittance equation Eq. (3.26) as functions of the relative beam size error. Betatron phase advance of 45°, normalized geometrical emittance of 0.9 mm.mrad and beam momentum of 32 MeV/c are assumed in the Monte Carlo simulations.

measured beam sizes on the screens along the tomography section. The emittance, resulting from those perturbed spot sizes, is then calculated using the multiscreen approach for 10000 seeds. As it can be noticed, a solution always exists for relative spot size errors below 20 %. For values above that, the curve representing the rate of no solution has a steep slope. If the relative error in the measured rms spot sizes is maintained below 10 %, the distribution of the mismatch parameter ξ, i.e. the ratio between the perturbed and the design emittances, over 10000 seeds in the Monte Carlo simulations follows a Gaussian with mean $\mu = 1$ and $\sigma = 0.1$ - Fig. 5.18 with black solid curve, as $\xi = \varepsilon/\varepsilon_0 \subseteq [0.65, 1.56]$. For higher relative spot
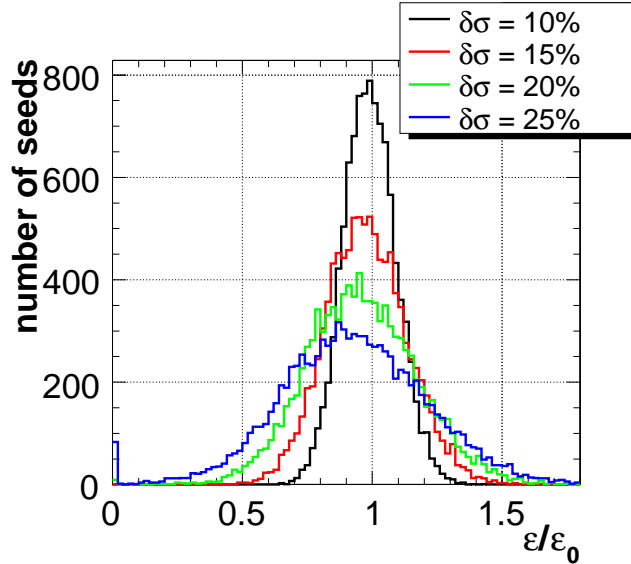

Figure 5.18: Emittance distribution normalized to design emittance ε_0 of 0.9 mm.mrad for relative beam size error of 10 %, 15 %, 20 % and 25 % outlined respectively in black, red, green and blue. For smaller relative spot size errors $\delta\sigma$ the probability distribution is Gaussian as the higher the error the bigger the sigma of the distribution and its mean tends to underestimate the emittance.

size errors the tails of the Gaussian curve extend. Moreover, for higher errors the probability distribution is no longer symmetric around a mean $\mu = 1$ with tails extended towards smaller emittance making negative emittance values possible. This can be seen by the peak at $\varepsilon/\varepsilon_0$ which tends to 0 for $\delta\sigma = 25\%$. In the case of 25% spot size error the Gaussian has a mean $\mu = 0.83$ and $\sigma = 0.26$ as $\xi \subseteq [0, 2.16]$.

Visualizing the values of the Twiss α and β, calculated from the perturbed beam sizes, emittance and corresponding to a certain ξ parameter, one can see the allowed deviation of α and β so that a small phase-space mismatch is achieved. Such an example is given in Fig. 5.19(a) and Fig. 5.19(b) for 10% and 20% spot size errors correspondingly. The black solid lines cross at the design Twiss parameters. The coloured area shows the counts in the Monte Carlo simulations where the phase-space mismatch falls, having predefined errors on the fours screens in the tomography module, and the range of change of the Twiss functions. White regions exclude the probability to have any emittance and Twiss functions for particular uncertainty in the spot size, i.e. there is no hit from the simulations. The colour map shows the number of hits for some ξ. The spread of the area here reveals the

(a) Spread for spot size error of 10%.   (b) Spread for spot size error of 20%.
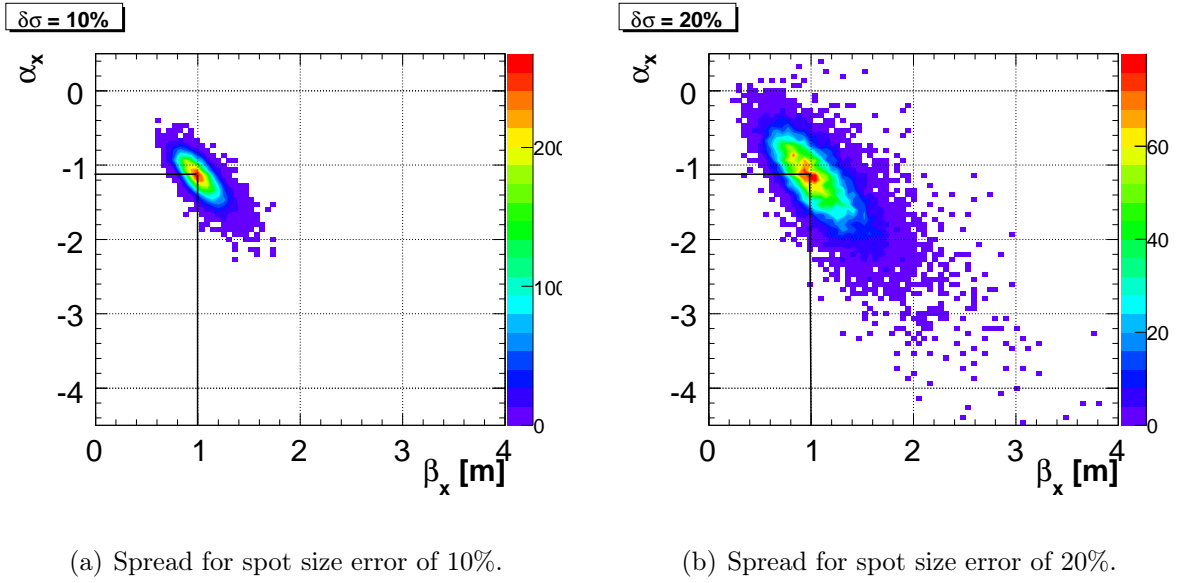
Figure 5.19: Spread in Twiss parameters propagated backwards to the first screen along the FODO lattice, resulting from the emittance calculated out of four perturbed spot sizes on the screens in the tomography module. The area where the Twiss functions, and correspondingly the emittance, are mismatched increases as expected from Fig. 5.18. The colour map shows the probability to have a particular pair (α, β) - in yellow-red in the case of 10% beam size error fall more than 200 events from the Monte Carlo with nearly the same ξ parameter.

same as the extended tails in the Gaussian curves from Fig. 5.18 and the number of hits depicted in red - the decrease in the peaks of the Gaussian curves from Fig. 5.18.

A possible error source contributing to the measured emittance is an uncertainty in the beam momentum p. Assuming p_m is the measured momentum and Δp - the error in absolute units, being negative or positive, then $p_m = p + \Delta p$. Thus, the real quadrupole strength k_m will be

$$k_m = \frac{k}{1 + \frac{\Delta p}{p}}, \tag{5.9}$$

where k is the quadrupole strength for a matched periodic solution. Fig. 5.20 shows the
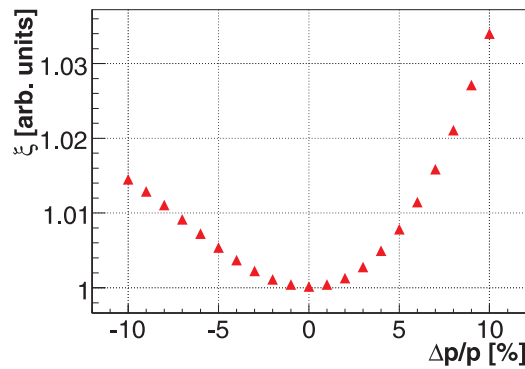

Figure 5.20: Ellipse mismatch parameter on the last screen of the tomography module as a function of the relative error in momentum measurements.

dependence of the mismatch parameter ξ as a function of the relative momentum error. A

matched solution is assumed at the entrance of the FODO lattice and the quadrupoles along the lattice will be either stronger than needed or weaker with some random value defined by the value of $\Delta p/p$. The mismatch is estimated at the position of the last screen along the tomography module as there the β function will be influenced by beats along the full FODO lattice. For that reason the curve is not symmetric with respect to the momentum error. For PITZ the systematic uncertainty of the first high energy spectrometer dipole HEDA1 has been estimated to be below 5% [35] and therefore the mismatch parameter due to momentum error is below 1% in relative values or neglibly small if this would be the only source of uncertainty.

5.4.2 Matching of the electron beam

The tomography module designed for PITZ should be usable in a range of beam momenta between 15 and 40 MeV/c. Earlier, in chapter 3 Fig. 3.6, it was shown that, over the full energy range, the beam dynamics of the electron bunch is influenced strongly by space-charge effects. Thus, the external quadrupole focusing will be partially cancelled by the defocusing effect induced by the space-charge forces and, therefore, it has to be compensated by appropriate matching all along the matching and tomography sections.

A beam will be defined as matched if it satisfies the conditions of Eq. (3.36), i.e. the purpose of the matching procedure is to prepare the beam in front of the tomography module so that β_x, β_y, α_x and α_y are equal to their design values from Table 5.3 on the screens in the tomography module. In order to follow such a condition one needs to adjust the strengths of the quadrupoles used along the matching and tomography section. The gradients of the quadrupole magnets inside the tomography module do not depend on a particular beam energy, i.e. if the space-charge effects are negligible those gradients are valid for any beam parameters. In the tomography section the beam undergoes a transition from space-charge to emittance dominated regime - Fig. 3.7, and it is still needed to adjust the quadrupoles along the FODO lattice slightly. In the steps described below the matching is always initiated with MAD because of its simplicity of usage. If stated so, an additional matching is done using TRACE-3D in order to check its applicability for high-charge density beams. The verification of either MAD or TRACE-3D results is done with the macroparticle tracking routines of ASTRA.

In order to determine the most appropriate matching, a number of physical matching setups have been evaluated with respect to the conditions to deliver a phase advances of 45° in both transverse planes along the FODO lattice and achieve a β-mismatch below 15 % again for both planes. Using Monte-Carlo simulations it has been shown that for a relative beam size error of 20 % the value of the emittance can always be determined - Fig. 5.17.

A theoretical solution of the beam envelope trajectory, based on transport maps, is shown in Fig. 5.15. To verify the linear transport of this solution with numerical simulations, ASTRA has been used for a beam momentum of 32 MeV/c, transverse emittance of

1.17 mm·mrad at the location of the first EMSY station (EMSY1) from Fig. 2.1, at first neglecting space-charge effects. These non-realistic simulations are conducted here and for later iterations to demonstrate the detrimental effects the space charge has on the performance of the tomographic reconstruction. The resulting β-function is shown in Fig. 5.21(a) - here the ASTRA solution is shown with a solid line and superimposed with a dashed line is the theoretical MAD solution. Fig. 5.21(b) shows the corresponding phase advances - according to the definition of phase advance - Eq. (3.20) - it is fixed between two beamline positions if the envelope of the betatron oscillations β between those two positions is fixed. It can be seen that there is some minor mismatch in the β-functions.
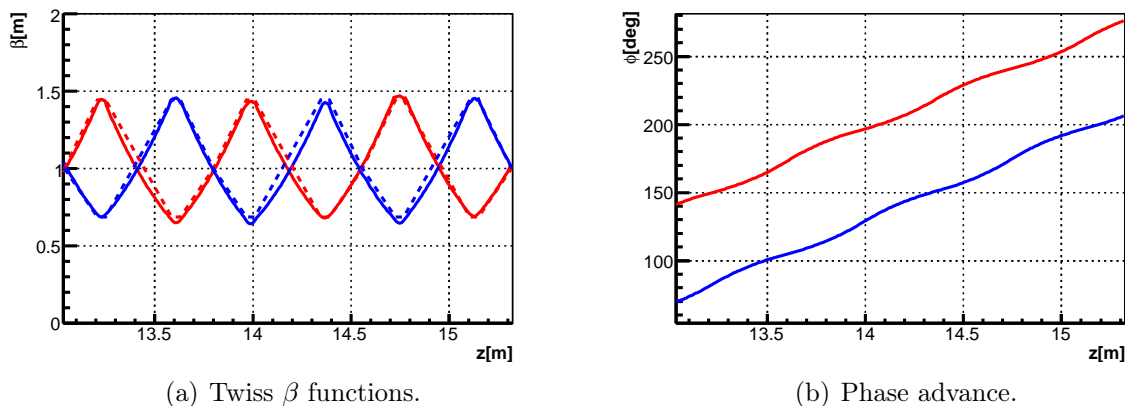

(a) Twiss β functions.

(b) Phase advance.

Figure 5.21: β-functions and phase advances obtained with MAD (dashed curves in the β evolution) and ASTRA (solid curves). Red colour represents the horizontal plane, blue - the vertical. Space-charge forces are excluded from the numerical tracking. The screens along the tomography module are located at the even crossings of the design MAD β_x and β_y or at 13.04, 13.8, 14.56 and 15.32 m from the cathode. The matching quadrupoles are all but the first two along the beamline in Fig. 2.1.

Quantatively, for the two transverse planes, it is below 1 %. The mismatch in phase space for the vertical plane can be seen in Fig. 5.22 and the result is similar for the horizontal plane. There is an increase in the area of the normalized rms ellipses even if they look concentric with the design one. As the area of the rms ellipse is equivalent to emittance, one would assume the projected emittance increases. This is indeed the case - the emittance increases by 2 % along the matching section and stays nearly constant along the FODO lattice.

Such a mismatch can be qualified as fairly good but it has to be kept in mind that it is achieved for unrealistic conditions. The realistic case when the particles counteract with each other, i.e. the space-charge effects are included in the numerical tracking, is shown in Fig. 5.23(a) and Fig. 5.23(b). The β-mismatch increases to 38 % - quantatively the β-functions and the phase advance are summarized in Table 5.4 and Table 5.5.

Using multiscreen technique, the projected normalized emittances at the position of the first screen in the tomography module for the horizontal and the vertical transverse planes have been estimated to have 3.4 % and 2 % relative error, correspondingly, with respect to ASTRA. The calculated values are $\varepsilon_{x,N} = 1.21$ mm·mrad and $\varepsilon_{y,N} = 1.2$ mm·mrad versus ASTRA values of 1.17 mm·mrad and 1.18 mm·mrad. How the normalized phase space would
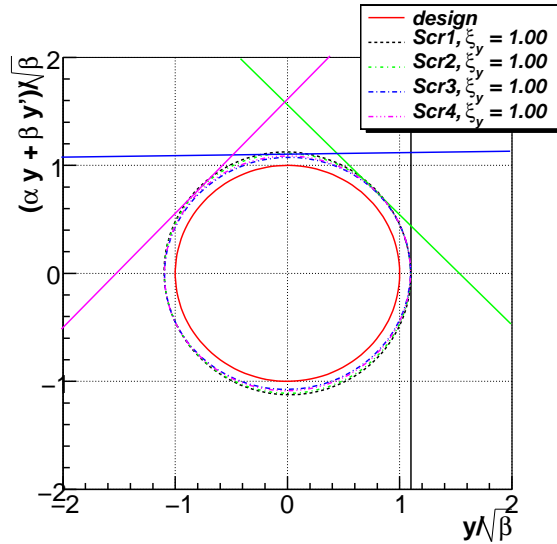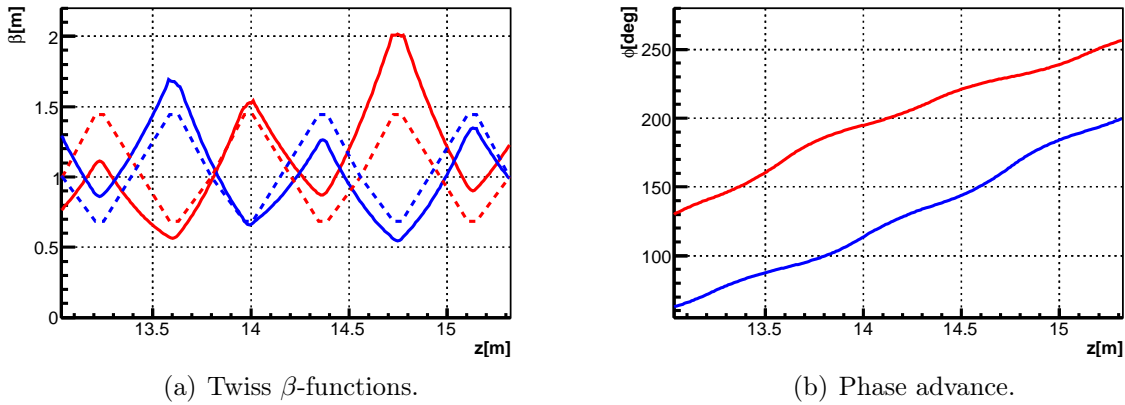
Figure 5.22: The ellipses for the vertical plane, obtained on the four screens and normalized to the design ellipse in normalized coordinates. The results are similar for the horizontal plane.

(a) Twiss β-functions.

(b) Phase advance.

Figure 5.23: β-functions and phase advances obtained with MAD and ASTRA in the same colour scheme as above. Beam with momentum of 32 MeV/c and normalized emittance of 1.17 mm·mrad, estimated on EMSY1, is tracked including the space-charge forces for a bunch with 1 nC charge. All but the first two quadrupoles from Fig. 2.1 are used for matching.

Table 5.4: β-functions on screens and β-mismatch calculated using Eq.(5.1) for the graphical representation in Fig. 5.23(a).

	Design	Scr.#1	Scr.#2	Scr#3	Scr.#4	$\Delta\beta$
$\beta_x\,[m]$	0.999	0.770	0.966	1.378	1.224	38 %
$\beta_y\,[m]$	0.999	1.290	1.107	0.828	0.985	29 %

look like in this case is shown in Fig. 5.24.

In practice the β-mismatch and the phase-space mismatch ξ, shown in Fig. 5.23(a) and Fig. 5.24, are identical. For machines like PITZ the ξ parameter is in general not defined because, looking for optimum injector conditions, PITZ operates at different regimes of charge density and volume of the electron beam in the six-dimensional phase space. Even

Table 5.5: Phase advances between the screens for the graphical representation in Fig. 5.23(b).

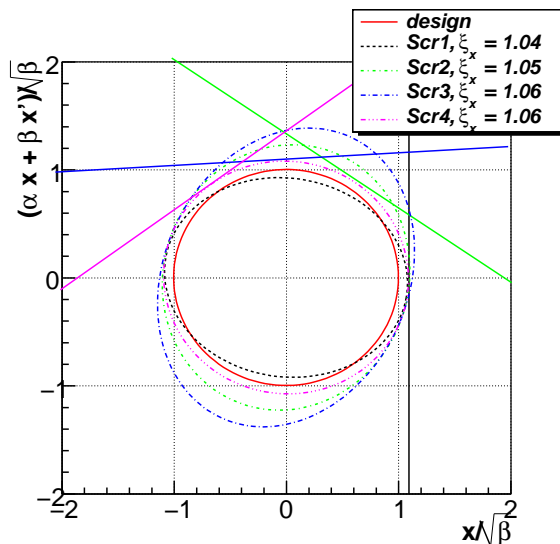|	**Design**	**#1 → #2**	**#2 → #3**	**#3 → #4**
$\varphi_x \,[^\circ]$	45	55.3	37.94	33.05
$\varphi_y \,[^\circ]$	45	36.67	48.13	52.04

Figure 5.24: Normalized phase space rms ellipse with superimposed ellipses from the screens along the tomography module for beam momentum 32 MeV/c, 1 nC bunch charge and normalized emittance of 1.17 mm· mrad calculated on EMSY1. Space-charge forces are included in the ASTRA simulations.

though for measurement techniques like the tomography ξ is a useful representation, in the following the visualisation of the β-mismatch will be prefered.

Decrease in the beam energy degrades the smoothness of the periodicity of the particle trajectories, due to increase of the influence of the space-charge forces. An example for slightly lower energy - 25 MeV, 1 nC bunch charge and normalized transverse emittance of 0.73 mm·mrad at the position of EMSY1, using the same matching setup is shown in Fig. 5.25(a) and Fig. 5.25(b). Space charge is included in the numerical tracking and the periodicity of the Twiss β-function is worse than in the case depicted in Fig. 5.23(a). Quantatively the β-mismatches are 220 % and 92 % for the horizontal and the vertical transverse planes.

Comparing the β-functions in the last two cases - 32 MeV/c and 25 MeV/c, it can be concluded that the space-charge defocusing requires optimization of the matching setup and the quadrupoles gradients which is subject to the discussion in the next section.
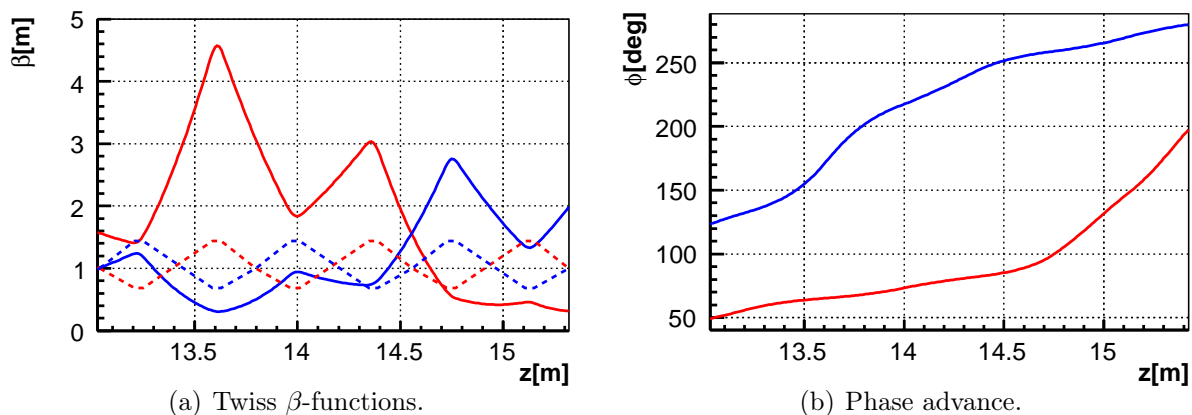
5.4. Modeling a tomographic experiment

(a) Twiss β-functions.

(b) Phase advance.

Figure 5.25: β-functions and phase advances obtained with MAD (dashed curves) and ASTRA (solid curves) for a beam with momentum p = 25 MeV/c, emittance of 0.73 mm·mrad for 1 nC bunch charge. Red colour represents the horizontal transverse plane, blue - the vertical plane. Space-charge forces are included in the numerical tracking. Quadrupole focusing additional to the predicted from the linear matching is not applied and, consequently, the β-mismatch is worse. The matching is done with all but the first two quadrupole magnets shown in Fig. 2.1.

5.4.2.1   Nominal setup of the matching section

The matching in the above two cases is obtained using a "nominal" physical setup, consisting of three FODO cells and seven matching quadrupole magnets. The magnets used are all but the first two shown in Fig. 5.26 - they are introduced later in Section 5.4.2.2. Further, the
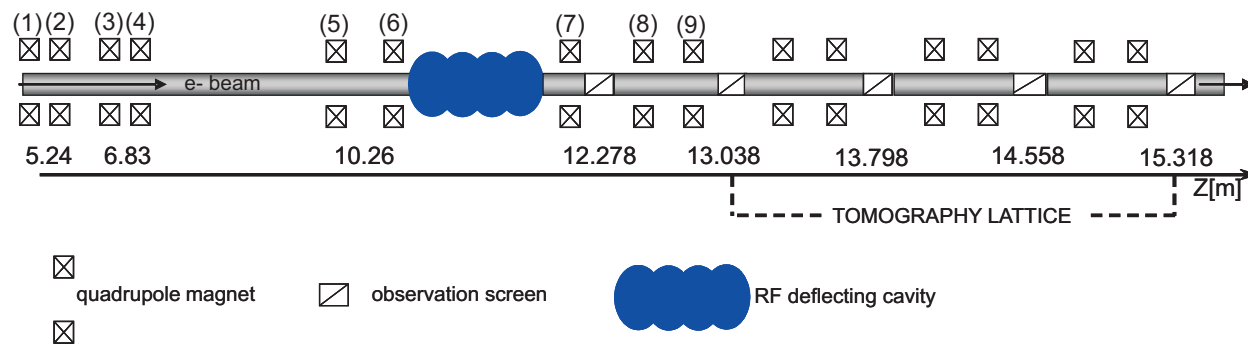

Figure 5.26: Nominal matching section (not to scale) with two additional quadrupoles at the beginning. The numbers on the quadrupoles in the matching section are indicated at the top side.

physical layout of the matching section has been modified in a number of iterations which will be described in the following. One of the constraints imposed during the searches for a solution, converging to the desired Twiss functions on screens, is a maximal quadrupole gradient of 6 T/m for any beam energy in order to stay within the linear part of the hysteresis. Another constraint might be to require a symmetric beam spot along long drifts in the matching section in order to keep the space-charge effects about symmetric for the two transverse planes. The latter has been used in the examples shown above.

Let's assume the matching constraints are related only to the quadrupole gradients and the desired Twiss functions on the first screen. The electron beam has a normalized emit-

tance of 1 mm·mrad, momentum of 32 MeV/c and uncorrelated momentum spread[1] of about 160 keV, bunch charge of 1 nC or equivalently 50 A peak current. A theoretical matching with MAD for this case is shown in Fig. 5.27. The results of numerically tracking this MAD solution in the case when space charge influence is neglected are shown in Fig. 5.28. Such a
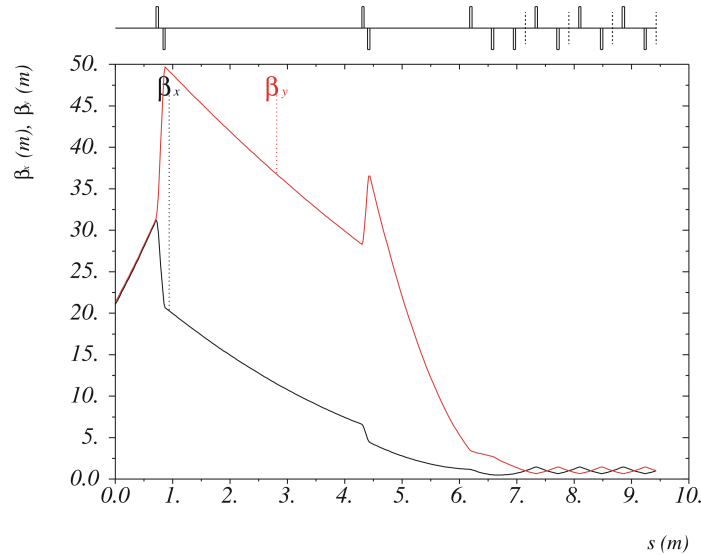

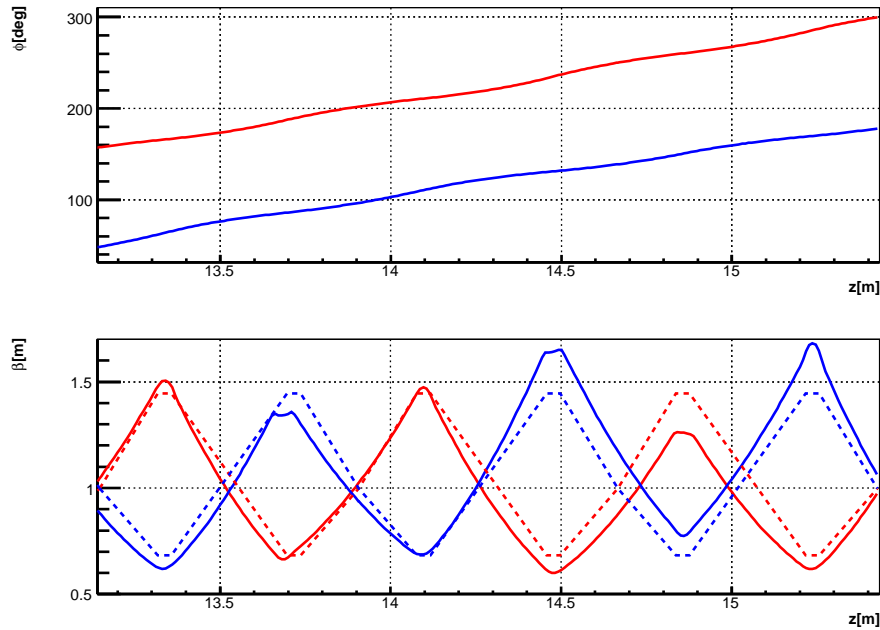Figure 5.27: β-functions along the matching and tomography section obtained with MAD.

Figure 5.28: β-functions and phase advances obtained with MAD (dashed curves) and ASTRA (solid curves). Red colour represents the horizontal plane, blue - the vertical plane. Space-charge forces are excluded from the numerical tracking.

solution delivers β-mismatches $\Delta\beta$ of 12 % and 18 % for the horizontal and vertical planes.

[1]The uncorrelated momentum spread $\sigma_{p_z}^2$ does not consider the longitudinal position of a particle within the bunch. Different longitudinal slices are characterized with different correlated momentum spreads as a function of the position of the particles with respect to the waves in the accelerating cavities.

5.4. Modeling a tomographic experiment

Including the space charge in the tracking results in mismatches of $\Delta\beta_x = 48\,\%$ and $\Delta\beta_y = 419\,\%$, depicted in Fig. 5.29 in blue, calculated using numerical data on the screens of the tomography section. Clearly, the beam dynamics is strongly influenced by the particles' repulsion and one needs to correct the quadrupoles gradients for that.

In order to estimate how far from the optimum the current solution is, ASTRA is used in a sequence of iterations for each couple/triple of quadrupoles using the following idea - find the strengths of each two/three quadrupole magnets which deliver the smallest mismatch with respect to the case of no interactions within the electron bunch. The so called "cost function" Δ depends on the beam sizes $\sigma_{x,y}$ as $X(z) = 4\sigma_x$, $Y(z) = 4\sigma_y$, and on the slopes $X(z) = 4\sigma'_x$ and $Y'(z) = 4\sigma'_y$:

$$\Delta^2 = (\delta X'_w - \delta X'_{wo})^2 + (\delta Y'_w - \delta Y'_{wo})^2 + (\sigma_{x,w} - \sigma_{x,wo})^2_{z_{end}} + (\sigma_{y,w} - \sigma_{y,wo})^2_{z_{end}}, \qquad (5.10)$$

where w denotes simulations with space charge included, wo - space-charge calculations discarded, and

$$\delta X'_n = \frac{4\left(\sigma_{n,x,z_{start}} - \sigma_{n,x,z_{end}}\right)}{L},$$

shows the focusing effect on the beam size σ_x for n being either w or wo. Analogously for $\delta Y'$. $L = z_{start} - z_{end}$ refers to the length of the beamline where the space charge is acting with z_{start} the beginning and z_{end} the end, including the number of quadrupoles being optimized. The first two terms in Eq. (5.10) estimate the defocusing introduced by the space-charge forces along the full length $z_{end} - z_{start}$. Each of them shows how the β-functions change due to space charge. The last two terms come into the equation to correct for the difference between the beam sizes at the end of the section. The beam envelopes are multiplied by a factor of 4 in order to use the definition of an equivalent RMS ellipse (see chapter 3, Eq. (3.26) and the corresponding footnote) and to maximize the charge density used to calculate the values. The cost function has to be minimized in a number of iterations where the strength of each magnet from the transfer map solution is corrected with a predefined value

$$\delta k = \frac{L}{L_{eff}} \cdot \frac{K}{R^2},$$

where L_{eff} is the quadrupole effective length, K is the generalized perveance and R is the beam radius. L is chosen so that there are no magnetic fields at its beginning and its end and it fully includes the quadrupoles on which the correction is done. δk can be changed in each successive iteration to a value where Δ is expected to be smaller. This iterative procedure has to include no less than two quadrupoles at a time if one needs to correct for both transverse planes simultaneously. The process is rather time consuming but in this way the mismatch has been decreased by a factor of about four inside the FODO lattice with respect to the previous $\Delta\beta_x = 48\,\%$ and $\Delta\beta_y = 419\,\%$ - now $\Delta\beta_x = 17\,\%$ and $\Delta\beta_y = 80\,\%$. A graphical comparison of the result is presented in Fig. 5.29 where the red curves are the

β-functions in the case when no space charge is included in the tracking, the blue ones are for the tracking without quadrupole strength correction and the green show the envelope after the above mentioned correction.
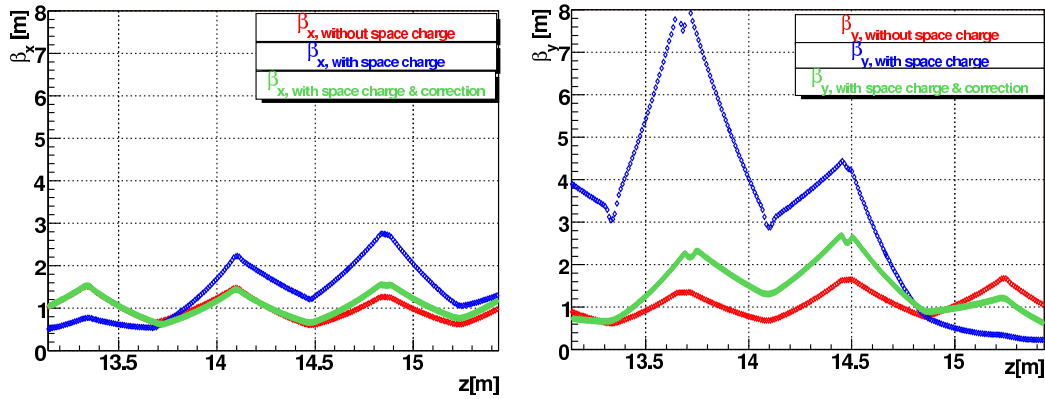

Figure 5.29: β_x (left) and β_y (right) along the tomography section using quadrupole strengths obtained after matching with MAD and ASTRA. The electron beam has 1 mm·mrad normalized projected emittance, 32 MeV/c momentum, 1 nC bunch charge. The red curves represent an ideal solution where the bunch dynamics is subject only to linear external focusing, they are the same as the ones shown with solid curves in Fig. 5.28. The case for which the space-charge forces are considered in the numerical tracking but the quadrupole focusing is not compensated for those effects is shown in blue - the mismatches $\Delta\beta$ are 48 % and 419 % for the horizontal and the vertical planes correspondingly. The green curves show the beam envelope subject to space charge and corrected quadrupole strengths - the resulting $\Delta\beta$ are 17 % for the horizontal and 80 % for the vertical planes.

Using the same setup and beam parameters the matching has been performed also with TRACE-3D. Results from this matching and consequent tracking are shown in Fig. 5.30. The result for the horizontal plane is relatively good but for the vertical it does not differ
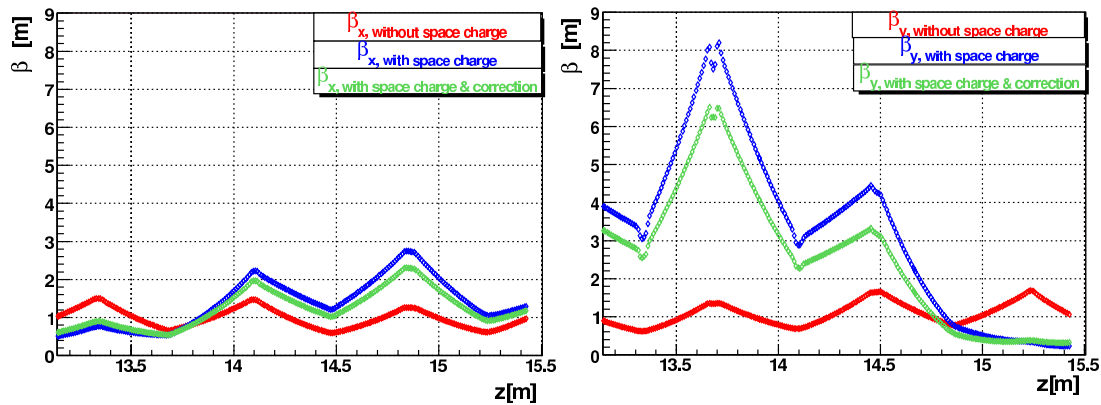

Figure 5.30: β_x (left) and β_y (right) along the tomography section using quadrupole strengths obtained after matching with TRACE-3D.

from the simple linear approach MAD uses. A possible explanation for the unsatisfactory performance is the fact that TRACE-3D cannot predict emittance growth due to space

charge while from numerical simulations it can be seen that the transverse emittances for the two planes grow asymmetrically.

5.4.2.2 Matching section of nine quadrupoles

In the PITZ beamline there are two more quadrupole magnets, located upstream - the first two shown in Fig. 5.26, Number 1 and 2. Adding them to the matching setup is another possible matching layout whose purpose has been to discard strong transverse kicks from the magnets downstream and consequently decrease the maximum excursion of the β-functions. At the same time the adjacent magnets in the first two pairs are very close to each other due to space limitations and, thus, overlapping fringe fields may introduce additional distortion.

Matching using the nine quadrupoles has been obtained using $TRACE - 3D$ and the beam has been tracked with ASTRA including space-charge calculations. As can be seen from Fig. 5.31 no periodic solution has been obtained. It's again clear that $TRACE - 3D$
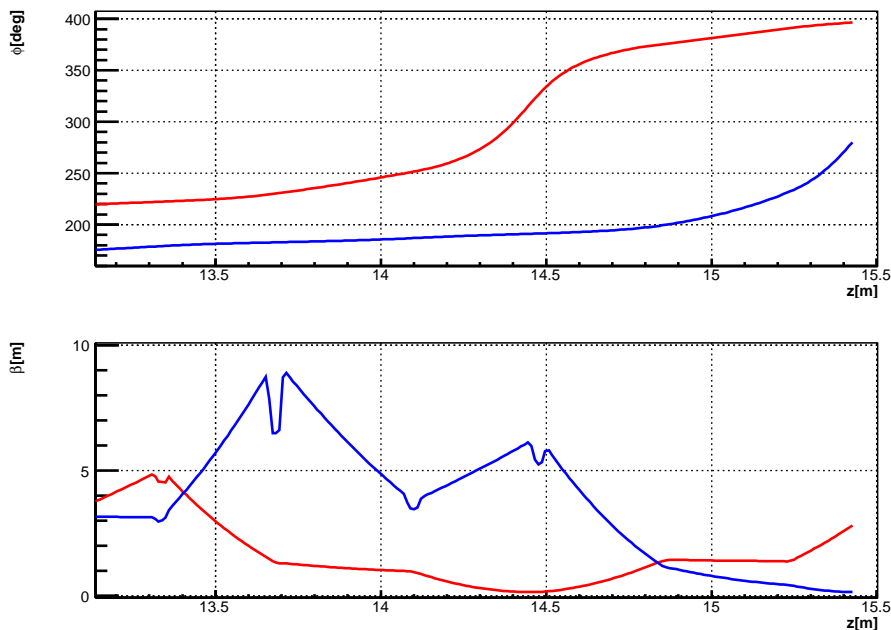

Figure 5.31: Phase advance (top) and β-function (bottom) along the tomography section using nine matching quadrupoles, resulting from macroparticle tracking with ASTRA. Good matching was obtained using TRACE-3D while the ASTRA tracking of this solutions reveals no periodic solution for either of the transverse planes.

does not offer a more convenient matching approach. The quadrupole strengths have to be corrected according to the scheme proposed in section 5.4.2.1. Since the usage of nine quadrupoles does not lead to a better matching while it needs two more magnets to be adjusted, this setup is not prefered.

5.4.2.3 Matching section of five quadrupoles

Another possible matching setup consists of the quadrupole magnets Number 2, 5 and 7 to 9 as shown in Fig. 5.26. The idea behind using such a combination is to check the influence of closely positioned lenses on the transverse emittance. As in the setup of seven magnets without restrictions on the symmetry of the beam, the projected emittance for one of the planes increases while for the other it stays nearly constant. Such an evolution results in a quasi-periodic beam envelope for the corresponding plane, i.e. smaller envelope oscillations, while for the second no periodic solution is obtained. The calculated mismatch after tracking, including space charge for the plane with worse periodicity, is $\Delta\beta_y = 214\,\%$, thus, quadrupole correction, additional to the one TRACE-3D offers, has to be applied. Visually this can be determined from Fig. 5.32.
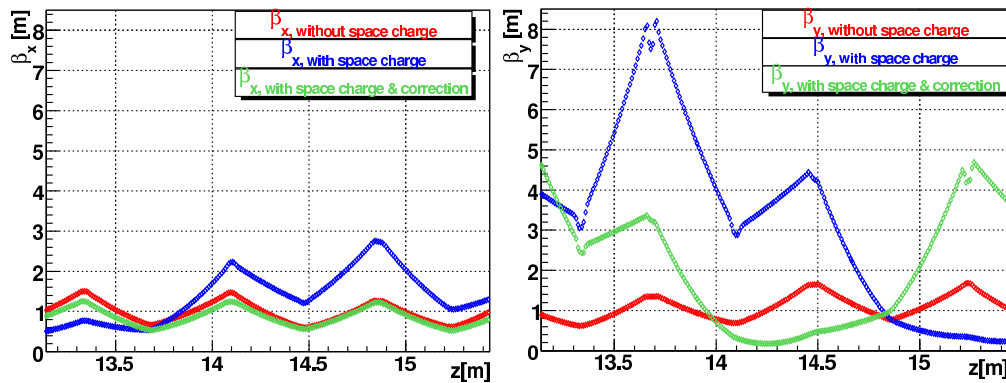

Figure 5.32: β_x (left) and β_y (right) along the tomography section using five matching quadrupoles with a long drift between the first two. TRACE-3D has been used for the matching. The bad periodicity for one of the transverse planes shows that the linear space charge calculations used by TRACE-3D are not sufficient for the small phase-space volume and high charge density PITZ characterizes.

5.4.2.4 Round beam

For the setups mentioned until now the beam has been allowed to be asymmetric in its transverse dimensions along the matching section. In such a case, as the beam is strongly focused in one of the planes, the phase space for that plane will be more diluted due to space-charge effects than for the other plane. To counteract such a behaviour, additional constraints are introduced in the matching procedure - namely, using intermediate points where the beam is required to be round or $\beta_x = \beta_y$. Those points are chosen to be at about the middle of long drifts where symmetricity is needed.

The first possible setup for which the requirement for a round beam can be set is using all the available nine quadrupole lenses. A linear MAD solution is shown in Fig. 5.33. A similar result has been obtained using TRACE-3D but the calculated mismatches after tracking with space-charge forces included are far beyond the acceptable - $\Delta\beta_x = 190\,\%$ and
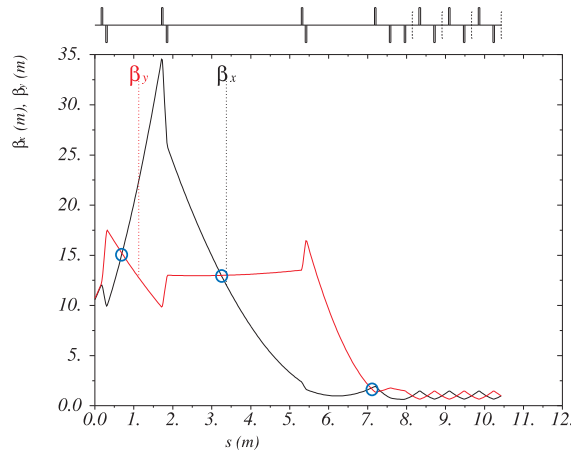
5.4. Modeling a tomographic experiment

Figure 5.33: β_x and β_y using all matching quadrupoles and constraints for a round beam. The blue circles represent the positions where the beam has been matched to be round. The longitudinal position is with respect to the first used quadrupole magnet physically located at about 5 m.

$\Delta\beta_y = 200\,\%$. Details of the Twiss β-functions on the screens are given in Table 5.6 and the envelope evolution along the tomography module can be seen in Fig. 5.34. Again the

Table 5.6: β-functions on screens with the condition of a round beam along the matching section and using all available matching quadrupole magnets. The beam transport is optimized towards periodic particles trajectories using MAD, afterward TRACE-3D and the validity is varified with the ASTRA numerical tracking.

	Design	**Scr.#1**	**Scr.#2**	**Scr.#3**	**Scr.#4**	$\Delta\beta$
$\beta_x\,[m]$	0.999	0.502	1.03	2.894	2.164	190 %
$\beta_y\,[m]$	0.999	1.952	2.975	1.179	0.445	200 %

conclusion is that a good matching of the beam envelope parameters to the optics of the lattice can be obtained only using a detailed particle tracking.

Excluding the first pair of quadrupoles along the beamline has proven to be possible to deliver a round beam and smaller mismatches if the momentum spread is minimized. Such a solution is the one shown in Fig. 5.23(b). No other matching except with MAD has been done. Consequently, in order to avoid the time consuming matching based on numerical tracking, one needs to optimize the beam parameters towards minimum momentum spread, i.e. to minimize possible longitudinal density modulations and average the effect of space charge over the bunch length.

Another possibility is to require a round beam with Twiss parameters as close as possible to those required on screens and the final correction to be done with a couple of additional quadrupoles. This is described in the next paragraph.
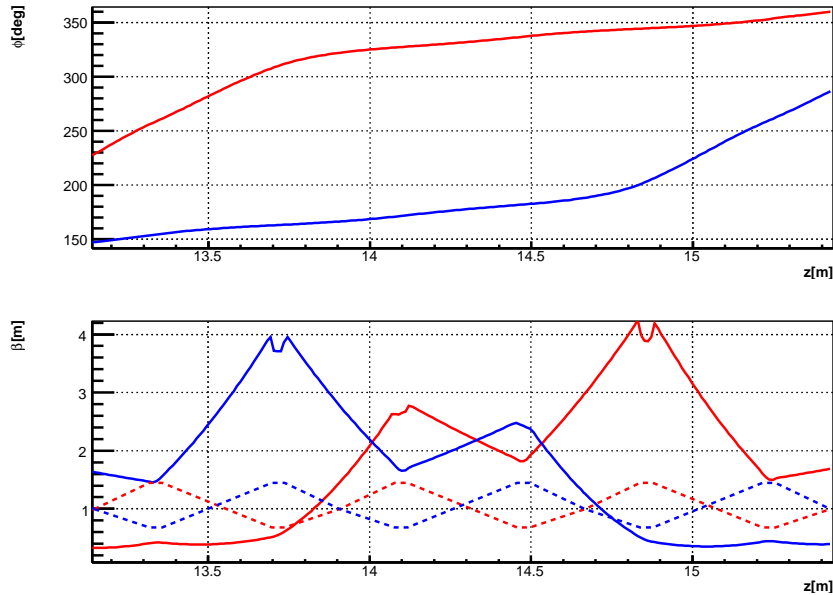
Figure 5.34: β_x and β_y MAD (dashed line) and ASTRA (solid line) using all nine matching quadrupoles and constraints for a round beam.

5.4.2.5   Using quadrupole triplets

With properly chosen gradients of the magnets in a quadrupole triplet, the electron beam can be focused simultaneously in both of the transverse planes. This case is purely hypothetical as there is no space to install triplets along the PITZ beamline. Using simulations it has been checked if a single triplet, whose first quadrupole is positioned at the same place as the first quadrupole in Fig. 5.26, can deliver the necessary focusing in front of the last three magnets ($z = 12.007$ m) from the matching section. The first and the third magnets from the triplet are the same as the ones inside the FODO lattice. For a beam with momentum close to the upper limit of the PITZ momentum range and normalized emittance close to 1 mm·mrad the required focusing directly at the entrance of the last three quadruples is not possible with the short effective length of the used magnets and the long drift behind. For that reason one additional triplet at $z = 10.327$ m has been inserted. A detailed ASTRA scan over the gradients of these two shows that the Twiss functions can be adjusted for a nearly round beam in front of the last three magnets in the matching section. The achieved values are as shown in Table 5.7. Since all four Twiss parameters are different from the design values for

Table 5.7: Twiss functions in front of the last three quadrupoles obtained using two triplets.

$\beta_x\,[m]$	$\beta_y\,[m]$	α_x	α_y
1.616	1.663	1.599	-1.390

45° phase advance, they still need to be adjusted and only three magnets are not sufficient. An additional quadrupole has been inserted in front of the first screen and, thus, all the

5.4. Modeling a tomographic experiment

FODO cells have been shifted by 0.37 m downstream. The beam has been matched with MAD and consequently numerically tracked using ASTRA with and without space charge. The resulting envelope evolution is shown in Fig. 5.35 for the case without and in Fig. 5.36
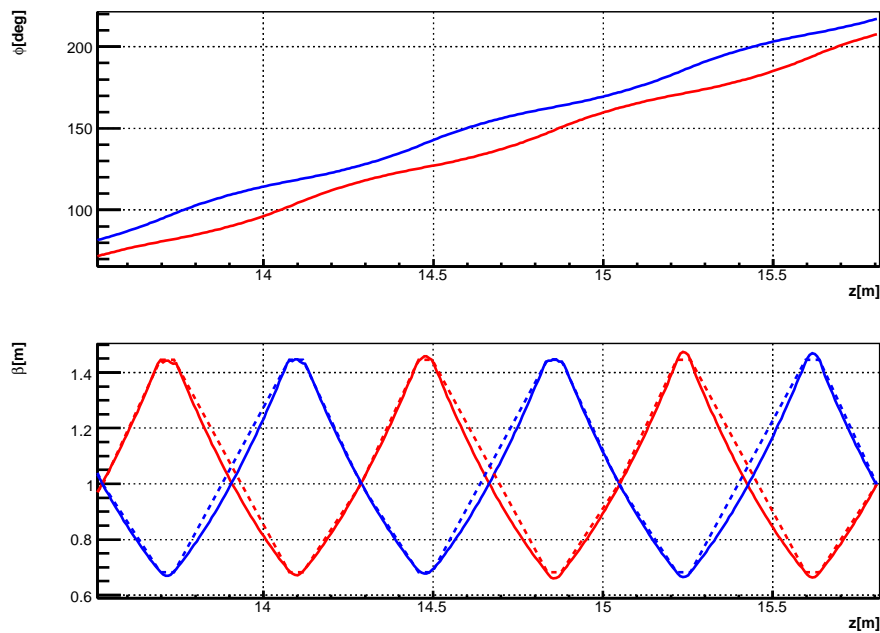

Figure 5.35: Phase advances and $\beta_{x,y}$ along the tomography section using two triplets and four quadrupoles. Tracking is done excluding space-charge forces.

with space-charge calculations. The unrealistic case - Fig. 5.35, is again periodic and also the
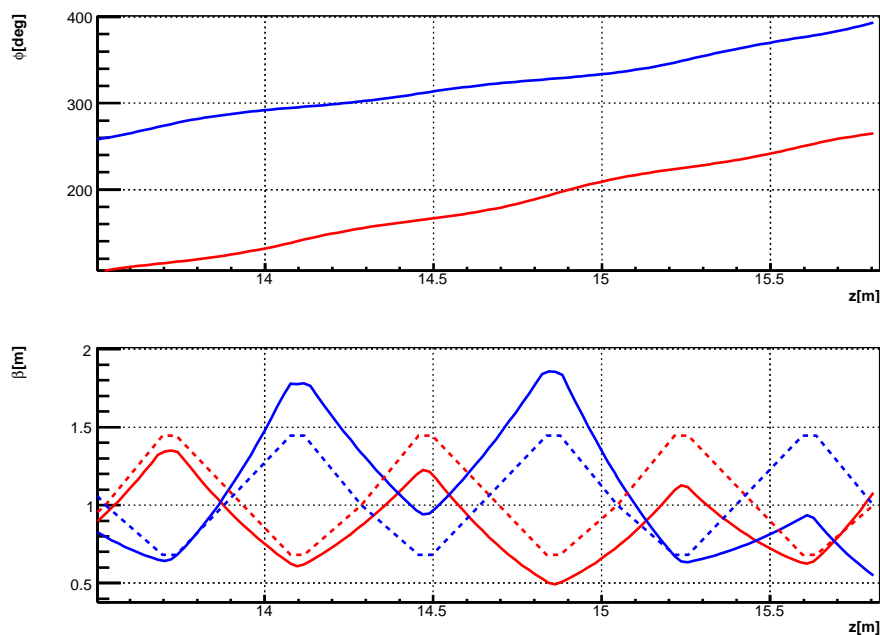

Figure 5.36: Phase advances and $\beta_{x,y}$ along the tomography section using two triplets and four quadrupoles. Tracking is done including space-charge forces.

realistic shows better periodicity than the case depicted for the same input beam parameters

and nominal matching setup of seven quadrupoles from Fig. 5.29. The resulting values of the β-function including space charge in the tracking are shown in Table 5.8. Quantatively the mismatches are $\Delta\beta_x = 27\%$, $\Delta\beta_y = 45\%$. In terms of phase advances the values between the screens are given in Table 5.9. The simulated arrangement of two triplets and four

Table 5.8: Twiss functions on screens using two quadrupole triplets and four single quadrupoles for matching. The graphical representation of the envelope is given in Fig. 5.36

	Design	Scr.#1	Scr.#2	Scr.#3	Scr.#4	$\Delta\beta$
$\beta_x\,[m]$	0.999	0.94	0.87	0.73	1.08	27 %
$\beta_y\,[m]$	0.999	0.799	1.34	1.18	0.55	45 %

Table 5.9: Phase advances between the screens using two triplets and four quadrupoles for matching. The values correspond to Fig. 5.36

	Design	#1 $\rightarrow$ #2	#2$\rightarrow$ #3	#3$\rightarrow$ #4
$\varphi_x\,[°]$	45	49	57.8	52.1
$\varphi_y\,[°]$	45	42.6	33.5	55.5

single quadrupoles delivers a result comparable to the one obtained with a nominal setup of seven separated magnets from Section 5.4.2.1. Practically the number of quadrupoles is increased by three for the sake of the longer beamline.

5.4.2.6 Matching for low bunch charges

The successful reconstruction for the two transverse planes requires a periodic solution for both of them simultaneously (see next section). It has been shown that, assuming high bunch charges, such a periodic solution is not easy to obtain using a non-periodic magnetic lattice for the range of beam momenta in which PITZ operates. These two conditions - high charge density and low photo-injector energies, is what makes the PITZ tomography module special. In order to check for operation parameters for which one can achieve a good matching, the charge has been decreased from 1 nC down to 20 pC varying also the beam energy. The matching setup used is the nominal one with seven quadrupole magnets. Fig. 5.37 shows results for 20 pC and 100 pC for a beam momentum of 19 MeV/c. The geometrical average of the normalized projected emittances for the two transverse planes for 20 pC is 0.098 mm·mrad and for 100 pC - 0.175 mm·mrad. Both cases correspond to optimized laser spot size so that the transverse emittance at the location of EMSY1 is minimized. The temporal laser profile is the same as for the ASTRA simulations at 1 nC - 20 ps FWHM and 2 ps rise and fall times. For the 20 pC case the initial laser spot size on the photo-cathode is 70 μm versus 150 μm for 100 pC - the charge density during photoemission is increased by a factor of about 0.1. The coupling between the transverse and longitudinal
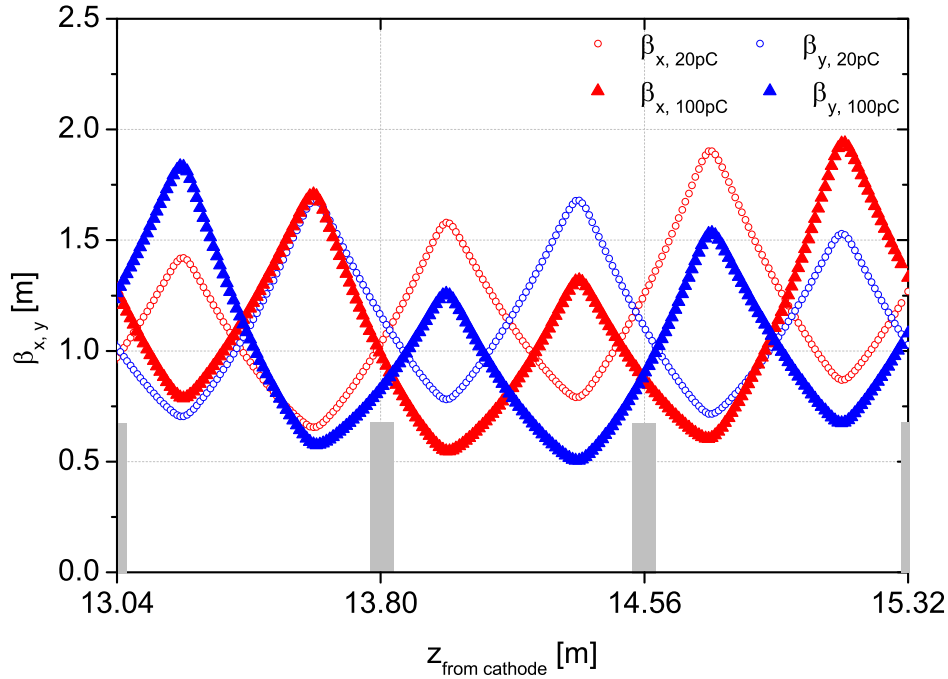
Figure 5.37: Twiss β-functions along the FODO lattice for a beam with momentum of 19 MeV/c, 20 pC with circles and 100 pC with triangles, geometrical average of the transverse emittances for the horizontal and the vertical planes at EMSY1 of 0.098 mm·mrad and 0.175 mm·mrad correspondingly for the 20 pC and the 100 pC case. The β-mismatch for the 20 pC case is 25 % for the horizontal plane where the periodicity is worse and 17 % for the vertical plane. For the 100 pC the mismatch is 50 % for both planes. The quadrupole strengths have been corrected additionally due to space-charge effects.

planes introduced due to space-charge forces lead to different mismatches in the two cases - 25 % for 20 pC bunch charge and 50 % for 100 pC. Additional correction on the strengths of the quadrupole magnets is applied. The practical conclusions one can draw are:

- the beam envelope matching depends on the charge density and the beam energy as prescribed by the generalized perveance

- each case of different beam parameters requires specific matching as a consequence of the previous point.

5.5 Reconstruction from numerical data

Chapter 4 introduced four reconstruction algorithms. The choice of which of them to be applied to experimental data depends on its performance with numerical data. Some of the matching solutions from the previous section 5.4.2 are used here with different reconstruction algorithms. All the examples use the same input distribution in front of the matching section. In the first case there are no space-charge forces acting on the beam. The second and the third example are realistic being different in the focusing strengths of the quadrupoles. An

identical matching setup is used in the three cases. The resulting distributions are compared with an original phantom ASTRA distribution in terms of the values defining the projected emittance.

5.5.1 Reconstruction from an ideal envelope transport

The first matching solution to start with is the one from Fig. 5.21 as it gives small mismatch even though the conditions within which the beam evolves are not realistic. Fig. 5.38 shows the phantom distribution and a number of reconstructions. The results are summarized in Table 5.10 only for the reconstructions which visually resemble the phantom.

Table 5.10: Relative errors between the phantom ASTRA distribution and its reconstructions with different algorithms.

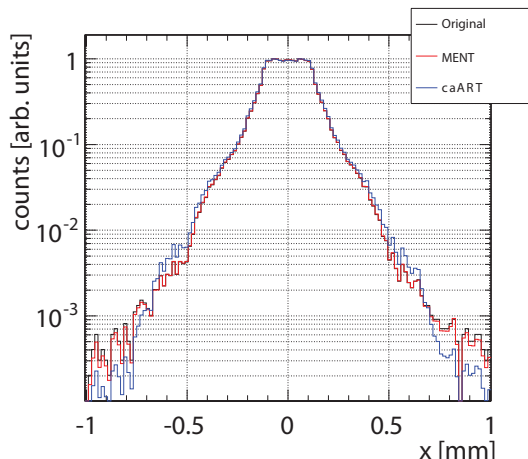| Algorithm	$\sigma_x \, [\%]$	$\sigma_{x'} \, [\%]$	$\sigma_{xx'} \, [\%]$
caART	0.199	0.4567	0.834
MENT	0.014	0.07	0.01

Figure 5.39: Normalized horizontal projections of the original distribution (black), reconstruction with MENT (red) and reconstruction with caART (blue) corresponding to Fig. 5.38(a), 5.38(d) and 5.38(e). MENT approximates better the density in the tails of the original distribution.

Visually there is some minor difference between the results obtained with BP and FBP but the result does not represent the original phantom. caART and MENT, on the other side, perform better also in terms of relative errors in the rms values of the resulting distributions. Considering the roughness of the contour lines in magenta, surrounding the core, it can be said that MENT shows better agreement in the density in the tails. This is also shown in Fig. 5.39 where the projections onto the horizontal axes of the original distribution and the reconstruction result with caART and MENT are given. The MENT result overlaps better the original distribution.
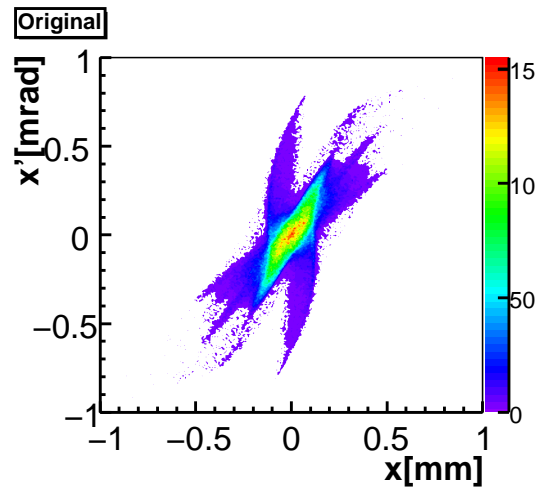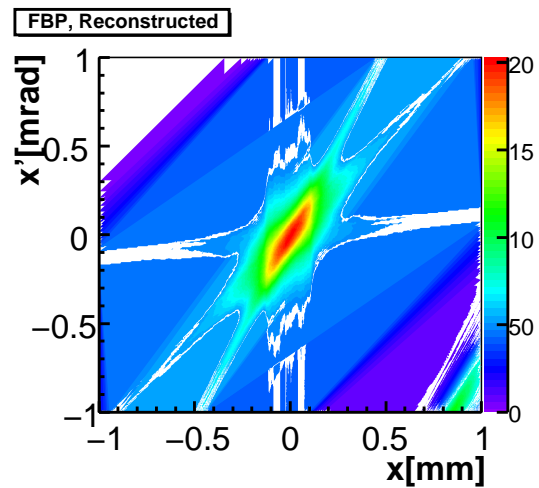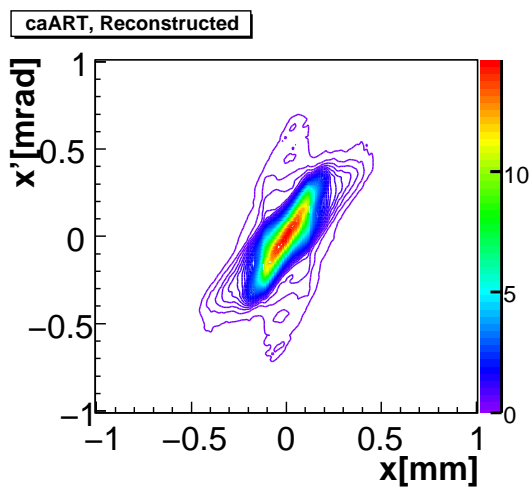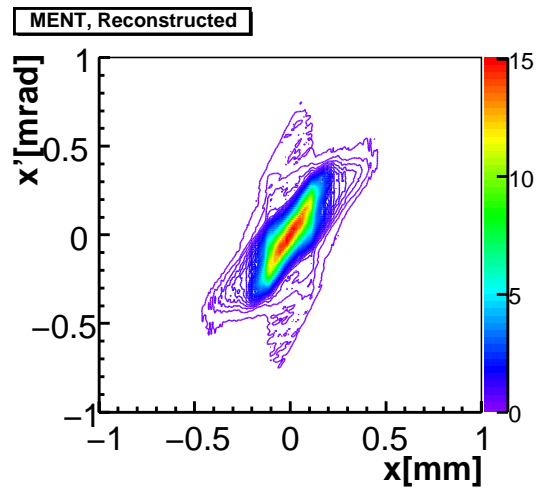
(a) Original phantom distribution.
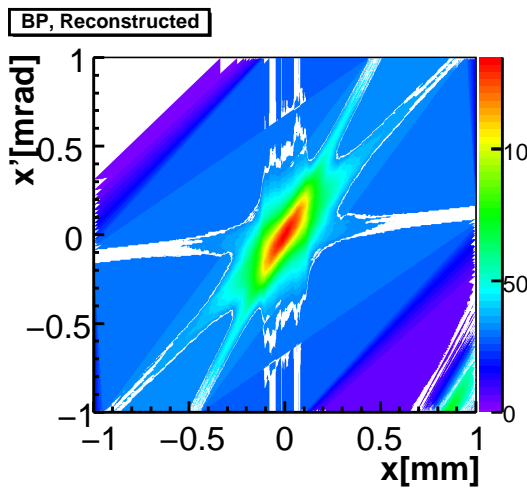
(b) BP result.

(c) FBP result.

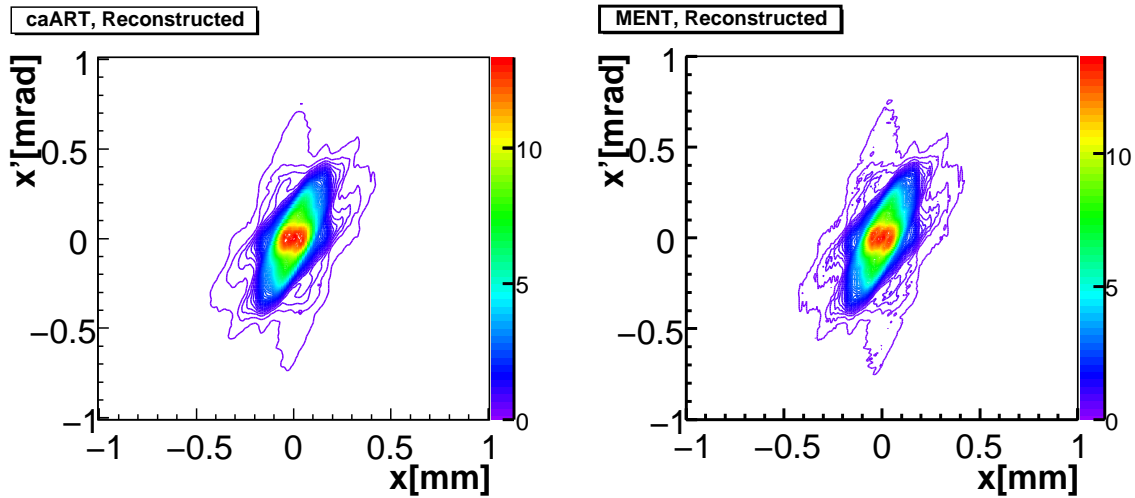(d) caART result.

(e) MENT result.

Figure 5.38: Phantom distribution and its reconstructions using BP, FBP, constrainted additive ART and MENT. The focusing along the FODO lattice corresponds to Fig. 5.21(a) and the numerical tracking excludes space-charge effects. The distributions are drawn as contour plots.

5.5.2 Reconstruction from numerical distributions tracked including the space-charge forces

In the next Fig. 5.40 only caART and MENT are shown. The distribution subject of reconstruction is the one given in Fig. 5.23(a) where the space-charge defocusing is taken into account in the numerical tracking. Both algorithms start to show artifacts especially visible at the beam core as MENT again shows higher density in the tails - Fig. 5.41.
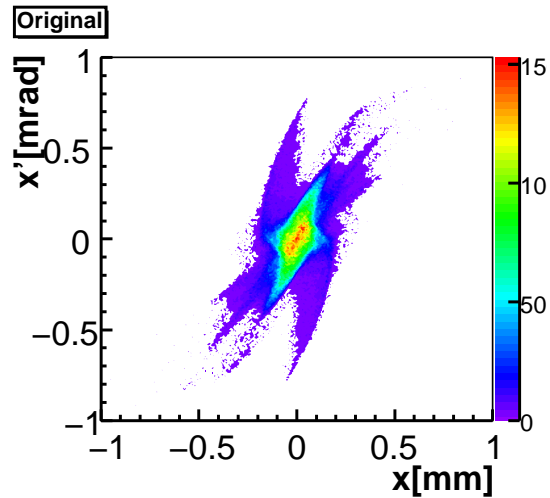
(a) Original phantom distribution.

(b) caART result.

(c) MENT result.

Figure 5.40: Phantom distribution and its reconstructions using caART and MENT, drawn as contour plots. The β-mismatches are 38 % and 29 % for the horizontal and the vertical planes shown in Fig. 5.23(a). Space-charge forces are included in the particle tracking. Clearly both algorithms show artifacts in the core of the beam.

The numerical estimation of the reconstructed elements of the beam sigma matrix is in Table 5.11. The values for MENT are 1-2 orders of magnitude higher than in the previous case of even better matching and zero-current beam.
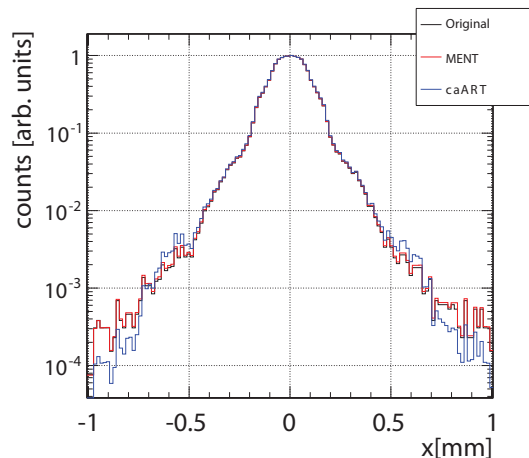
Figure 5.41: Normalized horizontal projections of the original distribution (black), reconstruction with MENT (red) and reconstruction with caART (blue) corresponding to Fig. 5.40(a), 5.40(b) and 5.40(c). As above in Fig.5.39, MENT again approximates better the density in the tails.

Table 5.11: Relative errors between a phantom distribution and its reconstructions shown in Fig. 5.40.

Algorithm	σ_x [%]	$\sigma_{x'}$ [%]	$\sigma_{xx'}$ [%]
caART	0.66	0.39	3.02
MENT	0.76	0.63	2.33

5.5.3 Reconstruction from a mismatched beam

The input projections of the next reconstruction are snapped from a badly matched beam - the β-mismatches for both of the transverse planes are 80 %. Its horizontal normalized phase space is given in Fig. 5.42 and the β-functions and the phase advances in Fig. 5.43. caART
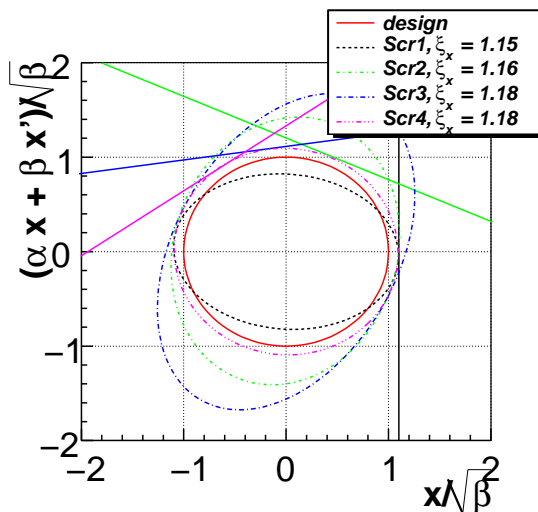

Figure 5.42: Normalized phase space with overlaid normalized rms ellipses from the four screens in the tomography module.
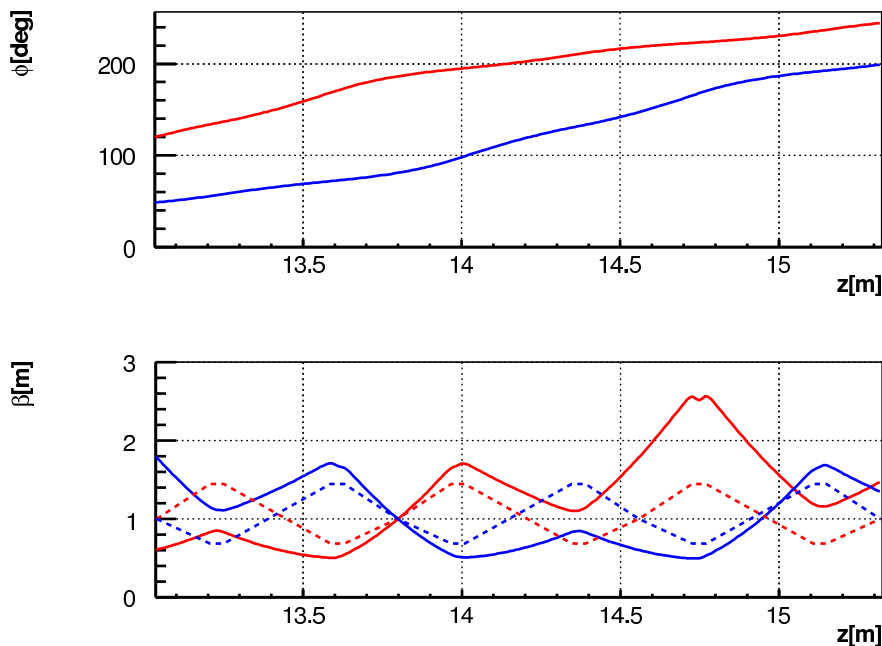
Figure 5.43: A badly matched beam along the FODO lattice is subject of this reconstruction. As before the dashed lines are a theoretical linear periodic trajectory of the beam envelope and the solid ones are the simulation data obtained with ASTRA.

and MENT performance for such a case is shown in Fig. 5.44. Table 5.12 summarizes the results of the last example. Clearly, the reconstruction artifacts in the case of badly matched

Table 5.12: Relative errors between the phantom ASTRA distribution and its reconstruction with different algorithms having non-equidistant angular steps of the rotation of the beam in the phase space.

Algorithm	σ_x [%]	$\sigma_{x'}$ [%]	$\sigma_{xx'}$ [%]
caART	0.73	0.062	7.92
MENT	0.58	0.121	7.97

beam for limited number of input projections increase with the degree of mismatch.

caART and MENT show a much better performance compared to the other two methods when applied to a limited number of projections. Besides, in the last two cases above - Fig. 5.40 and Fig. 5.44, the projections are not exactly equidistant since there is some mismatch of the beam envelope. Only for the unrealistic case of best matching, both algorithms show a single linear core of the reconstructed phase-space. For a bigger mismatch also the density in the tails is reconstructed worse.

5.5.4 Reconstructed charge density

An important issue for the reconstruction is the equivalent charge density in the resulting phase-space density distribution. To emphasize on the visual aspects, the above reconstruc-
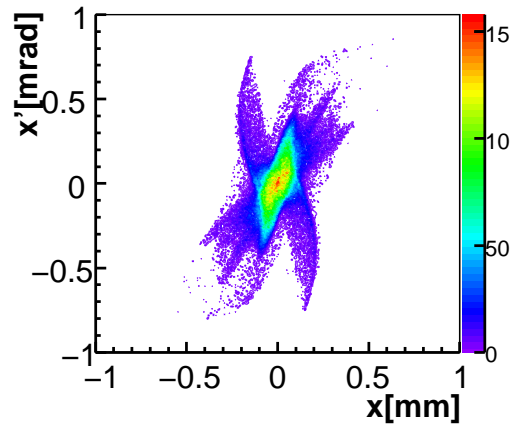
(a) Phantom distribution.
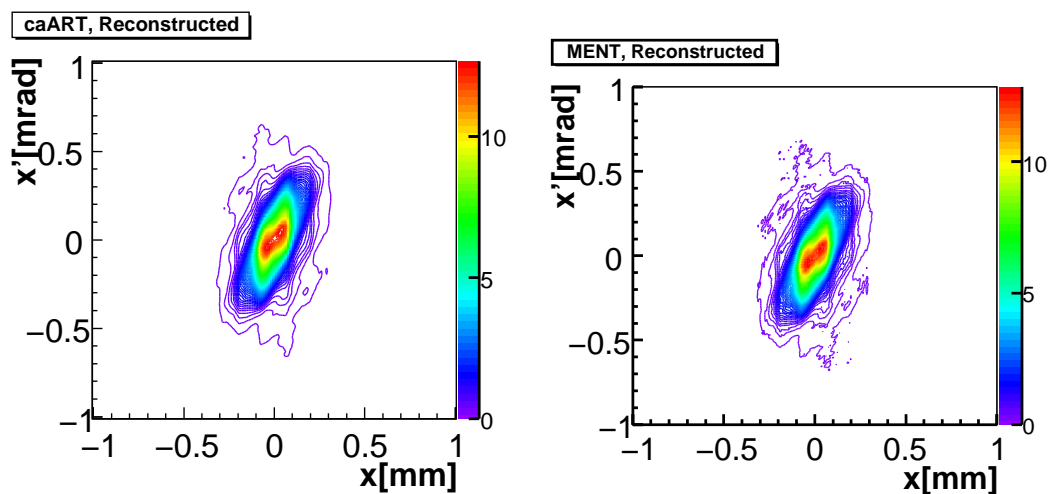
(b) caART result.

(c) MENT result.

Figure 5.44: Phantom distribution for an unmatched beam and its reconstruction using caART and MENT visualized with contour plots.

tion examples are shown in contour plots. In reality there is a low intensity rim whose level depends on the input number of projections. This rim encloses an area outside of which the probability to find a bin contributing to the object of reconstruction is zero. The effect of this rim for the exotic image from chapter 4 Fig. 4.2(a) is shown in Fig. 5.45 for 4 and 16 projections. The two distributions on the top are the same ones as shown in Fig. 4.6 and Fig. 4.8, previously drawn as contour plots. Comparing by columns, the weight in the rims for both MENT and ART decreases as more projections are used and therefore it can be treated as an artifact originating partially from the limited data. The question that needs to be answered then is what is the amount of charge such a rim represents.

Considering Fig. 5.38 and Fig. 5.40, the corresponding Tables 5.10 and 5.11 and Fig. 5.39 and Fig. 5.41, the MENT algorithm outperforms the ART and, therefore, it is advisable to utilize this algorithm for experimental data. In the studies to follow only MENT has been used and the results are shown in colour-code.

(a) caART result, 4 projections.

(b) MENT result, 4 projections.

(c) caART result, 16 projections.

(d) MENT result, 16 projections.
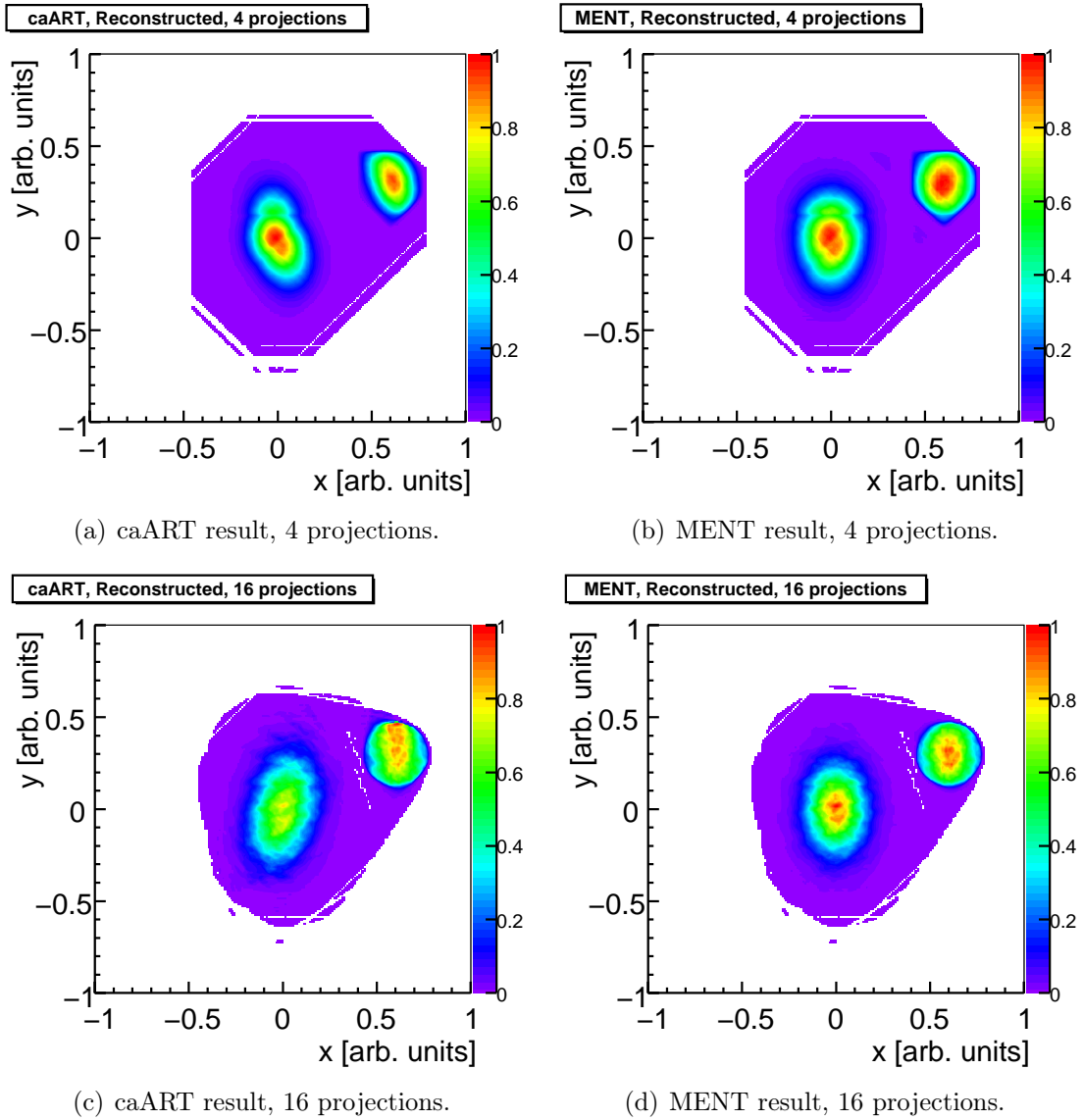
Figure 5.45: Colour-code visualisation of the reconstruction resulting from caART and MENT of the original image shown in Fig. 4.2(a). Projections from four (top) and 16 (bottom) equidistant rotations are used as input data.

A similar colour-code plot as introduced above is used to visualize the results from Fig. 5.40(c) as shown in Fig. 5.46(a). In order to estimate the weight of the artifact rim some small percentage $\hat{q}$ of the integrated intensity can be removed. This corresponds to an exclusion of some equivalent charge q contributing only to the tails of the density distribution if it would be real. For Fig. 5.46(b) only 0.1 % of the integrated intensity is removed. With the logic of the MENT algorithm this is equivalent to discarding the bins contributing with a probability less then 0.001 %. The calculated beam emittances from the original phantom, the uncut and the cut reconstructions are given in Table 5.13. The decrease in emittance is about 2 % with respect to the uncut distribution and, assuming this rim corresponds to charge, the equivalent charge it represents is 1 pC from the total charge of 1 nC represented in this simulation. It is evident that such a low-intensity cut does not lead to a significantly
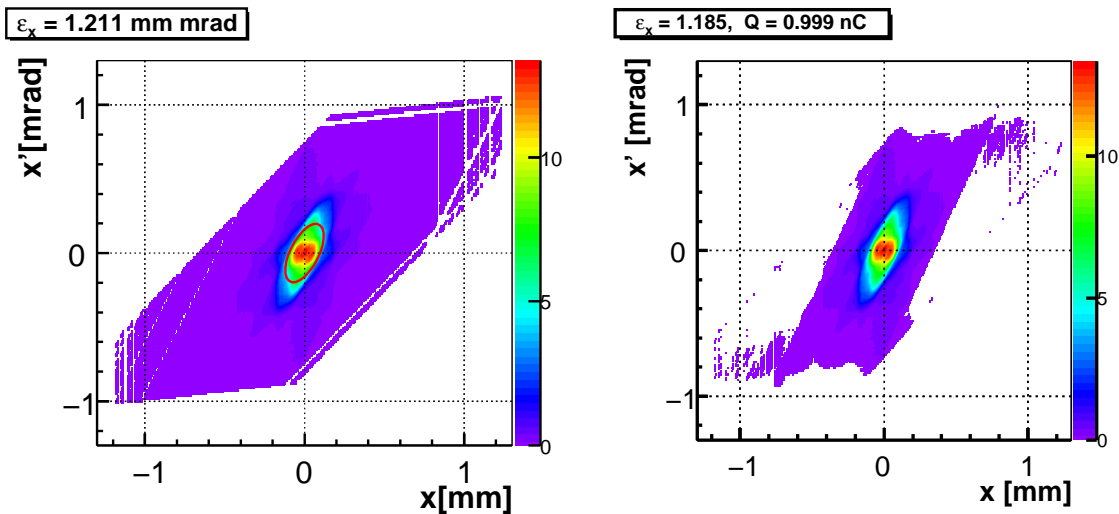
(a) Full range of the reconstruction result. The red ellipse at the center shows the equivalent RMS ellipse.

(b) 0.1 % of the overall intensity is excluded.

Figure 5.46: Colour-code visualisation of a reconstruction with MENT equivalent to the one shown in Fig. 5.40(c).

Table 5.13: Normalized emittance for the distribution in Fig.5.40(c), reconstruction without and with 0.1 % cut on the integrated intensity represented in Fig.5.46(a) and Fig.5.46(b).

| | Original ASTRA | Reconstructions | |
		without cut	0.1 % intensity cut
ε_x[mm·mrad]	1.17	1.211	1.185

underestimated emittance value.

In order to justify the quality of the reconstruction in terms of charge density distribution, one can take away the same amount of integrated intensity for both the original phantom and the uncut reconstruction result and evaluate the emittance for the remaining charge. The result of such a procedure emphasizes the beam dynamics aspect showing what amount of charge is contained within different contours around the beam core. The result applied on the uncut distribution from Fig. 5.46(a) and the original from Fig. 5.40(a) is shown in Fig. 5.47. The plot on the right side where the relative deviation is given shows that the biggest discrepancy originates close to the core of the beam which is also expected considering the double structure present in the reconstruction. A limited bin width in the region of the beam core is also a possible source of an increased difference between the original and the reconstruction. The second interesting point is the cut of 3 % where the emittance is underestimated by about 18 %. The reason here are the filamenting tails in the original distribution which are not correctly represented in the reconstruction result. Considering the fact that for the next cut of 4 % the relative difference decreases by half one can still rely on the reconstruction if the final emittance is calculated out of 95 % of the enclosed density.

(a) Emittance values.

(b) Relative difference between the emittances of the original and the reconstructed uncut distributions.
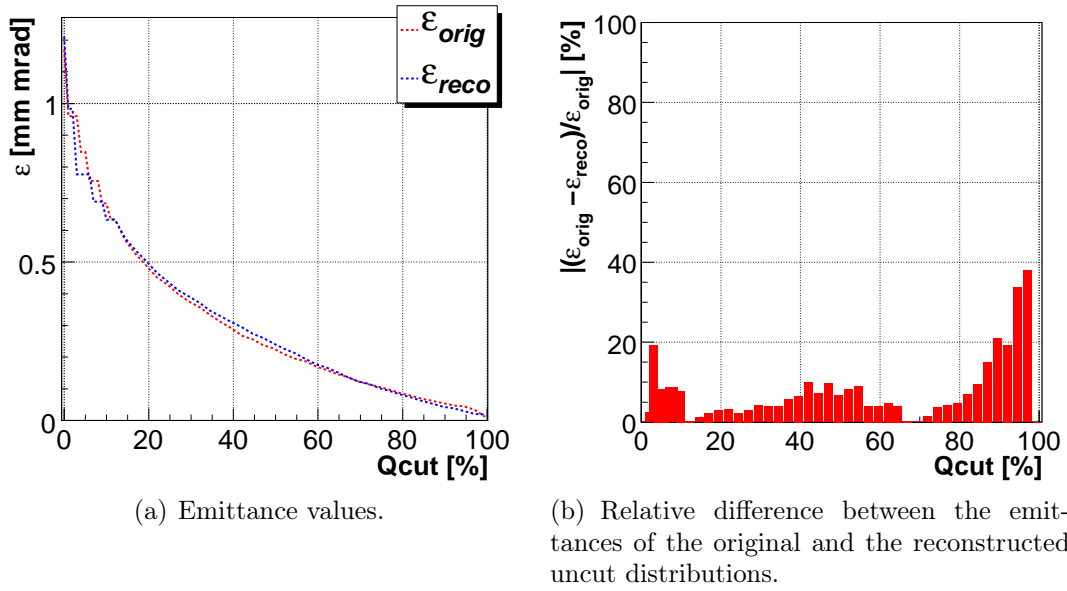
Figure 5.47: Emittance for the original and reconstructed distributions shown in Fig. 5.40(a) and Fig. 5.46(a) calculated as a function of equivalent charge excluded simultaneously from both distributions. The right hand side plot shows the relative difference between the two values.

Still, the question to justify such an intensity cut of 0.1 % should be answered for low bunch charges. This is done for the 20 pC bunch charge shown in Fig. 5.37 with blue and red circles for which the β-mismatch for the vertical plane is 17 %. The measurements of low charges are mostly affected by the resolution of the optical system. For the optics available along the tomography module the resolution of the lens with the higher magnification is estimated to be $\sigma_{\mathrm{resolution}} \simeq 15$ μm and this is taken into account for the results in Fig. 5.48.

The reconstruction overestimates the emittance by 12 % even when the above mentioned 0.1 % intensity is excluded - then the precise value is 10 % as seen in Fig. 5.49(a). The trend to overestimate the original emittance continues until about 65 % intensity cut and beyond 80 % the calculations reveal constant emittance from the reconstruction as demonstrated in Fig. 5.50. This is caused by the fact that the beam size and divergence are already calculated from a single pixel and therefore neither they change, nor the covariance.

A number of conclusions can be drawn from the reconstruction of low charge bunches. First, an intensity cut up to 0.1 % of the integrated intensity from the reconstruction can be done safely since the remaining equivalent charge represents the emittance of the uncut distribution correctly. A second conclusion is that such low charges require much better matching. Here the β-mismatch is 17 % and the density distribution calculated having about twice bigger mismatch for 1 nC charge resulted in a smaller overestimation of the emittance which was shown in Fig. 5.47(a). The third conclusion is related to the resolution of the optical system which needs to be improved. The installation of an additional lens providing twice better magnification has aleady been proposed. The expected improvement in the smoothness of the reconstruction result is demonstrated in Fig. 5.49(b) as compared

5.5. Reconstruction from numerical data

(a) Original phantom distribution.

(b) Reconstruction result.
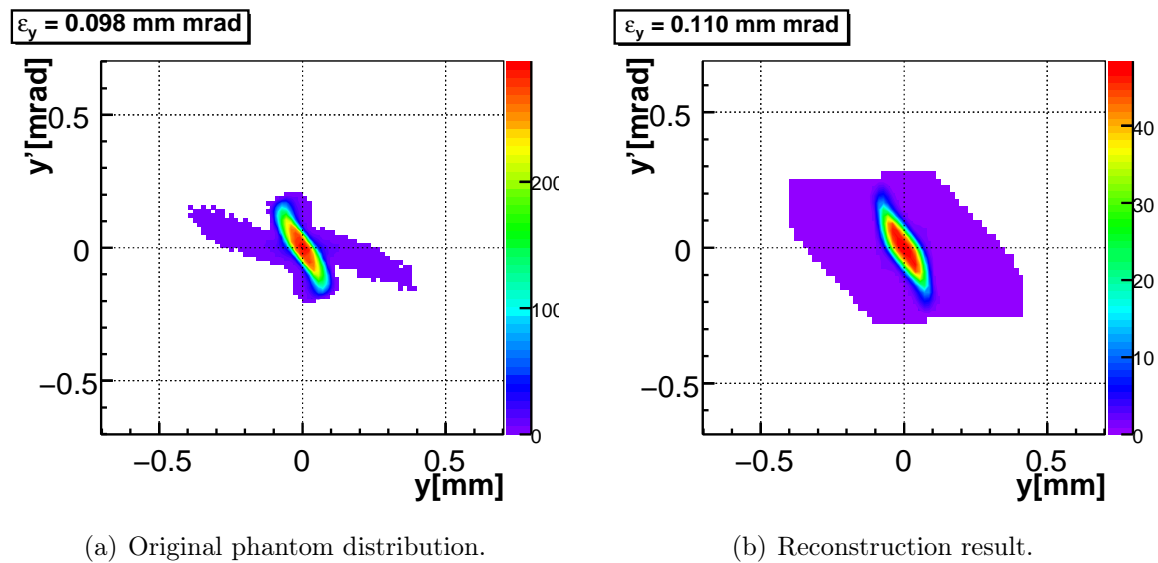
Figure 5.48: Underlying original distribution and the reconstruction result for 20 pC bunch charge, 19 MeV/c beam momentum and normalized transverse emittance of 0.098 mm·mrad. The bin width of the input projection data used for the reconstruction, as well as for the representation of the original distribution, is adjusted to correspond to the resolution of the lens that is used in the experimental measurements.

(a) The binning of the projections is defined with respect to the available optical resolution.

(b) The input projection data assumes twice better resolution of the optical system.
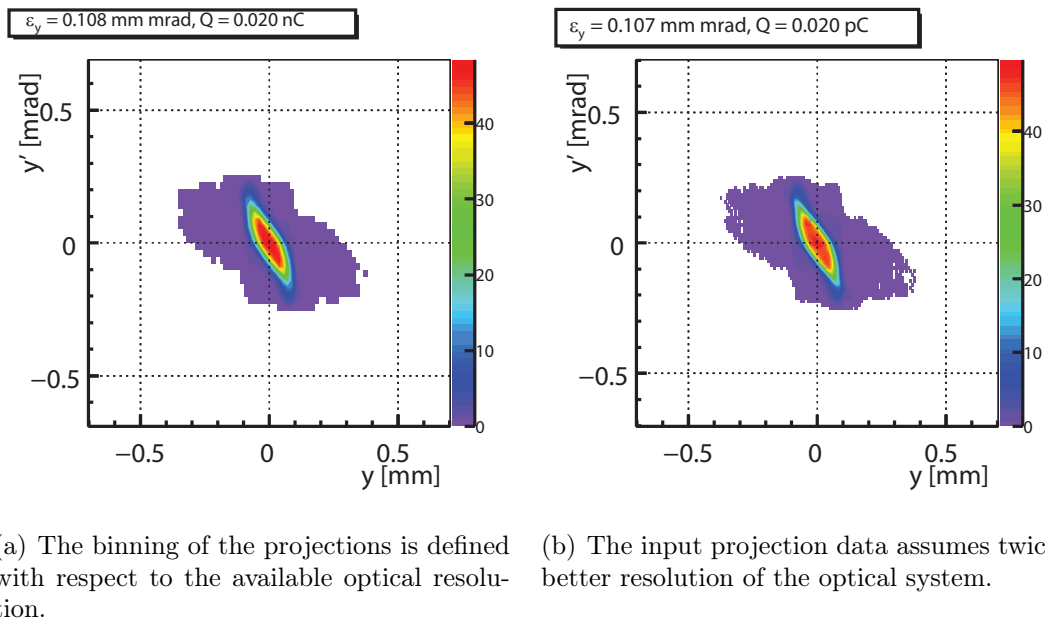
Figure 5.49: Resulting phase-space density distributions as 0.1 % of the total intensity is discarded.

to Fig. 5.49(a). The above mentioned 0.1 % intensity cut is applied. The improvement would also result in a better accuracy in the reconstruction of tails if such are present. The emittance almost does not change which proves that the algorithm converged to a solution where all the discrete bins have equal probability to be consistent with the given input projections.

(a) Emittance values.

(b) Relative difference between the emittances of the original and the reconstructed distributions.

Figure 5.50: Emittance and relative emittance deviation for the original and reconstructed distributions shown in Fig. 5.48(a) and Fig. 5.48(b) calculated as a function of equivalent charge excluded simultaneously from both distributions. The resolution of the unredlying distribution is limited as discussed in the text.

Conclusions

This chapter described the issues considered to reach the first goal of the thesis. The following topics were presented:

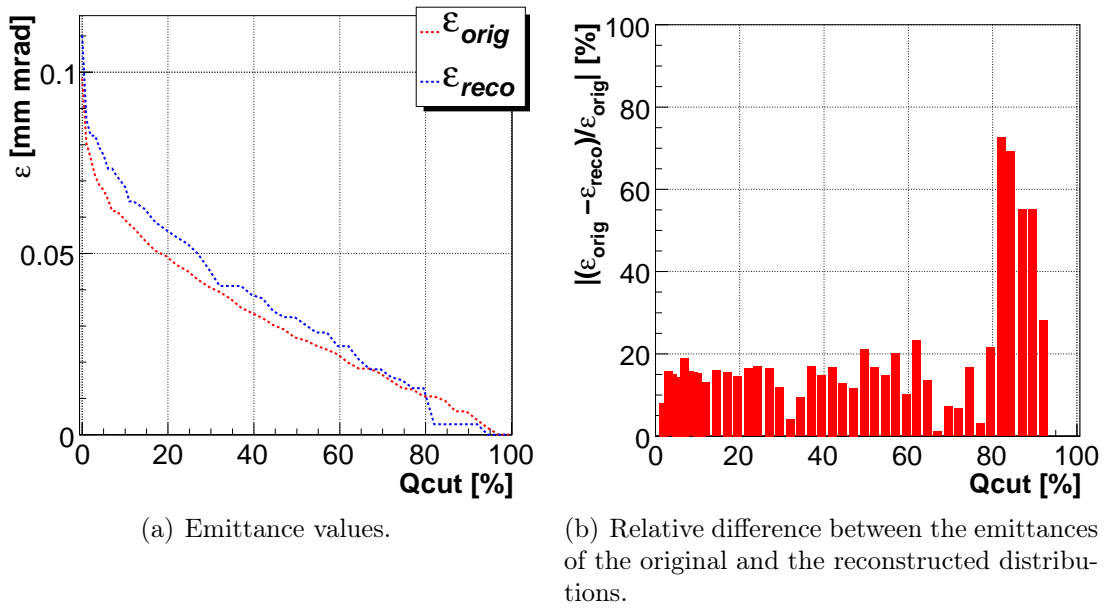1. the design of the tomography module - it contains three FODO cells and additionally there is an identical cell upstream the first screen as part of the matching section; the matching section can include up to nine quadrupole magnets;

2. a phase advance between the screens was chosen to be $\pi/4$ as the choice was made on the basis of sources of systematic uncertainties and on the tomographic requirements for equidistant angular spacing between the projections;

3. Monte Carlo simulations have shown that neglecting the influence of the space-charge forces results in underestimation of the calculated emittance; therefore one needs to bring the beam to an emittance dominated regime along the FODO lattice which was considered in chapter 3;

4. with numerical particle tracking it was shown that the space charge has to be taken into account but its influence can be controlled;

5. the prefered setup of matching quadrupoles consists of seven magnets - all but the first two along the beamline; if one allows a strong mismatch, the phase advance between the screens is no longer optimal and, consequently, artifacts are to be expected in the reconstruction results;

6. comparing reconstruction results from ART and MENT on numerically tracked macroparticle distributions it was concluded that MENT delivers better agreement in the reconstructed charge density; the biggest discrepancy in the reconstructed charge density originates from strong tails and around the core of the beam; to a great extend this can be improved with a properly designed optical system;

7. some rims in the halo part of the reconstruction result are always present and their weight can be decreases with more input data; these rims can safely be taken away with only 0.1% cut on the integrated intensity; it was shown that this can also be done for bunches with low charges.

Chapter 6

Measurements with phase-space tomographic reconstruction

The PITZ tomography module is operational since November 2010. Together with it the matching section and new gun and booster cavities were installed. Additionally a 10 MW in-vacuum directional coupler was installed in the waveguide feeding the gun giving the possibility to measure the RF power and to regulate the RF phase with better precision. The phase stability was improved to $1.5°$ peak-to-peak as compared to the $10\text{-}15°$ in the previous run in year 2009 [99]. The gun was conditioned with maximal peak power of about 6.25 MW and pulse duration up to 700 μs [23]. The first step in the characterization of the gun was to prove the results obtained in the year 2009 with the same accelerating gradient [100].

The new booster cavity provides the possibility to apply a stronger accelerating field than it was previously used. Currently the booster is capable to run with a maximum gradient of 21 MV/m with which a final beam momentum of about 25 MeV/c can be reached, compared to the maximum beam momentum of about 15 MeV/c until 2009.

The characterization of the RF guns operated at PITZ is based on measurements of the transverse emittance directly at the injector exit, i.e. just after the booster cavity, using the single slit-scan technique. The emittance is measured as a function of the field in the main solenoid for various transverse laser spot sizes, gun and booster RF phases and different bunch charges. The temporal laser profile varies slightly around 22 ps FWHM with 2 ps rise and fall times. The tomographic measurements were done for a part of those settings with the purpose to examine the functionality of the setup and to follow the evolution of the transverse phase space downstream the beamline. Priority was given to the 1 nC bunch charge as a nominal charge value used at PITZ. The set of parameters for which tomographic measurements were done is summarized in Table 6.1 [1].

The single-slit scan technique provides a direct measure of one of the transverse phase spaces but, in order to reach good data quality, the signal from a number of micropulses is

---

[1]Phase of 0 deg is used to denote the phase of maximum mean momentum gain.

Table 6.1: Photo-injector parameters used for tomographic measurements.

Gun cavity	Maximum gradient at the cathode	60	MV/m
	RF phase ϕ_g	0^1	deg
Booster cavity	Maximum gradient	21	MV/m
	RF phase ϕ_b	0^1	deg
Laser	Transverse rms spot size σ_{ini}	0.125-0.485	mm
	Longitudinal profile FWHM	22	ps
	Longitudinal profile rise/fall times	2	ps
Electron beam	Mean momentum after the gun	6.6	MeV/c
	Mean momentum after the booster	24.6-25.2	MeV/c
	Bunch charge	0.1-1	nC

integrated. Additionally, such a slit scan is a multishot measurement since moving the slit over the entire beam cross-section takes longer time during which many pulse trains are emitted from the cathode. Due to beam instabilities this procedure can cause inconsistent data sets. An updated measurement procedure drives the slit across the bunch in a continuous manner with which effects like laser position jitter and beam jitter are minimised. Nevetheless, measurements of one micropulse are important and the tomography module gives the possibility for such. Most of the data presented here utilizes imaging of a single bunch in the pulse train, i.e. the linac accelerates trains with one bunch. Exception is the case for 100 pC where 2 bunches were necessary. For statistical purposes 20 beam images were taken from a screen and the image by image analysis from each screen is used to evaluate the statistical fluctuations. The systematic uncertainty includes:

- 1% quadrupole calibration errors, including stability of the power supplies which was measured to be about 3.5×10^{-4} A [101].

- 2% error in the measured beam momentum.

- 2% uncertainty in the calibration of the optical system.

In a non-linear reconstruction procedure it is not possible to take into account the uncertainty due to the mismatch of the beam phase space.

This chapter presents the measurements done with the tomography module. Two consecutive measurements are used to cross-check the validity of the result as compared to results obtained from single slit scans at locations around the tomography section. In the presented reconstruction results the emittance is calculated as 0.1% of the integrated intensity is excluded since earlier in Chapter 5.5.4 it was demonstrated that this does not lead to a significant underestimation of the tails contributing to the density distribution. The charge calculated as 99.9% of the integrated intensity from the uncut distribution is given in the

header of the plot. Additionally the emittance of 90% of the integrated intensity is given to show the contribution of the tails. The graphical representation of the density distribution is done using the average of the 20 images for each of the four projections.

6.1   Details on the measurement procedure

The general procedure for a measurement of the transverse phase space with tomographic reconstruction using a FODO structure is as follows:

1. Preparation of the machine including:

    (a) defining the transverse and temporal properties of the photo-cathode laser.

    (b) defining the phase of the RF in the gun with respect to the phase of the laser for the necessary bunch charge.

    (c) defining the phase of the booster.

    (d) steering of the beam so that the charge is transported to the end of the beamline without losses and through the centers of all quadrupole magnets that will be used. The precise alignment of the quadrupoles and the screens guarantees that the beam is located at about the center of a screen if it is aligned through the previous pair of magnets whose currents are changed during setting up the tomographic measurement.

2. Adjustment of the currents in the quadrupoles along the FODO lattice with respect to their design strengths and the beam mean momentum. These quadrupoles should deliver the necessary rotations of the electron beam in the transverse phase space.

3. Matching of the electron beam - adjust the parameters of the beam in front of the FODO lattice so that the Twiss parameters on the first screen correspond to the ones with which phase advance of $45°$ along the lattice can be achieved.

4. Performing the screen measurement, i.e. projecting the six-dimensional phase space $\rho(x, x', y, y', z, p_z)$ onto a two-dimensional (x, y) by means of observation screens.

5. Projecting a spatial (x, y) distribution onto the axis defining the plane of the reconstruction.

6. Providing the projection data, prepared as described in Appendix C, and transport matrices, run the reconstruction algorithm.

Having the result of the reconstruction one is able to visualize the beam envelope oscillations along the FODO lattice - a plot like the one shown in Fig. 5.21(a). Such a visualization offers the possibility to verify the validity of the matching and, if necessary, to improve it.

For the measurement presented here the initial matching was done using MAD and the quadrupole setup corresponds to the nominal one described in Section 5.4.2.1. The position of reconstruction is the first screen along the FODO structure marked with 1$^{\text{st}}$ in Fig. 5.1(a). Prior to the tomographic measurement the two transverse phase spaces were measured for a fixed current in the main solenoid at the position of EMSY1. From those measurements one can obtain the initial beam Twiss parameters needed for the matching. Usually the first guess from MAD does not deliver a matched solution because the space-charge forces are not taken into account. Using another code leads to similar results as this was shown in Chapter 5.4.2 since in all cases the modeled space-charge forces are only linear and, thus, the beam emittance does not increase. But on the contrary, the emittance at PITZ is still not conserved and the matching has to be optimised with respect to that.

A particular difficulty during the measurements originated from the shape of the electron beam in this run period. The symmetricity of the transverse profile is broken along the linac as satellites develop in the horizontal plane. They become better pronounced downstream the beamline as this can be seen in Fig. 6.1 where the beam transverse distributions are measured at the locations of the first and the third emittance measurement systems. The blue solid line shows the evolution of the beam rms size from a simulated measurement for adapted machine parameters. Measured (top) and simulated (bottom) spots are also shown. A possible explanation for the shape of the transverse profile is an observed half-quadrupole effect from the main solenoid wherefrom the two transverse planes are differently focused at the entrance of the booster cavity and consequently the RF focusing from the booster has unequal effects - the transverse momentum vector components are affected differently.

6.2 Measurements with bunch charge of 1 nC

The transverse emittance for a bunch charge of 1 nC was measured as a function of the initial transverse laser spot size on the photo-cathode and of the field of the main solenoid. The scan of the laser spot size had a two-fold purpose. On one side it was intended to determine if the difficulties related to the matching of the envelope parameters are reduced for bigger beam sizes and correspondingly smaller space-charge densities. The second reason was to follow the dependence of the emittance on the laser transverse size.

6.2.1 Emittance evolution along the beamline

To confirm the validity of the tomographic measurements, the transverse emittance was measured at three locations along the beamline - EMSY1 (z = 5.74 m), on the first screen of the tomography module (z = 13.038 m) and on EMSY3 (z = 16.303 m) for fixed laser spot size. The chosen solenoid currents correspond to the one for which minimum emittance on EMSY1 has been found denoted with $I_{\varepsilon_{min}}$ further in this section, and additionally ($I_{\varepsilon_{min}} + 1\ A$) in order to confirm the first point. The phases of the gun and the booster cavities were set
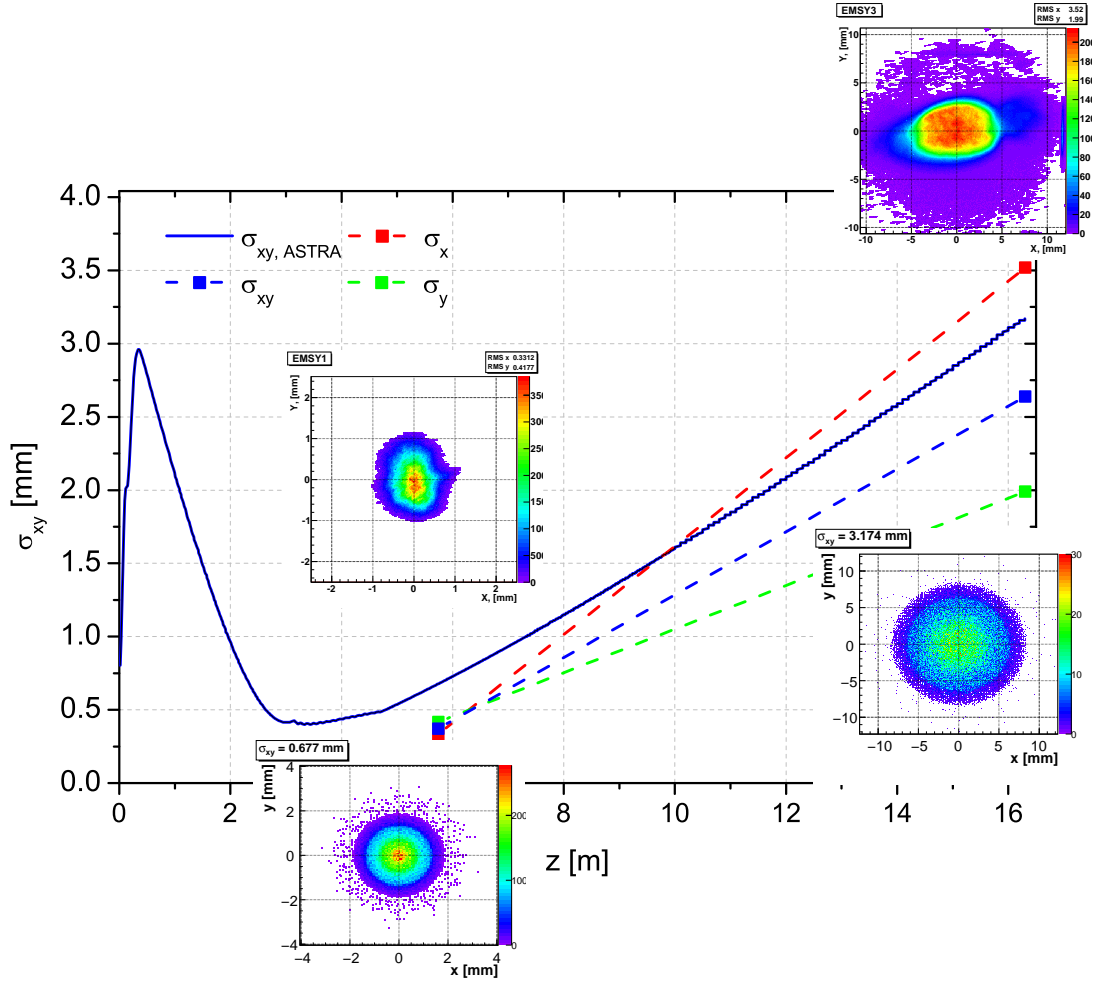
Figure 6.1: Simulated (solid) and measured (dashed) beam size along the beamline. The asymmetry of the measured transverse distributions becomes stronger pronounced as the beam propagates downstream whereas the simulation shows an aspect ratio of one. The measured beam profiles are shown on the upper side and the simulated at the bottom. The first measured profiles were taken at the EMSY1, z = 5.74 m from the cathode, the second at EMSY3, z = 16.303 m, as quadrupoles were not used.

to obtain maximum mean momentum. The laser spot size was set to 0.4 mm which does not correspond to the one delivering minimum emittance at the injector exit [102]. This bigger spot size was chosen in order to minimize the difficulties imposed by the space-charge influence during the matching.

Fig.6.2(a), Fig.6.2(b), Fig.6.2(c) and Fig.6.2(d) show the measured and simulated emittances. The EMSY1 data set consists of 10 consecutive slit scans for both planes from which a statistical deviation is calculated as the resulting error bar is smaller than the marker. For consistensy with the EMSY1 data the error bars on the tomographic reconstruction include only the statistical error over the 20 beam images taken from each screen. For EMSY3 no statistics is available as well as for EMSY1 at $(I_{\varepsilon_{min}} + 1 \; A)$. The emittance for the vertical plane calculated at the position of EMSY3 does not include the full beam distribution due to technical problems with the slit during the run period and the emittance is underestimated. A feasible measure of the error was not possible. Despite that the values are not completely
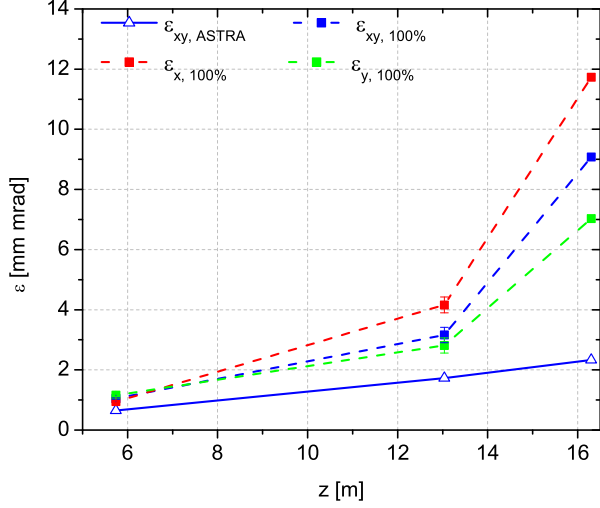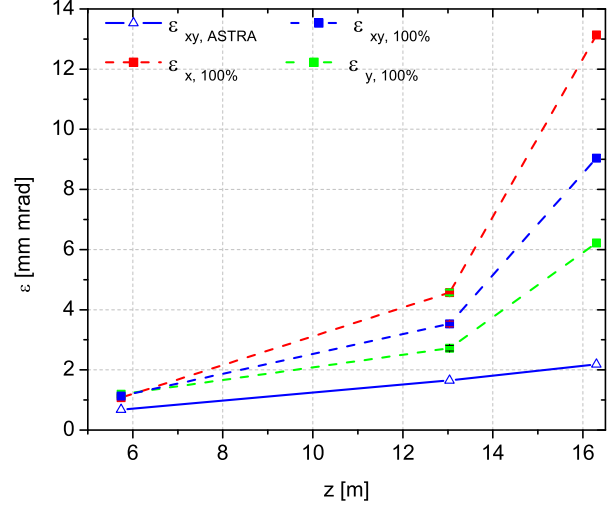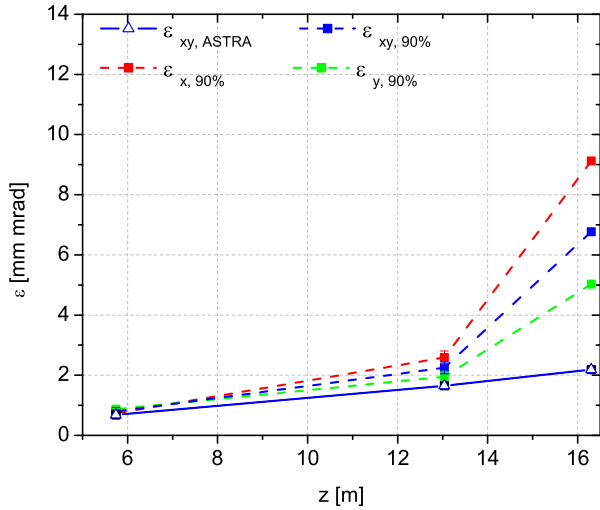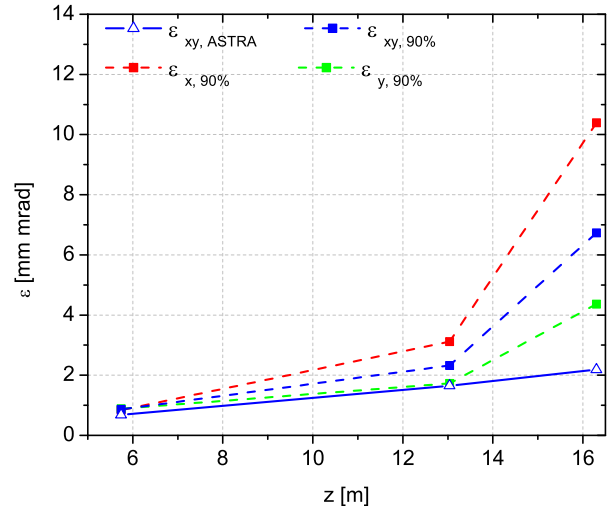
(a) Emittance evolution for $I_{\varepsilon_{min}}$.

(b) Emittance evolution for $(I_{\varepsilon_{min}} + 1A)$.

(c) Evolution of the 90% emittance for $I_{\varepsilon_{min}}$.

(d) Evolution of the 90% emittance for $(I_{\varepsilon_{min}} + 1A)$.

Figure 6.2: Measured (dashed) and simulated (solid curve) emittance evolution for $\sigma_{\text{ini}} = 0.4$ mm, $\phi_{\text{g}} = 0$ deg, $\phi_{\text{b}} = 0$ deg, final measured beam momentum 24.67 MeV/c and simulated 24.66 MeV/c. The EMSY3 measurement are done without active quadrupole magnets in front of the station. The emittance values calculated from the simulated ASTRA data take into account the full 100% distributions. The vertical emittance at EMSY3 is underestimated due to technical problems.

correct, they visualize the increase in emittance with a good approximation.

The disagreement between the measured and simulated values for 100% of the charge density increases with the distance from the cathode. A possible explanation is the discrepancy in the beam size originating from the nonsymmetricity depicted in Fig. 6.1. The corresponding phase-space distributions can be seen in Fig. 6.3 and Fig. 6.4 for $I_{\varepsilon_{min}}$ and $(I_{\varepsilon_{min}} + 1 A)$ correspondingly. The calculated mismatches are $\Delta\beta_{x,I_{\varepsilon_{min}}} \sim 60\%$, $\Delta\beta_{y,I_{\varepsilon_{min}}} \sim 10\%$ and
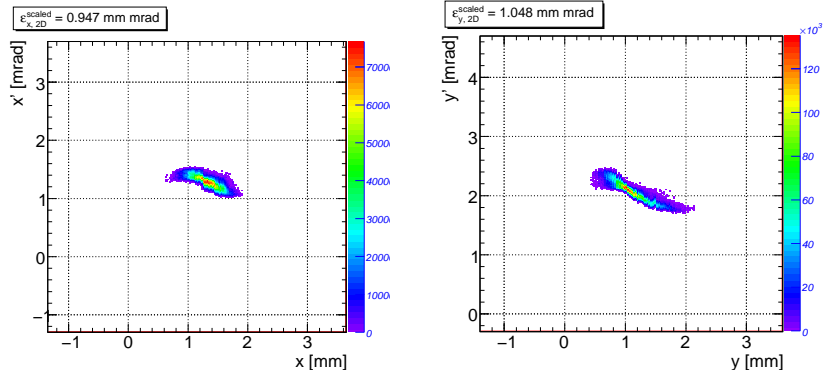
(a) Horizontal distribution on EMSY1.
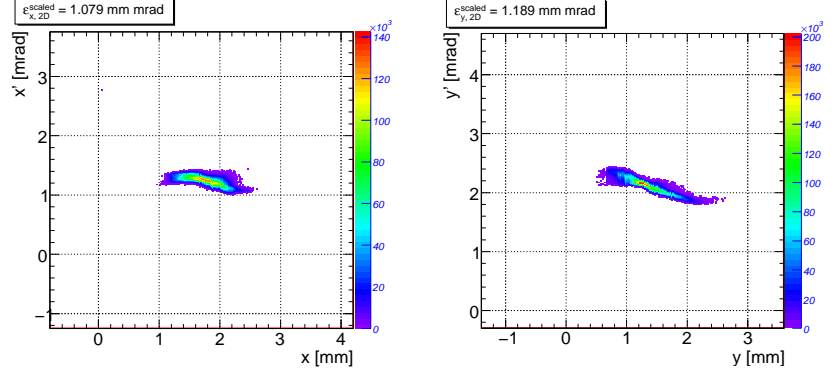
(b) Vertical distribution on EMSY1.
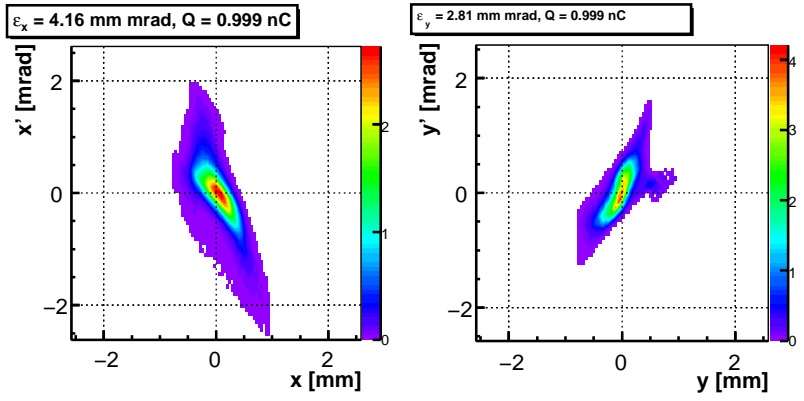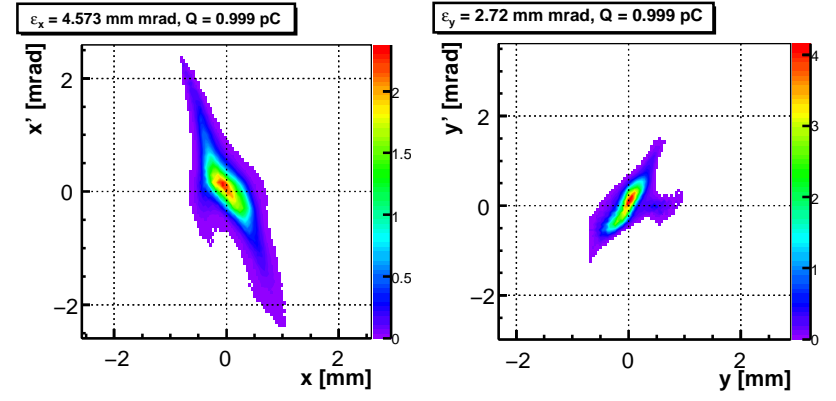
(c) Reconstruction of the horizontal plane from the tomography module.

(d) Reconstruction of the vertical plane from the tomography module.

Figure 6.3: Phase-space distributions on EMSY1 (top) and on the first screen of the tomography module (bottom) for a main solenoid current corresponding to minimum emittance at the location of EMSY1 $I_{\varepsilon_{min}}$. The horizontal axis of the phase space resulting from EMSY1 shows the position of the slit with respect to the beam position at the observation screen.

(a) Horizontal distribution on EMSY1.

(b) Vertical distribution on EMSY1.

(c) Reconstruction of the horizontal plane from the tomography module.

(d) Reconstruction of the vertical plane from the tomography module.

Figure 6.4: Phase-space distributions on EMSY1 (top) and on the first screen of the tomography module (bottom) for main solenoid current corresponding to $(I_{\varepsilon_{min}} + 1A)$. As above, the horizontal axis on EMSY1 data is with respect to the position of the beamlet on the observation screen.

$\Delta\beta_{x,y,(I_{\varepsilon_{min}}+1\ A)} \sim 20\%$ from the β-evolution along the tomography FODO lattice shown in Fig. 6.5. From those values it is expected that the reconstructions will be precise for the vertical plane of $I_{\varepsilon_{min}}$ and both planes of $(I_{\varepsilon_{min}} + 1\ A)$.

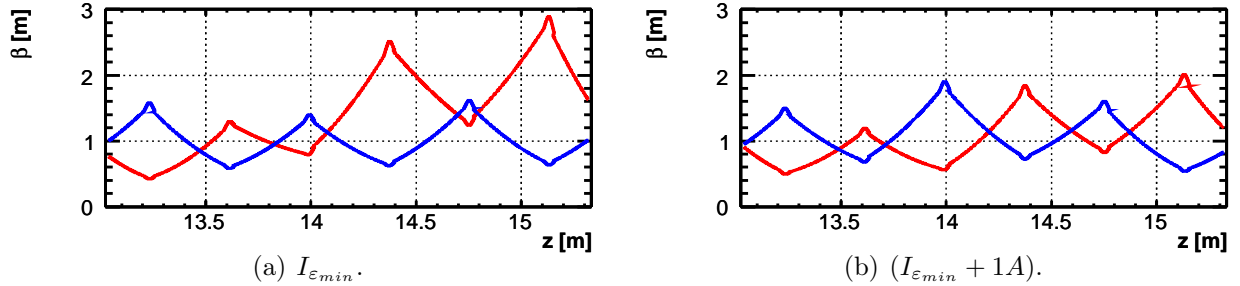(a) $I_{\varepsilon_{min}}$.   (b) $(I_{\varepsilon_{min}} + 1A)$.

Figure 6.5: β-functions along the FODO lattice for main solenoid currents corresponding to $I_{\varepsilon_{min}}$ (left) and $(I_{\varepsilon_{min}} + 1A)$ (right). Space-charge forces are not taken into account. The matching quadrupole are readjusted for each of the cases. The horizontal plane is given in red and the vertical in blue. The screens are located at 13.038, 13.798, 14.558 and 15.318 m.

The first noticeable point in the reconstructions is the mirrored orientation of the vertical plane with respect to the horizontal as this is mandatory according to Fig. 3.4 and Fig. 5.15 where it is shown that the two transverse planes on a screen along the tomography module should have opposite orientation - the Twiss α-functions have different signs for x and y.

The reconstructed vertical phase spaces for the two solenoid currents are very similar to each other showing the matching was successful in both cases even though the quadrupoles needed to be readjusted according to the different solenoid current. For the horizontal plane the covariance as well as the core of the beam are reconstructed with great similarities leading to the conclusion that the mismatch at $I_{\varepsilon_{min}}$ originates mostly from the tails of the distribution.

The horizontal EMSY1 measurement for $I_{\varepsilon_{min}}$ shows some small tails at $(1.55, 1.35)$ which are better pronounced in the tomographic reconstruction for the vertical plane - a micro-structure at about $(0.5, 0.1)$ in Fig.6.3(d) with an intensity at about 8% of the maximum beam intensity is cleary visible. Those tails develop further for the $(I_{\varepsilon_{min}} + 1A)$ as there the reconstruction reveals they are present in the two planes which is confirmed in the EMSY1 phase portraits at about $(2.2, 1.4)$ and $(2.2, 2.4)$ shown on Fig. 6.4(a) and Fig. 6.4(b) correspondingly. Fig.6.1 depicts the data for $(I_{\varepsilon_{min}} + 1A)$. It should be noted that the tails do not lead to bifurcation of the phase space but stay rather separated from the area with highest charge density. The particles constituting the structure have different β-functions and, therefore, they meet different quadrupole focusing and continue to stay separated from the main charge density. The satellite micro-structure is expected, having in mind the increased weight in terms of size and intensity of the satellites seen in Fig.6.1 as the electron beam propagates downstream.

The emittance was measured also at EMSY3 with the expectations from simulations that the value will be higher as compared to the one in the tomography section. As presented in

Fig. 6.2 the reconstruction result from the tomography module falls between the results from EMSY1 and EMSY3 for both transverse planes. The agreement in the phase-space density distributions and the calculated emittance values is a demonstration of the functionality of the tomography module for low energy and high charge density electron beams.

6.3 Reproducibility of the measurements

The reproducibility of the measurement was examined for a fixed solenoid current on two consecutive days with different gradients in the matching magnets. The chosen solenoid current of 393 A corresponds to the current for which minimum emittance on EMSY1 was found for the other specific injector parameters of those measurement days. The combination of initial laser spot on the cathode and solenoid current was chosen because together they presented the toughest matching at that period of time. While on the first day only the vertical plane was matched, on the second day the horizontal mismatch on the screens was somewhat decreased for the sake of a small decay in the periodicity for the vertical plane. This can be seen in Fig. 6.6 where the β-functions are shown along the FODO lattice. As the

(a) Measurement 1.

(b) Measurement 2.
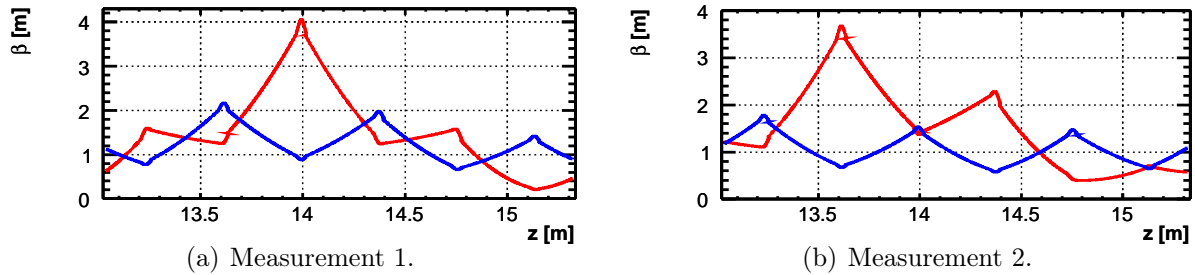
Figure 6.6: β-functions along the FODO lattice for different matching quadrupole gradients on two consecutive days. The red curve shows the horizontal plane, the blue the vertical.

horizontal mismatch $\Delta\beta_x$ was still rather high, here only the vertical planes are compared.

The conditions for which the measurements were done are summarized in Table 6.2.

Table 6.2: Parameters used for tomographic measurements in two consequent days.

	Measurement 1	Measurement 2	
Bunch charge	1	1	nC
Gun phase	0	0	deg
Momentum after the gun	6.66	6.68	MeV/c
Booster phase	0	0	deg
Momentum after the booster	24.66	25.21	MeV/c
Main solenoid current	393	393	A
Initial laser spot size	0.3	0.3	mm
Laser pulse rise time/FWHM\fall time	1.8/21.6\2.2	1.7/21.7\2	ps

The measured vertical phase-space distributions are shown in Fig.6.7. The orientations

(a) Phase space for measurement 1.

(b) Phase space for measurement 2.

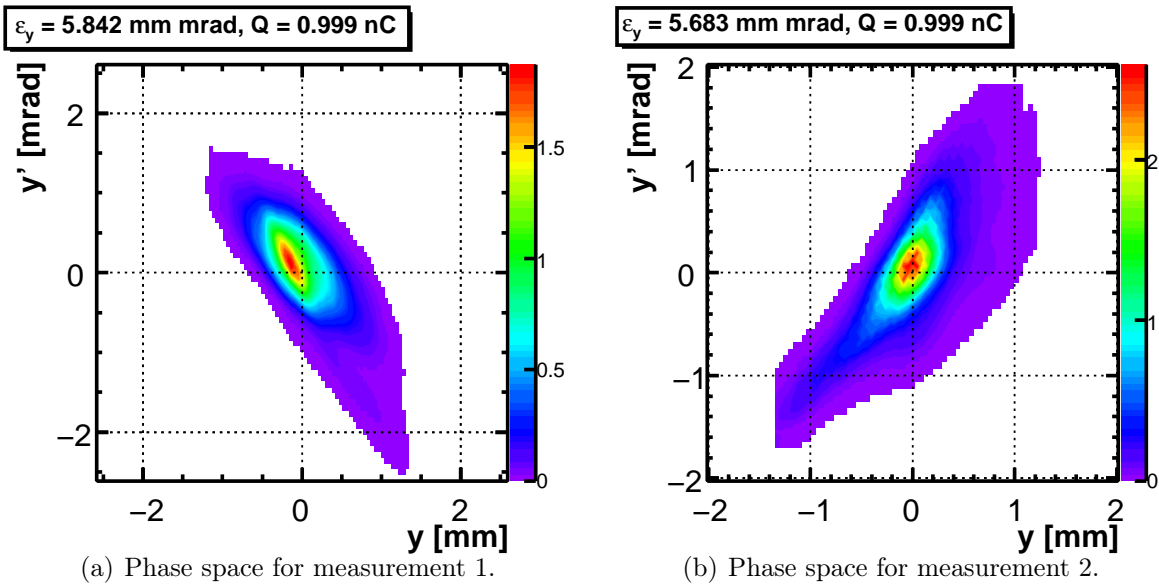Figure 6.7: Reconstruction of the vertical phase spaces on two consequent measurement days. Two different combinations of gradients in the matching quadrupole magnets are used wherefrom the distributions on the first screen in the tomography module are mirrored horizontally with respect to each other - in Measurement 1 the beam is convergent in the vertical plane and it is divergent in Measurement 2.

are different due to the fact that the matching quadrupoles vary in value and sign. Consequently the quadrupoles in the FODO structure have inverted polarity. The corresponding emittance values for 100% intensity and 90% intensity are summarized in Fig. 6.8. Even
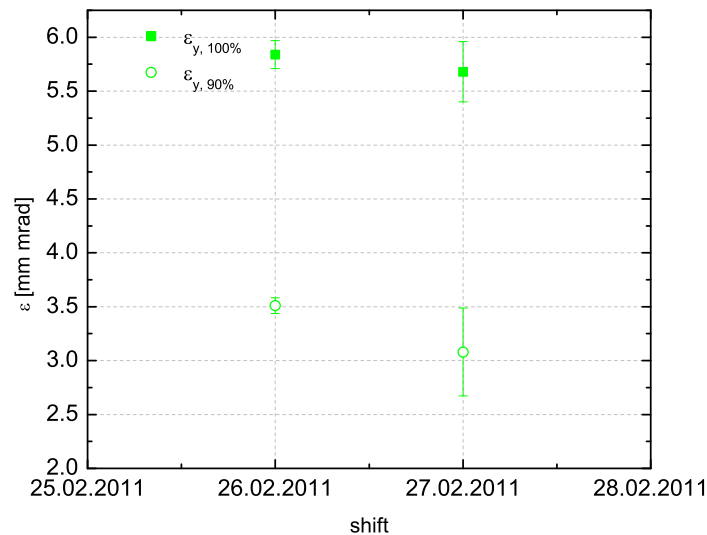

Figure 6.8: Vertical normalized emittances from the two measurements for 100% (full square) and 90% (hollow circle) of the beam intensity. The photo-injector parameters are set as in Table 6.2.

though the measured emittance values are close, the beam halo is characteristic with different features in the two cases wherefrom one can assume that the horizontal mismatch

again originates mainly from the tails in the projections used to calculate the beam envelope parameters. The major difference between the two days is the unexplained increase of the booster power with which the focusing conditions and the beam trajectory change. If the trajectory through the booster cavity or the centers of the quadrupole magnets is influenced, dispersion effects might occur which can explain bad focusing around the beam core similar to the one in the second measurement depicted in Fig. 6.7(b). Such an assumption related to the transport through the quadrupoles might be excluded due to the small mismatch meaning that the beam has inherent tails even upstream of the matching quadrupoles. The elongated tails in the distribution from Fig. 6.7(b) together with the bigger error bars seen in Fig. 6.8, calculated from the reconstruction of the 20 images from each screen, imply possible shot-to-shot fluctuations. The last lead to smearing of the averaged spatial transverse distributions used to calculate the projections and respectively significant differences between the 20 statistical images on each screen.

The emittance decreases almost twice for 90% of the beam intensity. This means that the tails in the reconstructed transverse phase space have a significant contribution to the calculated emittance. That can be related to chromaticity induced by the quadrupoles or some remnant dispersion due to beam transport along the linac. As the weight of the above mentioned satellites increased towards the tomography module they also contribute mostly to the tails of the phase-space density distributions. The reconstruction from which 90% emittance is calculated and a summary table with results are shown in Fig. 6.9 and Table 6.3.

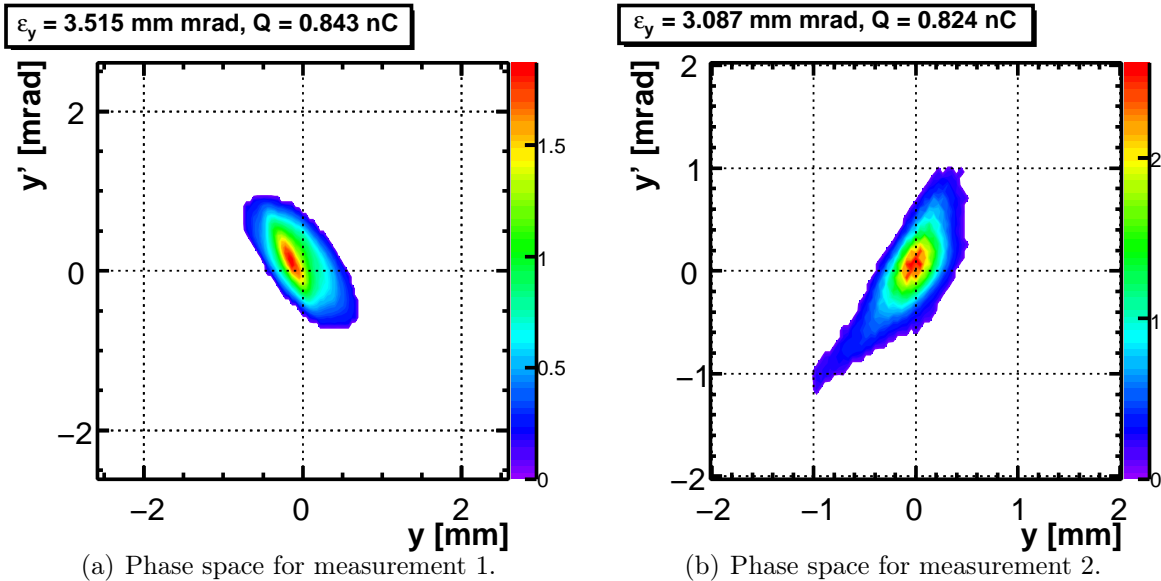(a) Phase space for measurement 1.   (b) Phase space for measurement 2.

Figure 6.9: Reconstruction of the vertical phase spaces on two consecutive measurement days. 10% of the integrated intensity is excluded in order to calculate 90% emittance. The machine paramenters corresponding to these measurements are listed in Table 6.2.
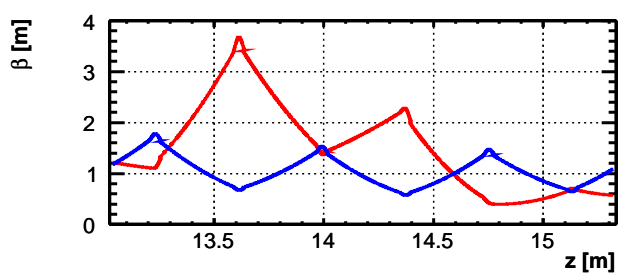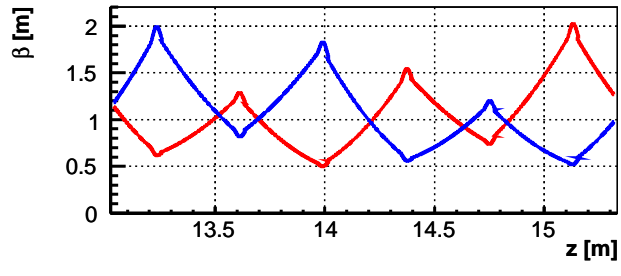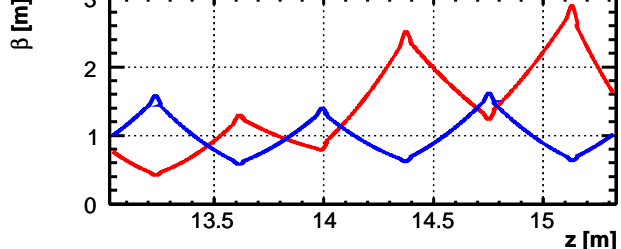
Table 6.3: Measured vertical emittances corresponding to 100% and 90% of the beam intensity for the reconstructed distributions from Fig. 6.7 and Fig. 6.9.

	$\varepsilon_{y,100\%} \pm \sigma_{statistical} \pm \sigma_{systematical}$	$\varepsilon_{y,90\%} \pm \sigma_{statistical} \pm \sigma_{systematical}$
Measurement 1	$5.84 \pm 0.13 \pm 0.25$	$3.52 \pm 0.07 \pm 0.3$
Measurement 2	$5.68 \pm 0.28 \pm 0.25$	$3.09 \pm 0.22 \pm 0.25$

6.4 Dependence on the laser spot size

The transverse phase space was measured as a function of the laser spot size on the photocathode in order to estimate the effect of the laser transverse size on the matching efficiency and the emittance increase. Table 6.4 shows the charge densities onto the cathode and the obtained β-functions along the FODO lattice for which measurements at 1 nC bunch charge were performed. Each line entry in the table indicates the solenoid current for a particular radius of the laser beam R for which minimum emittance on EMSY1 was experimentally obtained. Emittance values and reconstructed phase space results are given in Appendix B.1.

Table 6.4: Charge density and matching efficiency for solenoid currents delivering minimum emittance measured at the end of the injector. Red curves represent the horizontal plane and blue the vertical. The β-functions are obtained from the reconstruction results and transported using linear approximation along the FODO structure.

#	R_{laser} [mm]	I_{main} [A]	charge density [nC/mm^2]	Matching efficiency -
A.	0.3	393	1.23	
B.	0.37	388	0.81	
C.	0.4	389	0.69	

From these plots it cannot be concluded that the periodicity of the particle trajectories inside the FODO lattice improves as the charge density decreases. Such a judgement is subjective since only the initial matching was done using MAD and additional adjustements were done by hand. The plots show the effect of the satellites on the simultaneous matching of the two transverse planes. The quadrupole focusing is appropriate to control the beam envelope in the vertical plane, while the same cannot be done for the horizontal plane.

The results from the measurements, together with the expectations from numerical particle tracking, are summarized in Fig. 6.10(a) and Fig. 6.10(b). Simulations for a laser

(a) Horizontal emittances.   (b) Vertical emittances.
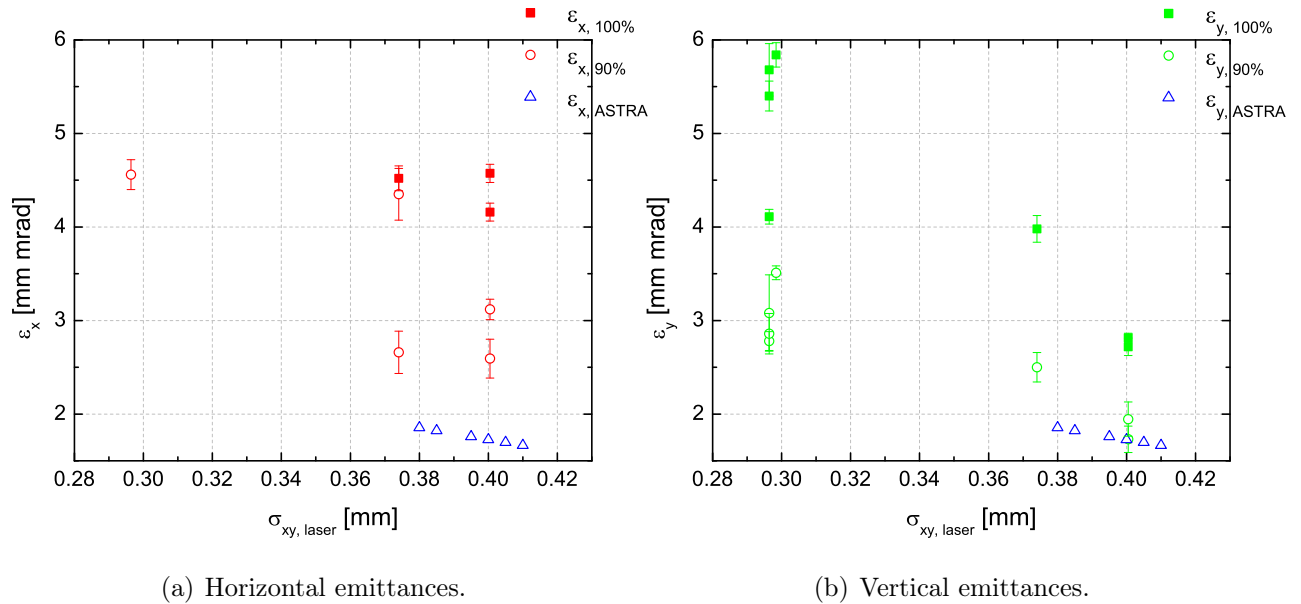
Figure 6.10: Measured and simulated emittances at the position of the first screen of the tomography module as a function of the transverse laser spot size on the photo-cathode. All the measurements are done with the injector parameters listed in Table 6.1. The emittance value for 100% of the integrated intensity for laser spot size of 300 um is not included in the plot for the horizontal plane due to the big mismatch seen in Fig. 6.4.

transverse spot size of 0.3 mm were not possible due to constraints related to the ammount of extracted charge in ASTRA. Considering the 90% emittance the simulations correctly describe the trend of the dependence on the laser spot size. The simulated results correspond to solenoid currents for a particular laser transverse size, with which smallest emittance on EMSY1 can be obtained. It is not necessary that this current corresponds to the one found with measurements.

6.5   Measurements with low bunch charges

6.5.1   Measurements at 100 pC

The transverse phase space was measured also for a bunch charge of 100 pC. The transverse laser profile on the photo-cathode was kept fixed with an rms spot size of 0.125 mm and

the solenoid current was varied. The other machine parameters were set as in Table 6.1.
The charge density at the photo-cathode is comparable to the case of initial laser transverse
profile of 0.4 mm for 1 nC from Table 6.4 and the matching here was mostly successful. The
results for 100% and 90% of the reconstructed intensity are summarized in Fig. 6.11.
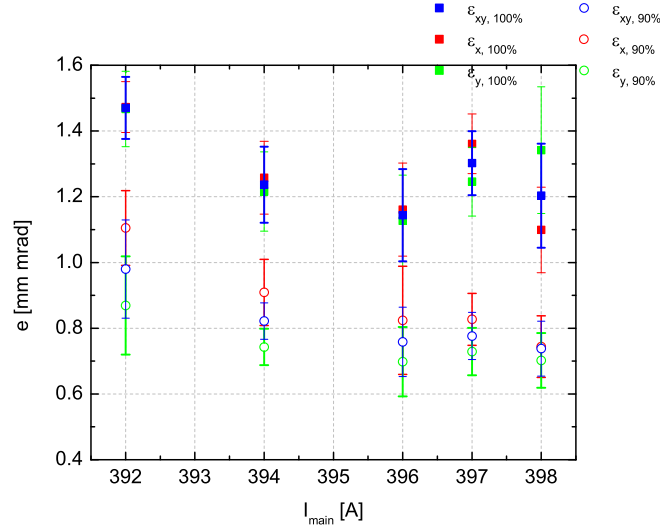

Figure 6.11: Measured horizontal (red) and vertical (green) emittances and the geometrical one (in
blue) for 100% and 90% of the equivalent charge density. The error bars correspond to statistical
fluctuation within the 20 frames used for the analysis of each point.

The emittances for the two transverse planes are closer to each other than in the 1 nC
measurements. Fig. 6.12 shows the reconstructions for main solenoid currents of 392 A,
396 A and 398 A.

Also for this charge one of the transverse density distributions is characteristic with the
micro-structure seen before -satellite on the side - now the horizontal. While the distribu-
tions for the horizontal plain decrease their area with increasing solenoid current, the ones
describing the vertical plane tend to stretch demonstrating the different dynamics governing
the two transverse planes. Excluding the low intensity halo, the vertical phase spaces develop
to Gaussian distributions and their linearity increases with higher main solenoid currents.
The weight of the tails shown in dark blue increases which leads to the higher calculated
emittance values.

The measurement at 398 A was taken a day later than the rest with remeasured gun
and booster phases. The beam mean momentum is the same. Despite the features similar
to the other solenoid currents, the emittances are slightly different with bigger error bars.
The error bars describe the statistical deviation within the 20 images used, leading to the
conclusion some shot-to-shot fluctuations were present.
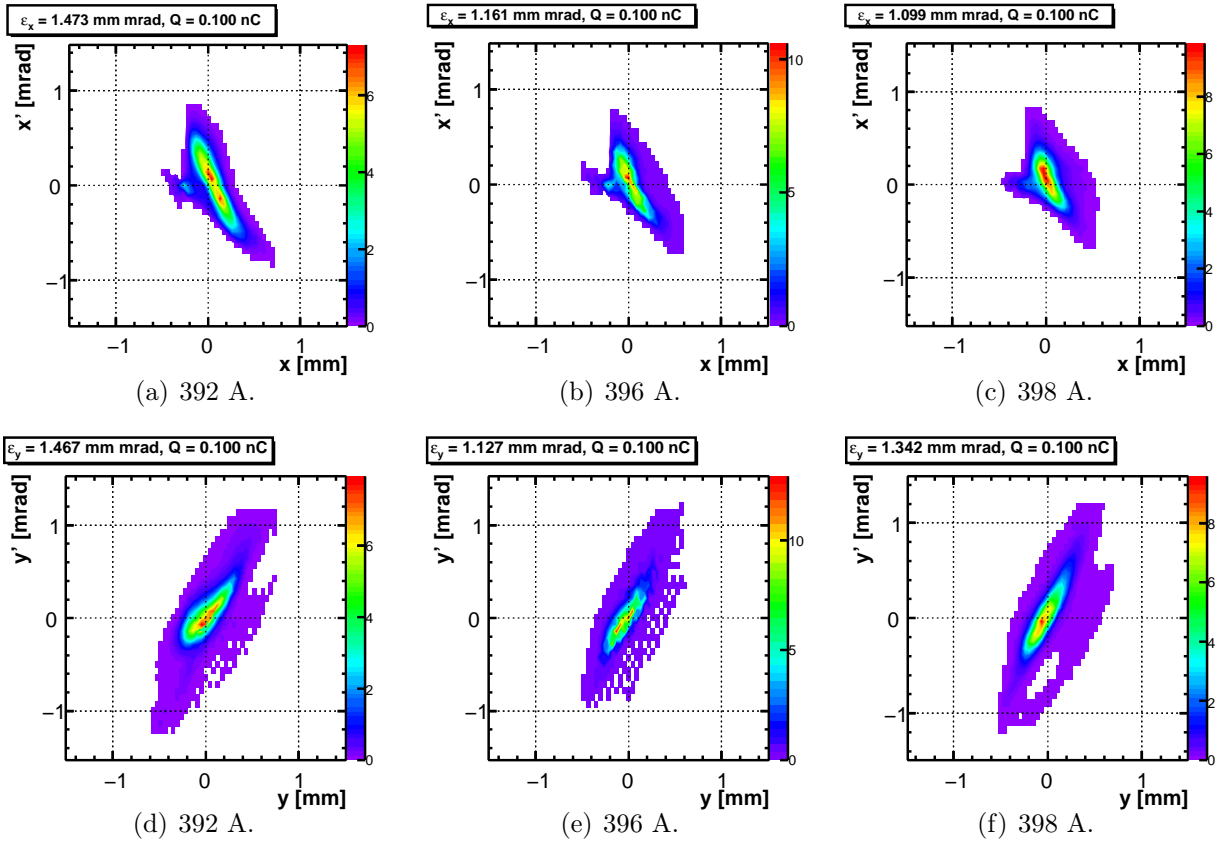
Figure 6.12: Reconstruction of the horizontal (top) and vertical (bottom) planes for 100 pC bunch charge. The middle column at 396 A corresponds to minimum emittance measured at EMSY1.

6.5.2 Consistensy of the reconstruction for low charges

The evolution of the electron beam was followed downstream also for a bunch charge of 250 pC and laser spot size on the photocathode of 0.21 mm. The solenoid current delivering minimum emittance on EMSY1, where the slit scan technique was used, was also measured with tomographic reconstruction. Both methods reveal bifurcation of the vertical phase space as demonstrated in Fig. 6.13. Effects like that are associated with the non-linear dynamics governing the beam evolution. The equivalent charge in the tails is more than 10% of the integrated intensity as without it the emittances decreases by about 30 % - Fig. 6.13(c).

These three plots confirm that the tomographic reconstruction correctly represents the underlying phase space density distribution also for low charges. The EMSY1 data needed 14 bunches in the pulse train to obtain good signal quality, 2 pulses were needed for the tomography, therefore, the disadvantage to introduce smearing of details is minimized.

Conclusions

This chapter presented experimenal results with the tomography module. It was shown that:

1. the results are consistent with ones from slit scans performed on EMSY stations surrounding the module; for these experiments PITZ was set for nominal operational con-
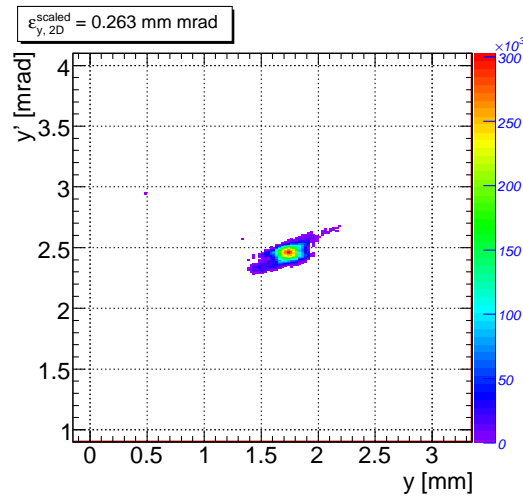
(a) EMSY1 reconstruction.
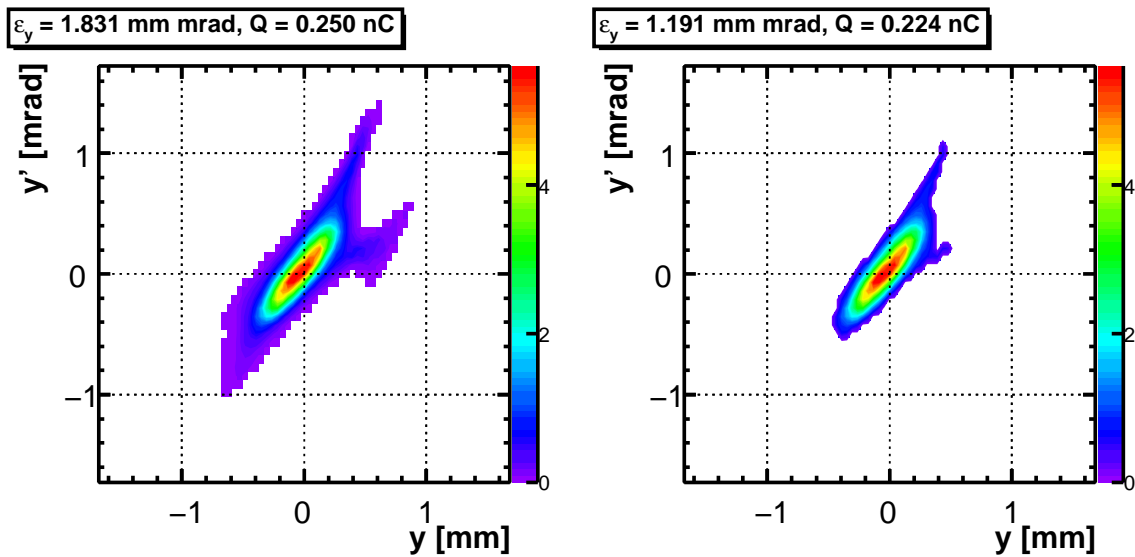
(b) Tomographic reconstruction with 0.1% intensity cut.

(c) Tomographic reconstruction with 10% intensity cut.

Figure 6.13: Vertical phase space measured at EMSY1 (top) and on the first screen of the tomography module (bottom). The specific tails developing already at EMSY1 are being more pronounced further downstream of the photocathode. The reconstruction with 10% intensity cut shows the weight in the tails and the impact on the emittance - about 30 % of the emittance results from them as the equivalent charge is about 10 %.

ditions - bunch charge of 1 nC, maximum obtainable beam momentum of 25 MeV/c and transverse emittance about 1 mm·mrad measured directly at the injector exit behind the booster cavity; those results showed significant dilution of the transverse phase spaces, measured with single pulse per screen which was not possible by the EMSY measurements where minimum of 6 pulses were needed;

2. simulated measurements of the emittance as a function of the laser spot size for the mentioned nominal operational conditions confirmed the trend of the measured emittances for 90 % of the integrated intensity; the difference for the 100 % intensity is believed to originate from the secondary structures visible in the beam profile in Fig. 6.1;

3. the phase-space density distributions of the two transverse planes can be measured simultaneously for high and low charges for short pulse trains with very good resolution;

4. results from the tomographic measurements can be reproduced with different set of focusing strengths of the matching and FODO quadrupoles; the experiments were performed in two consecutive days with readjusted machine parameters; machine fluctuations were revealed using single pulse per screen;

5. the two transverse planes are influences by different dynamics; this was revealed by the linearization of the vertical phase space for 100 pC bunch charge with increasing weight in the tails, while a secondary substructure in the horizontal plane was coming closer to the main beam while varying the solenoid current;

6. the consistency of the low-charge measurements was proven for bunch charges lower than the nominal; charge of 250 pC was used; bifurcation of the vertical phase space was observed using both methods - slit scan and tomographic reconstruction; the slit scan needed 14 pulses in the pulse train to obtain good signal-to-noise while 2 pulses were sufficient for the tomographic measurement.

Chapter 7

Conclusions and Outlook

The PITZ beamline is extended with a module for transverse phase-space tomographic diagnostics. Unique about the setup are the conditions in which it operates:

- low beam energies,

- high charge densities and

- strong space-charge effects.

The physical setup of the module consists of four observation screens separated by three FODO cells. Its performance has been estimated taking into account the actual phase advances between the FODO cells and systematic uncertainties such as beam spot size determination and momentum measurement uncertainties, resolution of the optical read-out system, misalignment of the components and effects of space-charge forces. Any of those systematic difficulties results in unperiodic particle trajectories and consequently drift from the phase advance which delivers the smallest emittance measurement error for such a setup. As a consequence, the quality of the tomographic reconstruction might be limited as the optimal performance by definition requires multiple small equidistant angular steps of the projections. But it was shown that reliable reconstructions of the transverse phase space at PITZ can be obtained.

A number of reconstruction algorithms were tested with respect to the quality of the reconstructed image in the case of limited projection data. Backprojection and its derivative Filtered Backprojection, two basic most commonly used algorithms, were discarded since their performance on several examples was found not to be sufficient. ART and MENT perform better for limited data sets. In terms of visual artifacts and numerical estimates the results from MENT were shown to be more precise. From the given examples one can see that the quality of the reconstruction degrades as the degree of mismatch increases.

A major challenge in the operation of the tomography module is the matching of the electron beam Twiss parameters to the optics of the lattice due to the operating conditions of a photo-injector. A number of matching layouts were investigated with numerical data.

The conclusion was that matching of a space-charge dominated beam is feasible. It was shown that the optimal matching can be achieved only with detailed particle tracking. More efforts are needed in order to automatize the procedure.

First measurements with the tomography module were done for the nominal beam momentum used currently at PITZ and different bunch charges. The measurement results for the most difficult case of 1 nC charge were cross-checked with a well established procedure at PITZ - the slit scan - at locations in front and behind the setup. It was shown that the emittance values calculated from the reconstructed phase-space density distributions are consistent with the values obtained from the slit scans. With numerical simulations it was confirmed that the trend of the decrease in emittance as a function of the laser spot size shown by the tomographic reconstruction is correct. An obstacle for the measurements was the transverse profile of the electron beam which was shown to develop low intensity horizontal tails drifting downstream from the booster cavity. It was shown that it is more difficult to match the beam to the optics of the FODO lattice in the plane where the low intensity tails occur but still a good matching is possible there.

In details of the reconstructed distribution it was found that tomography is a more powerful technique as compared to the slit scan. The systematic analysis of a single beam image from a screen revealed possible shot-to-shot fluctuations even at low charges which would be smeared by the slit scans. An additional magnifying lens for the screen readout is needed in order to improve the resolution at charges lower than the measured and at higher beam energies.

A software tool combining data taking and data analysis was prepared and used in the measurements. A number of image analysis algorithms were encorporated.

The design, construction and commissioning of and first results measured with the tomography module are discussed here. At a later stage of the PITZ project, the module will be equipped with kicker magnets. In such a way the transverse distributions of a number of bunches from the bunch train can be reconstructed as a selected pulse is kicked to an off-axis screen by a kicker where it is measured. The rest of the bunch continues to the beam dump or other diagnostics downstream. This possibility was considered in the design of the module but limited resources caused that the first prototype kicker will not be installed before the end of 2011.

In future an RF deflecting cavity will be used to streak the beam vertically and combining the tomography setup with the kickers and this cavity will give the possibility to study the longitudinal distribution of a single pulse in the bunch train.

To facilitate the quality of the reconstruction for the high current longitudinal slices as well as for the phase space of the full beam, the description of the transport between the measuring screens has to incorporate space-charge effects. A possible solution incorporating linear and non-linear space-charge forces is already being developed. This so called V-code [103] is currently being tested with numerical data.

Appendix A

Quadrupole magnet

The only source of external focusing applied to the electron beam after it has achieved final momentum originates from quadrupole magnets. A cross-section demonstrating the forces induced by a quadrupole is given in Fig. A.1. The quadrupole is horizontally focusing and
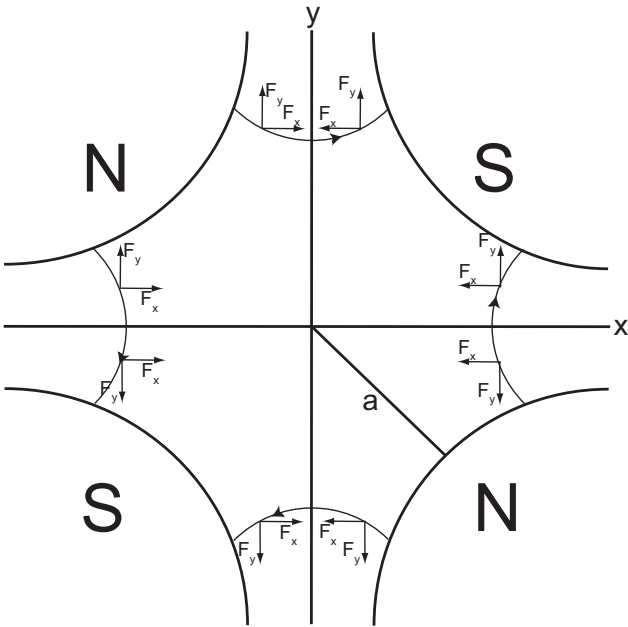
Figure A.1: Force components in a quadrupole magnet with bore radius a.

vertically defocusing with the same focusing strength for a negatively charged particle going into the plane of the drawing. Here the coordinate system introduced in chapter 3 is used.

The magnetic field components

$$
B_x = gy \\
B_y = gx
$$
(A.1)

with g denoting the gradient of the field, scale linearly with the distance from the magnet axis and the transverse kick applied to a particle depends on its offset with respect to the magnet axis. Fig. A.2 shows the trajectories of a number of particles having different phase-space coordinates.
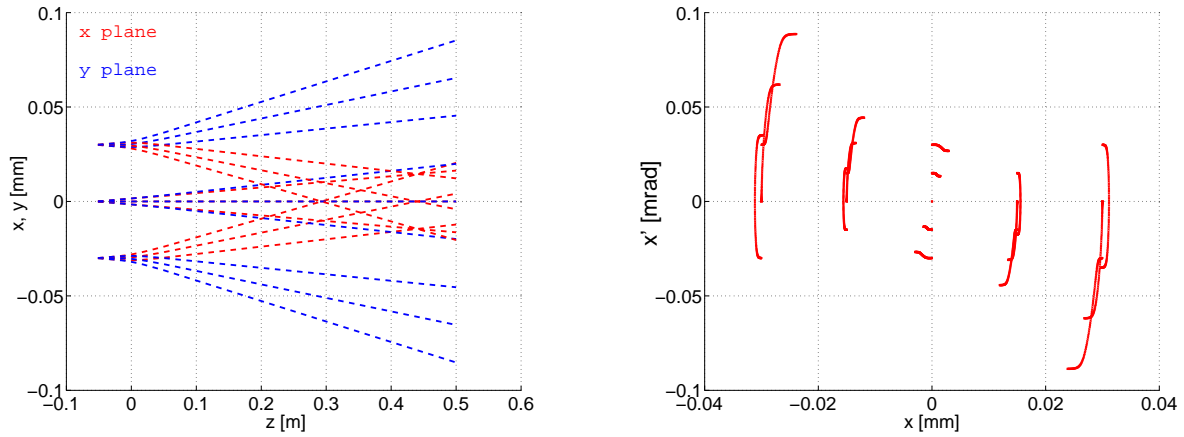
(a) Trajectories of particles passing through a quadrupole magnet whose center is at z = 0. The particles are focused at about 0.45 m and continue drifting downstream.

(b) In the (x, x') plane the particles project an elliptical orbit.

Figure A.2: Individual particle trajectories in the (x, z) and (y, z) (left) and (x, x') (right) planes. The figures are obtained using linear transport through a quadrupole and a drift space.

The linear transport matrix formalism uses hard-edge quadrupoles. In order to better approximate the fields, the calculation of the matrices, needed for the tomographic reconstruction, is based on the division of one magnet into short ones having effective length of 1e-3 m and interpolating the strengths between the centers of each two neighbouring short magnets. The resulting strength map for nominal strength of k = 48.716 m^{-2} is shown in Fig. A.3.
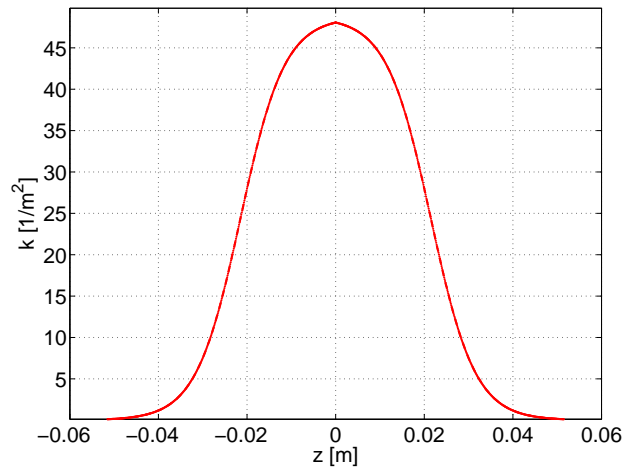

Figure A.3: The strength of a hard-edge quadrupole is mapped onto a Gaussian curve as 430 short magnets with effective length of 1 mm are used to represent a standard one with effective length of 0.043 m.

Appendix B

Reconstructed distributions and tables with results

B.1 Measurements at 1 nC as a function of the laser spot size.

Measured values

Table B.1: Horizontal emittance measured at 1 nC as a function of the laser spot size for various main solenoid currents I_{main}. A dash is used where the matching was not considered satisfactory.

#	σ_{laser} [mm]	I_{main} [A]	$\varepsilon_{x,100\%} \pm \sigma_{stat} \pm \sigma_{sys}$ [mm.mrad]	$\varepsilon_{x,90\%} \pm \sigma_{stat} \pm \sigma_{sys}$ [mm.mrad]
A.	0.30	393	-	-
B.	0.30	393	-	-
C.	0.37	388	$4.52 \pm 0.13 \pm 0.28$	$2.66 \pm 0.23 \pm 0.34$
D.	0.37	390	$6.60 \pm 0.31 \pm 0.39$	$4.35 \pm 0.28 \pm 0.37$
E.	0.40	389	$4.16 \pm 0.10 \pm 0.26$	$2.81 \pm 0.05 \pm 0.32$
F.	0.40	390	$4.57 \pm 0.10 \pm 0.27$	$2.72 \pm 0.09 \pm 0.27$

Table B.2: Verical emittance measured at 1 nC as a function of the laser spot size for various main solenoid currents I_{main}. A dash is used where the matching was not considered satisfactory.

#	σ_{laser} [mm]	I_{main} [A]	$\varepsilon_{y,100\%} \pm \sigma_{stat} \pm \sigma_{sys}$ [mm.mrad]	$\varepsilon_{y,90\%} \pm \sigma_{stat} \pm \sigma_{sys}$ [mm.mrad]
A.	0.30	393	$5.68 \pm 0.28 \pm 0.25$	$3.09 \pm 0.22 \pm 0.25$
B.	0.30	393	$5.84 \pm 0.13 \pm 0.25$	$3.52 \pm 0.07 \pm 0.3$
C.	0.37	388	$3.98 \pm 0.14 \pm 0.28$	$2.50 \pm 0.16 \pm 0.37$
D.	0.37	390	-	-
E.	0.40	389	$2.81 \pm 0.05 \pm 0.25$	$1.95 \pm 0.18 \pm 0.37$
F.	0.40	390	$2.72 \pm 0.09 \pm 0.26$	$1.73 \pm 0.14 \pm 0.30$

Measured phase-space distributions

(a) $\sigma_{laser} = 0.37$ mm, $I_{main} = 388$ A.

(b) $\sigma_{laser} = 0.37$ mm, $I_{main} = 390$ A.

(c) $\sigma_{laser} = 0.4$ mm, $I_{main} = 388$ A.

(d) $\sigma_{laser} = 0.4$ mm, $I_{main} = 390$ A.
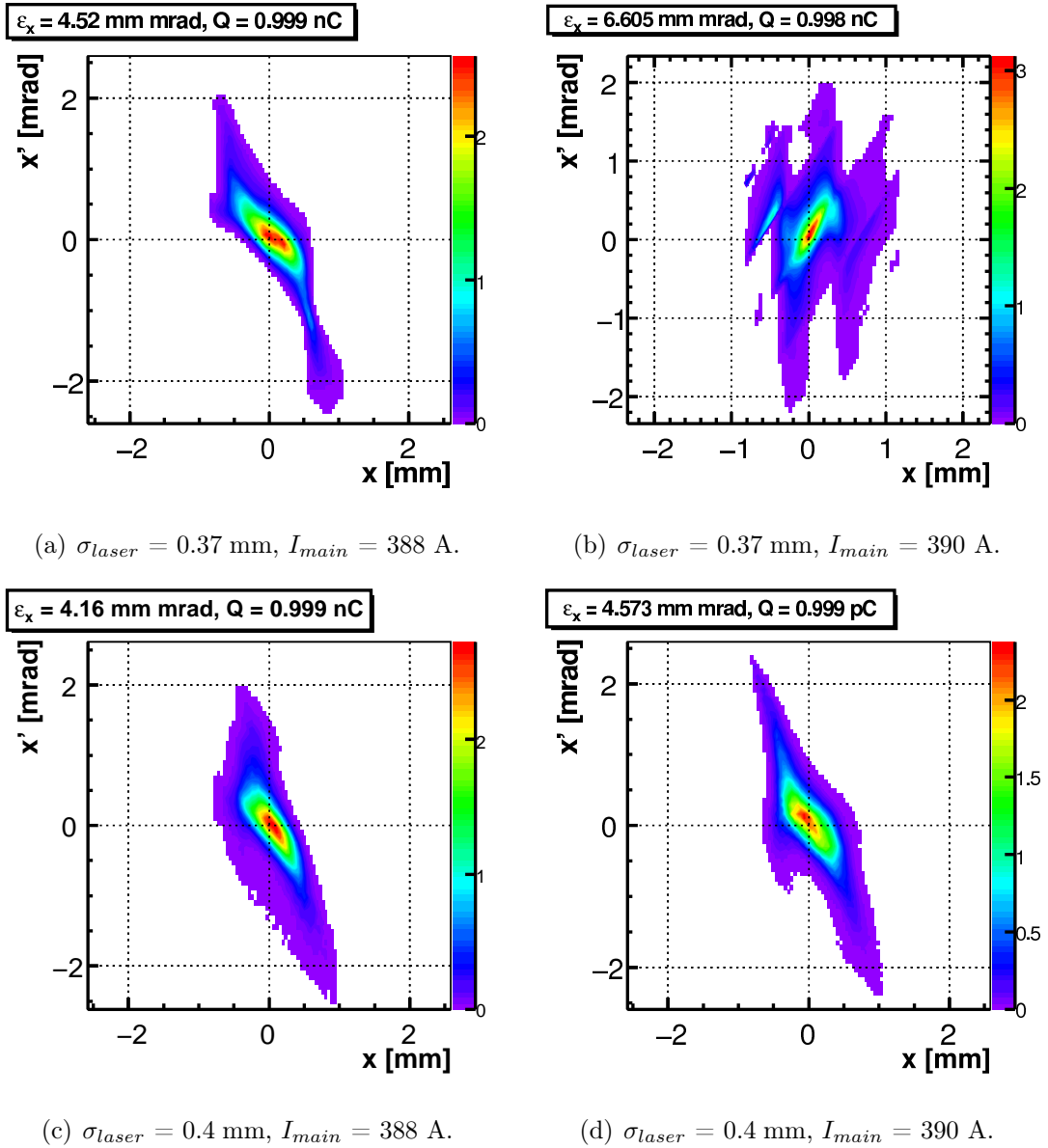
Figure B.1: Reconstructed horizontal phase spaces for 1 nC bunch charge.

B.1. Measurements at 1 nC as a function of the laser spot size.

(a) $\sigma_{laser} = 0.3$ mm, $I_{main} = 393$ A.

(b) $\sigma_{laser} = 0.3$ mm, $I_{main} = 393$ A.

(c) $\sigma_{laser} = 0.37$ mm, $I_{main} = 388$ A.

(d) $\sigma_{laser} = 0.4$ mm, $I_{main} = 389$ A.

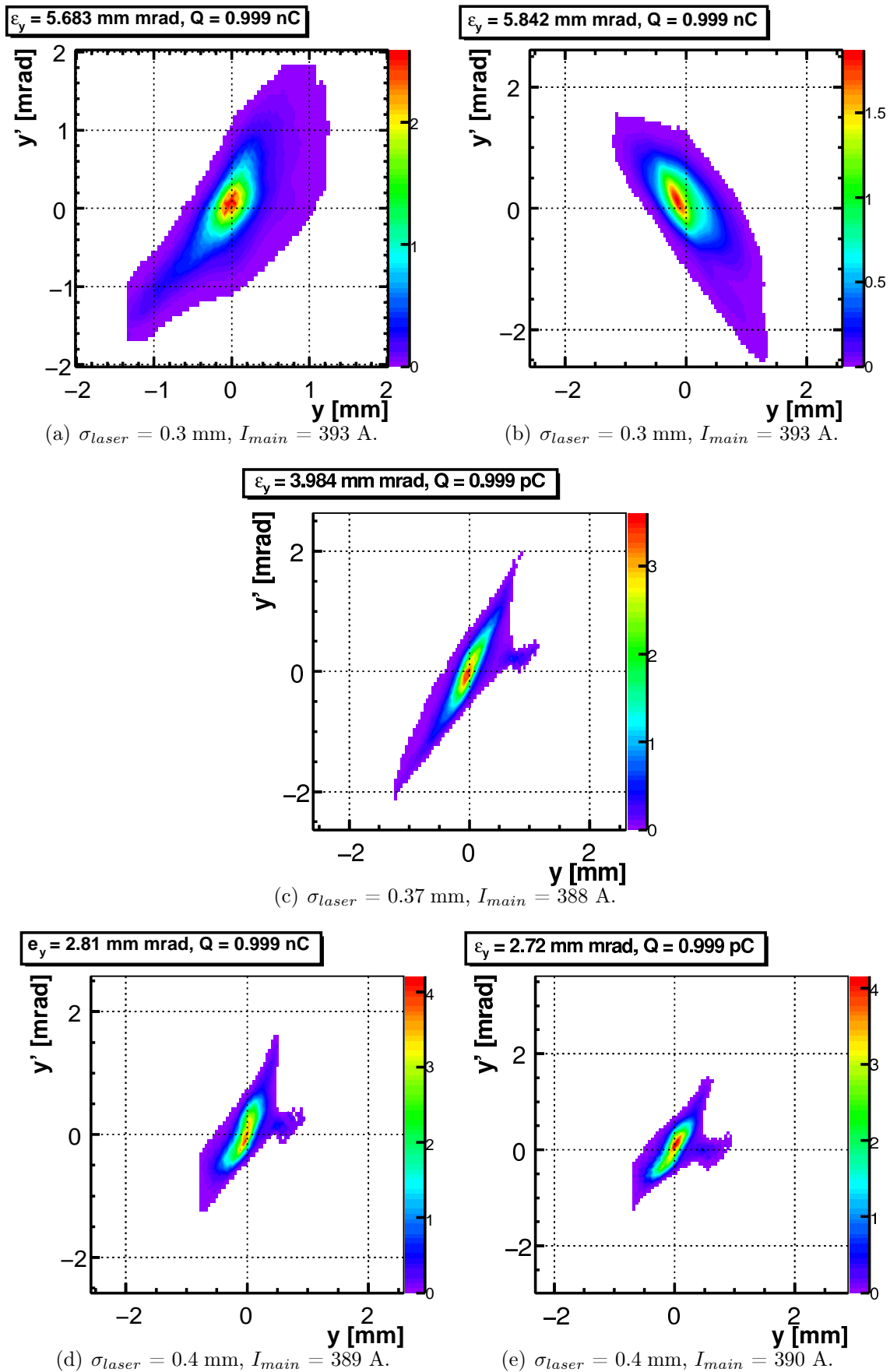(e) $\sigma_{laser} = 0.4$ mm, $I_{main} = 390$ A.

Figure B.2: Reconstructed vertical phase spaces for 1 nC bunch charge. The different orientation of the phase spaces in Fig. B.2(a) and Fig. B.2(b) is discussed in Section 6.3.

Appendix C

Image analysis

An image describing the spatial (x, y) profile used for tomographic reconstruction contains 20 consecutive images of the beam distribution, called later signal, and the same number of background images. The background characterizes effects like dark current inherent to the beam, electronic noise, dark current or gain noise from the camera and damaged pixels on the CCD. The steps to be done before a projection, that will be used in the reconstruction, is defined are:

1. Image filtering, i.e. defining whether the intensity in a pixel describes only the electron beam or it also contains some noise.

   An average intensity and statistical standard deviation for a single pixel are calculated for both the signal and the background data using the 20 images. Having this information the following image denoising procedure is applied:

   (a) The mean intensity of a pixel from the background data is subtrated from the mean of the pixel from the signal data. If the resulting intensity is negative, it is set to zero.

   (b) A pixel in the resulting CCD matrix is treated as probable beam signal if the mean signal intensity is bigger than one sigma of the noise added to the mean pixel noise.

   (c) An adaptive median filter is applied to the image resulting from the previous step. This filter uses the information in some range of neighbours to define if a pixel is representative for a cluster of pixels, here the pixels in 5 neighbouring rows and columns are used.

   Fig. C.1 shows an averaged signal image (left top) and the resulting ones after steps 1a, 1b and 1c. To evaluate the statistical deviation of the reconstructed phase-space distributions step 1a is skipped, i.e. the background from a single image is subtrated from a single signal.
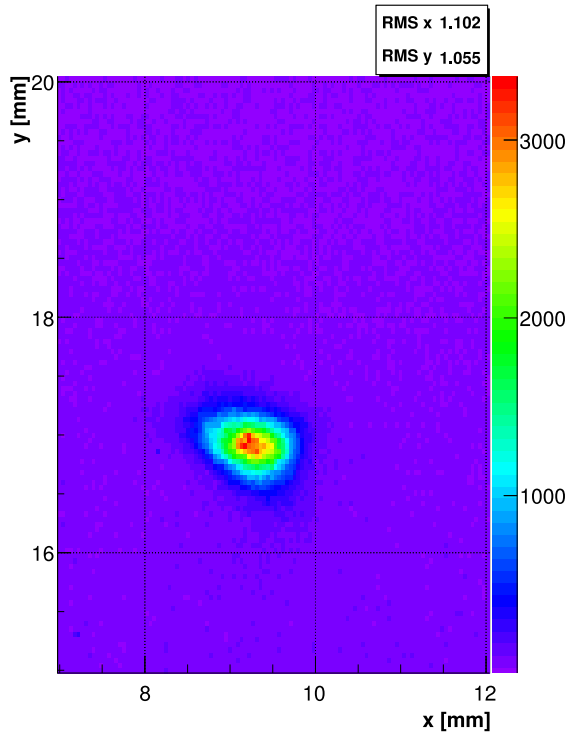
(a) Signal averaged over 20 images.
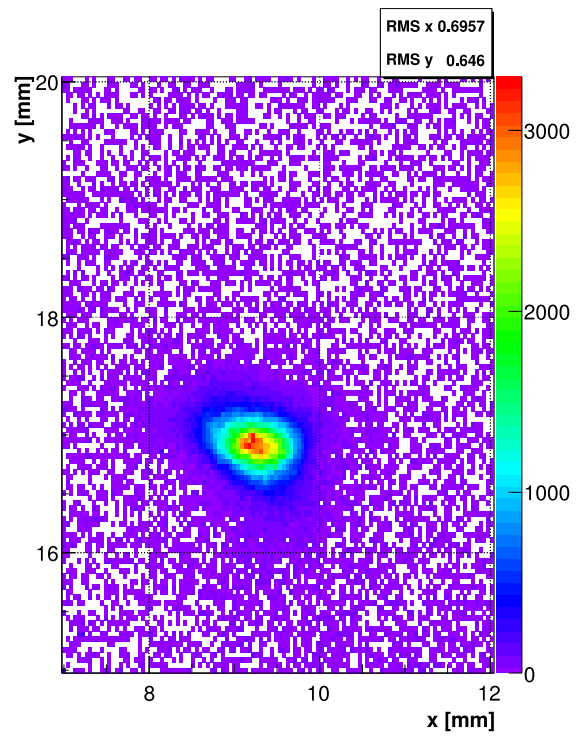
(b) Averaged background subtrated from the averaged signal.
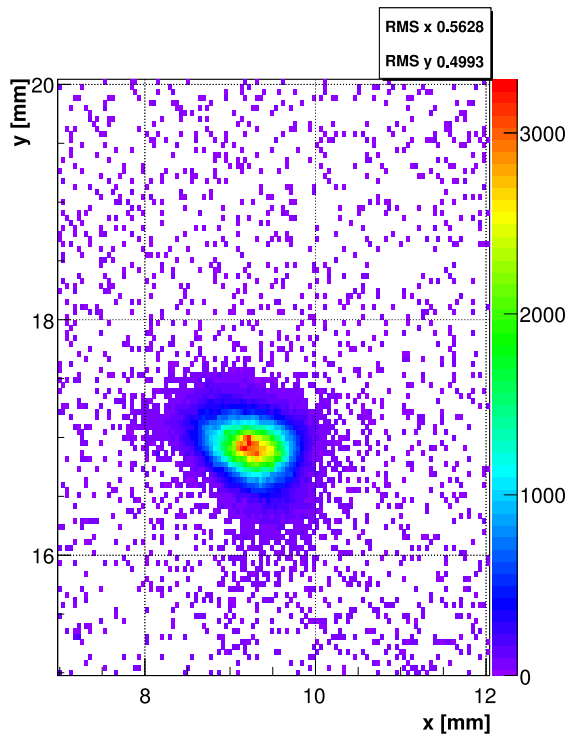
(c) One sigma of the noise are subtrated from the result in Fig. (b).
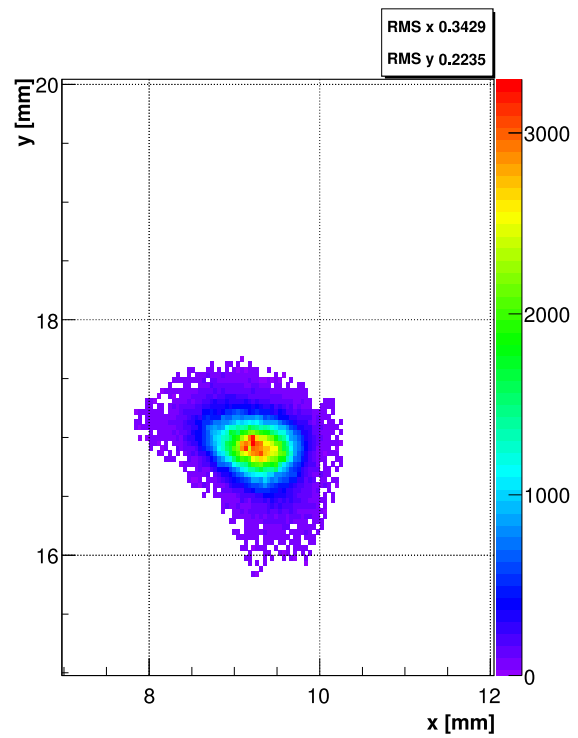
(d) Adaptive median filter is applied.

Figure C.1: Steps in image filtering. The images are zoomed.

2. Defining a region of interest (ROI) containing only relevant beam distribution. The ROI contains five times the rms spot size of the filtered beam spatial distribution (the bigger one from the horizontal and the vertical is taken). This step aims to decrease the size of the projection and to define a square matrix fully containing the electron beam.

3. Centering the projections from the four screens to a new cartesian coordinate system centered at $(0,0)$.

4. Defining a common ROI for the four images. The ranges from the four (x, y) distributions are compared and the biggest one is used.

5. Zero-padding each of the images where it is needed to fit the ROI from step 4.

The cameras installed along the tomography module can be used with the full resolution of the CCD or in a binned mode where four neighbouring pixels, two horizontal and two vertical, are combined logically into one. The procedure listed above is applied on any of these two binning modes.

After the zero-padding a projection from each of the four tomography screens is defined.

Nomenclature

ART   Algebraic Reconstruction Technique

BP   Backprojection

BPM Beam Position Monitor

caART Constrainted Additive ART

EMSY Emittance Measurement SYstem

EMSY1 Emittance Measurement SYstem 1 along the PITZ beamline

FBP   Filtered Backprojection

FODO Focusing-Defocusing

HEDA High Energy Dispersive Arm

LEDA Low Energy Dispersive Arm

MENT Maximum Entropy

OTR   Optical Transition Radiation

QE   Quantum Efficiency

YAG Yttrium-Aluminum-Garnet

Acknowledgments

First of all I would like to express my gratitude to Assos. Prof. Ivan Tsakov, Dr. Frank Stephan, Dr. Mikhail Krasilnikov, Prof. Dr. Jordan Stamenov, Dr. Ulrich Gensch and Dr. Hans-Jürgen Grabosch for giving me the possibility to work at PITZ. I'm sure PITZ is the only place where one can actually live in the process from designing a device to seeing it functional and, more importantly, useful.

My most sincere thanks to Dr. Sergiy Khodyachykh for his support on the tomography project, for introducing me to the field of accelerator physics and the great atmosphere he is able to create. Sergiy, it's tough but it works! Dr. Sven Lederer constantly pushed me forward, showed me how not to be afraid of the machine and made the night shifts fun, even though he can be *pingelich*. Dr. Lazar Staykov shared with me the insights of numerical simulations and beam dynamics, dwelling with me on many thresholds.

The tomography module wouldn't be such a beautiful structure without the devoted work of Dr. Jürgen Bähr, Jochen Bienge, Joachim Meissner, Sebastian Philipp, Riccardo Anders, Gerald Koss, Dr. Anne Oppelt, Frank Tonisch, Jörg Schultze, Markus Schade, Ralf Netzel who took care that every detail is on its place.

Ivan Bonev was there with me when the first measurements came and shared my excitement and frustration. *Бона, благодаря!*

Dr. Sakhorn Rimjaem and Dr. Matthias Gross must have had a tough time with me. Either having shifts doing tomography or reading the thesis, they joined me in my struggle to go beyond the understanding of emittance measurement I had before. My sincere gratitude to the PITZ shift crews for their patience, willingness to discuss and play with such a nice machine even at 5 a.m. on Sundays.

Bagrat Petrosyan, Dr. Gunter Trowitzsch, Stefan Weisse, Levon Hakobyan made sure any problem related to the control system can be solved. I deeply admire the ease with which you are able to do that. Dr. Michael Winde is the original source of my programming skills, the way I face programming challenges to a great extend is shaped by him.

Dr. Klaus Flötmann, Dr. Katja Honkavaara, Dr. Siggi Schreiber were constantly ready to share their good mood, knowledge and experience.

Thanks to the Joint University Accelerator School, to the TEMF at TU Darmstadt for their wish to make the V-code useful, to the Daresbury Lab for buying the magnets.

I'm greatly thankful to Dr. Orlin Dimitrov, Dr. Borislav Dimitrov and Dodo Kalcheva for all the tender care and the human understanding. You didn't give up in the hardest moments. You became part of my family.

I owe my great appreciation to my parents, *Снежана и Лазар Асови*, for all the encouragement, trust and support. I promised to go until the end. My Dad didn't live long enough to see the job done but I'm sure he is proud I kept my promise. I owe my curiousity to him and I delightfully share the joy with him. *Благодаря, обичам ви!*

Publication list

1. G. Asova, H.J. Grabosch, M. Gross, L. Hakobyan, I. V. Isaev, Y. Ivanisenko, M. Khojoyan, G. Klemz, M. Krasilnikov, M. Mahgoub, D. A. Malyutin, A. Oppelt, M. Otevrel, B. Petrosyan, D. Richer, S. Rimjaem, A. Shapovalov, F. Stephan, G. Vashchenko, First results with tomographic reconstruction of the transverse phase space at PITZ, *proceedings FEL 2011*, Shanghai, China

2. G. Asova, M. Krasilnikov, J. Saisut, F. Stephan, Methodical studies for tomographic reconstruction as a novel method for emittance measurements at the PITZ facility, *proceedings LINAC 2010,* Tsukuba, Japan

3. G. Asova, J. Bähr, H.J. Grabosch, L. Hakobyan, M. Hänel, Y. Ivanisenko, M. Khojoyan, G. Klemz, M. Krasilnikov, S. Lederer, M. Mahgoub, B. O'Shea, M. Otevrel, B. Petrosyan, D. Richer, S. Rimjaem, A. Shapovalov, L. Staykov, F. Stephan, G. Vashchenko, Phase space measurements with tomographic reconstruction at PITZ, *proceedings FEL 2010*, Malmö, Sweden

4. G. Asova, S. Khodyachykh, M. Krasilnikov, F. Stephan, P. Castro, F. Loehl, Phase-space tomography diagnostics at the PITZ facility, *proceedings ICAP 2006*, Chamonix, France

5. G. Asova, S. Khodyachykh, M. Krasilnikov, F. Stephan, K. Flöttmann, D.J. Holder, B. Muratori, Design considerations for phase-space tomography diagnostics at the PITZ facility, *proceedings DIPAC 2007*, Venice, Mestre, Italy

6. G. Asova, S. Khodyachykh, S. Korepanov, M. Krasilnikov, S. Rimjaem, F. Stephan, K. Floettmann, D.J. Holder, B. Muratori, Design of a tomography module for the PITZ facility, *proceedings EPAC 2008*, Genova, Italy

7. G. Asova, S. Khodyachykh, M. Krasilnikov, F. Stephan, I. Tsakov, Tomographic reconstruction from limited projection data, *proceedings ICAP 2009*, San Francisco, USA

8. G. Asova, J.Bähr, C. H. Boulware, A. Donat, U. Gensch, H.J. Grabosch, L. Hakobyan, M. Hänel, H. Henschel, Y. Ivanisenko, L. Jachmann, M. Khojoyan, W. Köhler, G. Koss, M. Krasilnikov, A. Kretzschmann, H. Leich, H. Lüdecke, A. Meissner, B. Petrosyan, M. Pohl, S. Riemann, S. Rimjaem, M. Sachwitz, B. Schöneich, J. Rönsch-Schulenburg, J. Schultze, A. Shapovalov, R. Spesyvtsev, L. Staykov, F. Stephan, F. Tonisch, G. Trowitzsch, T. Walter, S. Weisse, R. Wenndorff, M. Winde, G. Vashchenko, L. v. Vu, K. Flöttmann, S. Lederer, S. Schreiber, D. Richter, D.J. Holder, B. Muratori, Status of the Photo injector test facility at DESY, Zeuthen site, *proceedings IPAC 2010*, Kyoto, Japan

9. F. Stephan, C.H. Boulware, M. Krasilnikov, J. Bähr, G. Asova, A. Donat, U. Gensch, H.-J. Grabosch, M. Hanel, L. Hakobyan, H. Henschel, Y. Ivanisenko, L. Jachmann, S. Khodyachykh, M. Khojoyan, W. Kohler, S. Korepanov, G. Koss, A. Kretzschmann, H. Leich, H. Ludecke, J. Meissner, A. Oppelt, B. Petrosyan, M. Pohl, S. Riemann, S. Rimjaem, M. Sachwitz, B. Schoneich, T. Scholz, H. Schulze, J. Schultze, U. Schwendicke, A. Shapovalov, R. Spesyvtsev, L. Staykov, F. Tonisch, T. Walter, S. Weisse, R. Wenndorff, M. Winde, L. v. Vu, H. Durr, T. Kamps, D. Richter, M. Sperling, R. Ovsyannikov, A. Vollmer, J. Knobloch, E. Jaeschke, J. Boster, R. Brinkmann, S. Choroba, K. Flechsenhar, K. Flottmann, W. Gerdau, V. Katalev, W. Koprek, S. Lederer, C. Martens, P. Pucyk, S. Schreiber, S. Simrock, E. Vogel, V. Vogel, K. Rosbach, I. Bonev, I. Tsakov, P. Michelato, L. Monaco, C. Pagani, D. Sertore, T. Garvey, I. Will, I. Templin, W. Sandner, W. Ackermann, E. Arevalo, E. Gjonaj, W. Muller, S. Schnepp, T. Weiland, F. Wolfheimer, J. Roensch, J. Rossbach, Detailed characterization of electron sources at PITZ yielding first demonstration of XFEL beam quality, *Phys. Rev. ST Accel. Beams*, 13(2):020704, Feb. 2010

Bibliography

[1] XFEL collaboration, The European X-Ray Free-Electron Laser - Technical design report, Technical report, DESY, July 2007.

[2] F. Stephan, C. H. Boulware, M. Krasilnikov, J. Bähr, et al., Detailed characterization of electron sources yielding first demonstration of European X-ray Free-Electron Laser beam quality, *Phys. Rev. ST Accel. Beams*, 13(2):020704, Feb 2010.

[3] S. Schreiber, FLASH - Beam commissioning and operation after upgrade, presentation, PITZ collaboration meeting, December 2010.

[4] P. G. O'Shea and H. P. Freund, Free-Electron Lasers: Status and Applications, *Science*, 292(5523):1853–1858, 2001.

[5] M. Ferrario, Linac Based FELs, Proceedings CAS lectures, 2008.

[6] J. Rossbach, Linac Based Free Electron Lasers, Proceedings CAS lectures, 2003.

[7] E.L. Saldin, E.A. Schneidmiller, M.V. Yurkov, *The Physics of free electron lasers*, Springer-Verlag, 1999.

[8] TESLA collaboration, TESLA Technical design report, Technical report, DESY, 2001, DESY 2001-011.

[9] http://hasylab.desy.de.

[10] M. Ferrario et al., Conceptual design of the XFEL Photoinjector, Technical report, DESY, 2001, TESLA FEL 2001-03.

[11] K. L. F. Bane, F.-J. Decker, Y. Ding, D. Dowell, P. Emma, J. Frisch, Z. Huang, R. Iverson, C. Limborg-Deprey, H. Loos, H.-D. Nuhn, D. Ratner, G. Stupakov, J. Turner, J. Welch, and J. Wu, Measurements and modeling of coherent synchrotron radiation and its impact on the Linac Coherent Light Source electron beam, *Phys. Rev. ST Accel. Beams*, 12(3):030704, Mar 2009.

[12] The project PITZ 2 - development of optimized photo injectors for free electron lasers, Nov 2004, PITZ note.

[13] www.mbi-berlin.de.

[14] M. Krasilnikov et al., Experimental characterization and numerical simulations of the electron sources at PITZ, In *proceedings ICAP 2004*, Sankt-Petersburg, Russia, 2004.

[15] Y. Ivanisenko and M. Hänel, Latest developments in PITZ cathode laser diagnostics, presentation, PITZ collaboration meeting, June 2008.

[16] Y. Ivanisenko, Photo injector cathode laser beam intensity and position monitoring system, Master's thesis, Karazin Kharkiv National University, Ukraine, 2007.

[17] R. A. Powell, W. E. Spicer, G. B. Fisher, and P. Gregory, Photoemission Studies of Cesium Telluride, *Phys. Rev. B*, 8(8):3987–3995, Oct 1973.

[18] W. E. Spicer and A. Herrera-Gomez, Modern theory and applications of photocathodes, Presented at SPIE's 1993 International Symposium on Optics, Imaging and Instrumentation, San Diego, CA, 11-16 Jul 1993.

[19] http://wwwlasa.mi.infn.it/.

[20] D. Sertore et al., Review of the Production Process of TTF and PITZ Photocathodes, In *proceedings PAC 2005*, Knoxville, Tennessee, USA, 2005.

[21] J.-P. Carneiro et al., Behaviour of the TTF2 Gun with long pulses and repetition rates, Technical report, DESY, 2003, TESLA Note 2003-33.

[22] D. A. Reis, *Emittance measurements from a laser driven electron injector*, PhD thesis, Stanford University, California, 1999.

[23] M. Otevrel et al., Conditioning of a New Gun at PITZ Equipped with an Upgraded RF Measurement System, In *proceedings FEL 2010*, Malmö, Sweden, 2010.

[24] S. Korepanov, Solenoid measurements, Presentation, PITZ, 2007.

[25] K. Flöttmann, Some basic features of the beam emittance, *Phys. Rev. ST Accel. Beams*, 6(3):034202, Mar 2003.

[26] V. Paramonov et al., Design parameters of the normal conducting booster cavity for the PITZ-2 test stand, In *proceedings LINAC 2004*, Lübeck, Germany, 2004.

[27] R. Spesyvtsev, Transverse Beam size measurement systems at Photo Injector Test Facility in Zeuthen, Master's thesis, Karazin Kharkiv National University, Ukraine, 2007.

[28] S. Weisse et al., Status of a versatile video system at PITZ, DESY-2 and EMBL HAMBURG, In *proceedings ICALEPC 2007*, Knoxville, Tennessee, USA, 2007.

[29] http://www.jai.com/EN/Pages/home.aspx.

[30] http://www.prosilica.com/products.

[31] http://tine.desy.de.

[32] H.-J. Grabosch et al., Test of a Wire Scanner in the Diagnostic Section of PITZ, In *proceedings FEL 2007*, Novosibirsk, Russia, 2007.

[33] J. Bähr et al., Optical system for measuring electron bunch length and longitudinal phase space at PITZ: extension and methodical investigations, In *proceedings FEL 2006*, Berlin, Germany, 2006.

[34] J. Rönsch et al., Investigations of the longitudinal beam properties at the Photoinjector test facility in Zeuthen, In *proceedings FEL 2006*, Berlin, Germany, 2006.

[35] J. Rönsch, *Investigations on the longitudinal phase space at a photo injector*, PhD thesis, Universität Hamburg, 2009.

[36] S. Khodyachykh et al., New beam diagnostic developments at the Photo-injector test facility PITZ, In *proceedings PAC 2007*, Albuquerque, New Mexico, 2007.

[37] S. Rimjaem et al., Physics and technical design for the second high energy dispersive section at PITZ, In *proceedings DIPAC 2009*, Basel, Switzerland, 2009.

[38] V. Miltchev, *Investigation on the transverse phase space at a photo injector for minimized emittance*, PhD thesis, DESY-THESIS, 2006.

[39] L. Staykov et al., Design optimisation on an emittance measurement system at PITZ, In *proceedings DIPAC 2005*, Lyon, France, 2005.

[40] L. Staykov et al., Comissioning of a new emittance measurement system at PITZ, In *proceedings FEL 2006*, Berlin, Germany, 2006.

[41] L. Staykov, *Characterization of the transverse phase space at the Photo-Injector Test Facility in DESY, Zeuthen site*, PhD thesis, Universität Hamburg, 2008.

[42] L. Staykov et al., Measurement of the Projected Normalized Transverse Emittance at PITZ, In *proceedings FEL 2007*, Novosibirsk, Russia, 2007.

[43] S. Khodyachykh et al., Design considerations of the multipurpose dispersive section at PITZ, In *proceedings FEL 2006*, Berlin, Germany, 2006.

[44] S. Khodyachykh et al., Design and construction of a multipurpose dispersive section at PITZ, In *proceedings 8th European Workshop on Beam Diagnostics and Instrumentation for Particle Accelerators DIPAC 2007*, Venice, Mestre, Italy, 2007.

[45] Y. Ivanisenko et al., Slice Emittance Measurement Using an Energy Chirped Beam in a Dispersive Section at PITZ, In *proceedings FEL 2008*, Gyeongju, South Korea, 2008.

[46] J. Buon, Beam phase space and emittance, Proceedings CAS lectures.

[47] H. Wiedemann, *Particle Accelerator Physics*, Springer, Berlin, 1994.

[48] E. D. Courant and H. S. Snyder, Theory of the alternating-gradient synchrotron, *Ann. Phys.*, 3:1–48, 1958.

[49] N. Pichoff, Transverse beam dynamics, Lectures given at Joint University Accelerator School, Archamps, France, 2007.

[50] M. Reiser, *Theory and Design of Charged Particle Beams*, Wiley, Weinheim, 1994.

[51] P. M. Lapostolle, Possible emittance increase through filamentation due to space charge in continuous beams. (talk), *IEEE Trans. Nucl. Sci.*, 18:1101–1104, 1971.

[52] M. Sands, A Beta mismatch parameter, SLAC-AP-085.

[53] K. Schindl, Space charge, *CAS proceedings 2003*, 2003.

[54] K.-J. Kim, Rf and space-charge effects in laser-driven rf electron guns, *Nuclear Instruments and Methods in Physics Research Section A: Accelerators, Spectrometers, Detectors and Associated Equipment*, 275(2):201 – 218, 1989.

[55] B. Carlsten, New photoelectric injector design for the Los Alamos National Laboratory XUV FEL accelerator, *Nuclear Instruments and Methods in Physics Research Section A: Accelerators, Spectrometers, Detectors and Associated Equipment*, 285(1-2):313 – 319, 1989.

[56] F. Sacherer, RMS envelope equations with space charge, (CERN-SI-INT-DL-70-12):17 p, Nov 1970.

[57] S. M. Gierman, *Streak camera enhanced quadrupole scan technique for characterizing the temporal dependance of the trace space distribution of a photoinjector electron beam*, PhD thesis, University of California, San Diego, 1999.

[58] M. G. Minty and F. Zimmermann, *Measurement and control of charged particle beams*, Springer, Berlin, Germany, 2003.

[59] J. Rosenzweig and S. Anderson, The role of space-charge in emittance measurement of high-brightness photoinjector beams (talk), ICFA Sardegna, 2002.

[60] J. Radon, On the Determination of Functions from Their Integral Values along Certain Manifolds, *Medical Imaging, IEEE Transactions on*, 5(4):170–176, Dec. 1986.

[61] A. C. Kak and M. Slaney, *Principles of computerized tomographic imaging*, Society for Industrial and Applied Mathematics, Philadelphia, PA, USA, 2001.

[62] http://nobelprize.org.

[63] http://root.cern.ch.

[64] J. Scheins, Tomographic reconstruction of transverse and longitudinal phase space distributions using the Maximum entropy algorithm, Technical report, DESY, May 2004, TESLA Report 2004-08.

[65] F. Natterer, *The Mathematics of Computerized Tomography*, Society for Industrial and Applied Mathematics, Philadelphia, PA, USA, 2001.

[66] B. Gustafsson, Mathematics for computer tomography, *Physica Scripta*, T61:38–43.

[67] S. Webb, *The Physics of Medical Imaging*, Institute of Physics Publishing, 1988.

[68] P. Toft, *The Radon tranfrom - theory and implementation*, PhD thesis, Technical University of Denmark, Department of Mathematical Modeling, 1996.

[69] R. M. Rangayyan, *Biomedical Image Analysis*, CRC Press, 2005.

[70] DSP guide, http://www.dspguide.com.

[71] S. Kaczmarz, Angenäherte Auflösung von Systemen Linearer Gleichungen, *Bull. Internat. Acad. Polonaise*, Sci. Lett.(35):355–357, 1937.

[72] R. Gordon, R. Bender, and G. T. Herman, Algebraic reconstruction techniques (ART) for three-dimensional electron microscopy and X-ray photography, *J. Theor. Biol.*, 1970.

[73] R. Gordon, A Tutorial on ART (Algebraic Reconstruction Technique), *IEEE Trans. Nucl. Sci.*, NS-21(78), 1974.

[74] C. Shannon, A Mathematical Theory of Communication, *Bell System Technical Journal*, 27:379–423, 623–656, 1948.

[75] S. F. Gull and T. J. Newton, Maximum entropy tomography, *Appl. Opt.*, 25(1):156–160, 1986.

[76] G. Minerbo, MENT: a Maximum Entropy Algorithm for Reconstructing a Source from Projection Data, 10(1):48–68, May 1979.

[77] E. T. Jaynes, Information Theory and Statistical Mechanics, *Physical Review*, 106:620–630, 1957.

[78] G. Minerbo, Maximum entropy reconstruction from cone-beam projection data, *Computers in Biology and Medicine*, 9(1):29 – 37, 1979.

[79] M. A. Geitz, *Investigation on the transverse and longitudinal beam parameters at the TESLA Test Facility Linac*, PhD thesis, DESY-THESIS-1999-033, 1999.

[80] K. Flöttmann, http://www.desy.de/~mpyflo/.

[81] K. Flöttmann et al., Recent improvements to the ASTRA particle tracking code, In *proceedings PAC 2003*, Oregon, USA, 2003.

[82] G. Pöplau et al., 3D space charge calculations for bunches in the tracking code ASTRA, In *proceedings EPAC 2006*, Edinburgh, Scotland, 2006.

[83] http://mad.web.cern.ch/mad/.

[84] http://www.ghga.com/accelsoft/pbolab.html, PBO Lab 2.0, Gillespie Associates, Inc., 2001.

[85] N. Metropolis and S. Ulam, The Monte Carlo method, 44(247):335–341, Sept. 1949.

[86] P. Castro, Monte Carlo simulations of emittance measurements at TTF-2, Technical report, DESY, 2003, Technical note 2003-03.

[87] F. Löhl, Measurements of the transverse emittance at the VUV-FEL, Master's thesis, Department of Physics of the University of Hamburg, Germany, 2005, DESY-THESIS 2005-014.

[88] G. Asova et al., Design considerations for phase space tomography diagnostics at the PITZ facility., In *proceedings 8th European Workshop on Beam Diagnostics and Instrumentation for Particle Accelerators DIPAC 2007*, Venice, Mestre, Italy, 2007.

[89] D. Holder et al., A phase space tomography diagnostic for PITZ, In *proceedings EPAC 2006*, Edinburgh, Scotland, 2006.

[90] D. Holder et al., EuroFEL report 2006.

[91] C. Boulware et al., EuroFEL report 2007.

[92] G. Asova et al., Design of a Tomography Module for the PITZ Facility, In *proceedings EPAC 2008*, Genoa, Italy, 2008.

[93] http://www.danfysik.com.

[94] DANFYSIK, Quadrupole field mapper data, 2008.

[95] A. Murokh et al., Limitations on the resolution of YAG:Ce beam profile monitor for high brightness eletron beam, *World Scientific*, 2000.

[96] Particle physics booklet, July 2006.

[97] B. Gitter, Optical Transition Radiation, Technical report, CAA-Tech-Note Internal 24, UCLA Department of Physics, 1992.

[98] M. G. Minty and F. Zimmermann, Beam techniques: Beam control and manipulation, Lectures given at the U.S. Particle Accelerator School (USPAS 1999), Argonne, Illinois, 14-25 June.

[99] M. Krasilnikov, Emittance measurements and simulations at PITZ, presentation, HZB Berlin, June 2011.

[100] S. Rimjaem et al., Measurements and Simulations of Emittance for Different Bunch Charges at PITZ, In *proceedings FEL 2010*, Malmö, Sweden, 2010.

[101] J. Saisut, PITZ quadrupoles studies, presentation, PITZ seminar, October 2010.

[102] S. Rimjaem et al., Study of the transverse projected emittance for different bunch charges at the upgraded PITZ facility, In *proceedings FEL 2011*, Shanghai, China, 2011.

[103] S. Franke, V-code manual.

Curriculum vitae

Galina Asova

May 17 1978	Born in Sofia, Bulgaria
1985 - 1993	Primary education, 138 School "Prof. Vasil Zlatarski", Sofia
1993 - 1997	Secondary education, 31 High School, Sofia
1997 - 2003	Studies in the Faculty of Mathematics and Informatics, Sofia University "St. Kliment Ohridski"
January 2003	Masters Degree from the Faculty of Mathematics and Informatics
2002 - 2003	Teaching in the National School of Mathematics and Natural Sciences "Acad. L. Chakalov", Sofia
2003 - 2006	Guest scientist at DESY Zeuthen, on behalf of INRNE, Bulgarian Academy of Sciences, Sofia, development of data analysis software
since 2006	Guest scientist at DESY Zeuthen, on behalf of INRNE, Doctoral studies